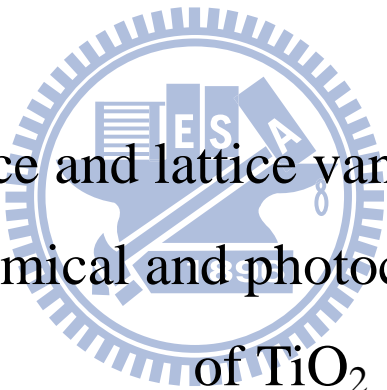


國立交通大學  
環境工程研究所  
碩士論文

晶體內部與表面摻雜釩離子對二氧化鈦光觸媒  
物化特性與光催化活性之影響



Effect of surface and lattice vanadium ions on the  
physicochemical and photocatalytic properties  
of  $\text{TiO}_2$

研究生：劉維斯  
指導教授：張淑閔 博士

中華民國九十八年八月

# 誌謝

經過三年酸甜苦辣的碩士生涯，我成長了，在這三年的歷練中，我學會了獨立思考以及對事情的處理態度，這都要感謝我的指導教授 張淑閔老師，老師除了教導我學業方面的知識外，還教會我很多做人做事的道理，這些對我的人生都有很大的助益。也謝謝陳登銘老師、董瑞安老師、徐雍瑩老師對本論文悉心指正並提供許多建議，使本論文更趨於充實完善。

此外，要感謝傑耀學長與品欣學姐對於我研究方面的引導以及精神方面的鼓勵，因為有你們的支援，我才能走完全程；還有同窗友人品涵跟精榮，因為有你們的陪伴，使我的碩士生活一點都不孤單；學妹小 G、姿吟、真端以及學弟胥哥，你們的加入讓實驗室變成一個大家庭，在這裡真的很感謝實驗室的大家，因為你們的包容以及支持，讓我能順利完成畢業論文；我要特別謝謝中興貴儀中心 EPR 操作員 吳宜瑾小姐，提供給我很多研究資料以及建議；最後，我要感謝我的家人，因為你們的經濟支援以及精神加油，讓我沒有後顧之憂，我愛你們。

僅以本文獻給所有關心我與曾經幫助過我的人。

維斯 謹誌

中華民國 98 年 8 月

# 中文摘要

本研究利用溶膠-凝膠法(sol-gel)及表面溶膠-凝膠法(surface sol-gel)製備釩離子摻雜之二氧化鈦( $\text{TiO}_2$ )，並探討晶體內部(bulk doping)或表面(surface doping)釩離子對於  $\text{TiO}_2$  材料及物化特性之影響。研究結果顯示單純  $\text{TiO}_2$  經  $300\text{ }^\circ\text{C}$  鍛燒後呈現 69.9 wt% 的銳鈦礦(anatase)與 31.1 wt% 的金紅石，同時銳鈦礦的平均晶粒為 6.1 nm，巨體摻雜後並未明顯改變  $\text{TiO}_2$  晶粒尺寸，其晶粒大小範圍為 6.0 至 6.5 nm 間，然而在 V/Ti 比例高於  $1.27 \times 10^{-3}$  時完全抑制金紅石晶相 (Rutile) 的形成，此外，由於鍛燒溫度略高於坦曼溫度，所以釩會遷移至表面形成  $\text{V}_2\text{O}_5$  晶相。由低濃度摻雜釩的 UV-Vis 圖譜中，發現巨體摻雜  $\text{TiO}_2$  於 250~320 nm 間有  $\text{V}^{5+}$  吸收波峰產生，證實摻雜釩於晶體內部會於  $\text{TiO}_2$  能帶間導入額外能階，然而當 V/Ti 莫爾比高於 1.00 %，部分  $\text{V}^{5+}$  會還原成  $\text{V}^{4+}$ ，而因為  $\text{V}^{4+}$  會同時捕捉電子電洞降低表面電荷轉移，所以降解 0.01 mM Rhodamine (RhB) 之擬一階反應速率常數隨著晶格內釩離子濃度的增加，而從  $5.20 \times 10^{-2}$  降至  $1.50 \times 10^{-2}$  1/min，利用 EPR 偵測觸媒表面 OH 自由基，其積分面積從  $5.40 \times 10^7$  降至  $5.50 \times 10^6$ ，證實電子轉移的效率會隨晶格內釩離子濃度增加而變差。相較下，表面摻雜對  $\text{TiO}_2$  的微結構及電子結構並無巨觀的影響，但表面摻雜釩的反應速率常數卻隨著表面  $\text{V}^{5+}$  濃度增加而從  $5.20 \times 10^{-2}$  提升至  $9.80 \times 10^{-2}$  1/min，當 V/Ti 約為  $1.00 \times 10^{-2}$  時，表面摻雜  $\text{TiO}_2$  的反應速率數高於內部摻雜觸媒的六倍，此原因為表面的  $\text{V}^{5+}$  易使電子累積於  $\text{TiO}_2$  表面，增進表面電荷轉移速率(觸媒表面 OH 自由基積分面積從  $2.07 \times 10^7$  提升至  $4.22 \times 10^7$ )，因此表面摻雜比巨體摻雜更可提高  $\text{TiO}_2$  光催化活性。

# Abstract

The aim of this study was to investigate the effects of bulk and surface lattice dopings on physicochemical properties and photocatalytic activities of V-doped TiO<sub>2</sub>. The sol-gel-derived TiO<sub>2</sub> exhibited 69.9 and 31.1 wt % of anatase and rutile phase, respectively. In addition, the crystallite size of the anatase TiO<sub>2</sub> was 6.1 nm. Lattice vanadium ions had no effect on crystal size of TiO<sub>2</sub>, ranging between 6.0-6.5 nm. However, lattice vanadium ions completely inhibited the formation of rutile as the V/Ti ratio is as high as 1.27× 10<sup>-3</sup>. V<sub>2</sub>O<sub>5</sub> crystals were observed on the surface of TiO<sub>2</sub> since vanadium ion diffused to surface when the calcination temperature was higher than its Tammann temperature. The UV-vis spectra show that bulk doping resulted in an additional absorption band centered at 289 nm. This phenomenon indicated that incorporation of V<sup>5+</sup> ions into the bulk lattice of TiO<sub>2</sub> at low vanadium concentrations (V/Ti ratio < 1.00× 10<sup>-2</sup>) introduced extra energy levels in the conduction band. When V/Ti atomic ratio was higher than 1.00 %, some V<sup>5+</sup> were partially reduced to V<sup>4+</sup> which acted as charge recombination centers. Pure TiO<sub>2</sub> exhibited a rate constant of 5.20×10<sup>-2</sup> min<sup>-1</sup> for the photocatalytic degradation of Rhodamine B (RhB). Bulk doping decreased the photocatalytic activity to from 5.20×10<sup>-2</sup> to 1.50×10<sup>-2</sup> min<sup>-1</sup> when the V/Ti ratio increased from 4.41×10<sup>-5</sup> to 1.22×10<sup>-2</sup>. In addition, the integrated area of generated •OH on the surface of photocatalysts, which were calculated by EPR, decreased from 5.40×10<sup>7</sup> to 5.50×10<sup>6</sup>. The results indicated electrons diffuse to surface hardly. In contrast, surface doping had little effects on the micro- and electronic structures of TiO<sub>2</sub>. Nevertheless, the photoactivity was enhanced from 5.20×10<sup>-2</sup> to 9.80×10<sup>-2</sup> min<sup>-1</sup> upon increasing vanadium concentration. The photoactivity of the surface doped TiO<sub>2</sub> was six times higher than that of bulk doped ones at the V/Ti ratio of 1.00×10<sup>-2</sup>. Such enhancement is due to that surface-V<sup>5+</sup> promotes diffusion of electrons to surface that further facility charges transfer to reactants. According to integrated area of surface doped materials, which increased from 2.07×10<sup>7</sup> to 4.22×10<sup>7</sup>, it indicate the electrons diffuse to surface efficaciously. Therefore, surface doping greatly improve the degradation efficiency, while bulk ones lad to detrimental effects on the photocatalytic activity.

# Content Index

誌謝 .....	I
中文摘要 .....	II
ABSTRACT.....	III
CONTENT INDEX.....	IV
FIGURE CAPTIONS .....	VII
TABLE CAPTIONS .....	XI
<b>CHAPTER 1 INTRODUCTION .....</b>	<b>1</b>
1-1 MOTIVATION .....	1
1-2 OBJECTIVES.....	2
<b>CHAPTER 2 BACKGROUND AND THEORY .....</b>	<b>3</b>
<b>2-1 TiO<sub>2</sub> SEMICONDUCTOR PHOTOCATALYSTS .....</b>	<b>3</b>
2-1-1 <i>Background and material properties</i> .....	3
2-1-2 <i>Principle of photocatalysis</i> .....	9
2-1-3 <i>Photoassisted degradation of Rhodamine B</i> .....	13
<b>2-2 SYNTHESIS TOWARD METAL OXIDE .....</b>	<b>14</b>
2-2-1 <i>Sol-gel method</i> .....	14
2-2-2 <i>Surface sol-gel method</i> .....	18
<b>2-3 DOPING TiO<sub>2</sub> WITH IMPURITIES.....</b>	<b>20</b>
<b>2-4 BULK AND SURFACE DOPING SITES .....</b>	<b>26</b>
<b>CHAPTER 3 MATERIALS AND METHODS .....</b>	<b>29</b>
<b>3-1 MATERIALS .....</b>	<b>29</b>
<b>3-2 PREPARATION OF BULK DOPED TiO<sub>2</sub> VIA SOL-GEL PROCESS.....</b>	<b>31</b>
<b>3-3 PREPARATION OF SURFACE DOPED TiO<sub>2</sub> VIA SURFACE SOL-GEL PROCESS</b>	

.....	33
<b>3-4 CHARACTERIZATION .....</b>	<b>36</b>
3-4-1 <i>X-ray photoelectron spectroscopy (XPS)</i> .....	36
3-4-2 <i>Time-of-Flight Secondary Ion Mass Spectrometer (TOF-SIMS)</i> .....	37
3-4-3 <i>Scanning electronic microscopy (SEM)</i> .....	37
3-4-4 <i>X-ray diffractometry</i> .....	38
3-4-5 <i>UV/Vis diffuse reflectance spectroscopy (UV-Vis DRS)</i> .....	39
3-4-6 <i>Inductively Coupled Plasma Mass Spectrometry (ICP-MS)</i> .....	39
3-4-7 <i>Specific surface area</i> .....	39
3-4-8 <i>Electron paramagnetic resonance (EPR)</i> .....	39
3-4-9 <i>Transmission Electron Microscope (TEM)</i> .....	41
<b>3-5 PHOTOCATALYTIC OF RHB DECOMPOSITION .....</b>	<b>41</b>
 <b>CHAPTER 4 RESULTS AND DISCUSSION .....</b>	 <b>43</b>
4-1 CHEMICAL COMPOSITIONS.....	43
4-2 MORPHOLOGY .....	45
4-3 MICROSTRUCTURES .....	47
4-4 UV-VISIBLE ABSORPTION.....	53
4-5 PHOTOCATALYTIC ACTIVITY .....	60
4-6 EPR STUDIES OF BULK AND SURFACE DOPING MATERIALS.....	67
 <b>CHAPTER 5 CONCLUSIONS .....</b>	 <b>82</b>
 <b>REFERENCES .....</b>	 <b>83</b>
 <b>APPENDIX A EXPERIMENTAL PARAMETERS.....</b>	 <b>91</b>
 <b>APPENDIX B INSTRUMENT PRINCIPLE .....</b>	 <b>93</b>
Appendix B-1 <i>Time-of-Flight Secondary Ion Mass Spectrometer</i> .....	93
Appendix B-2 <i>X-ray powder diffractometry (XRPD)</i> .....	94
Appendix B-3 <i>UV-vis diffuse reflectance spectroscopy (DRS)</i> .....	96
Appendix B-4 <i>Electron paramagnetic resonance (EPR)</i> .....	97
 <b>APPENDIX C BET DATA .....</b>	 <b>102</b>

<b>APPENDIX D. ESCA ANALYSIS .....</b>	<b>103</b>
<b>APPENDIX E BULK DOPED MATERIALS WITH HIGH VANADIUM IONS .....</b>	<b>106</b>
<b>APPENDIX F VANADIUM-DOPED ON THE SURFACE OF TIO<sub>2</sub>.....</b>	<b>108</b>
<b>APPENDIX G REDOX POTENTIAL .....</b>	<b>111</b>
<b>APPENDIX H LANGMUIR-HINSELWOOD KINETICS .</b>	<b>112</b>
<b>APPENDIX I TEM OF SURFACE DOPED MATERIALS ...</b>	<b>114</b>



# Figure Captions

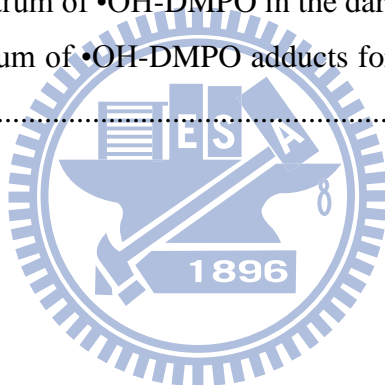
Figure 2-1	The density of electronic states of TiO <sub>2</sub> .....	4
Figure 2-2	Variation of enthalpies of anatase, brookite, and rutile as a function of particle size.....	6
Figure 2-3	The crystal phases of TiO <sub>2</sub> .....	7
Figure 2-4	UV-Vis reflectance spectra of size-quantized TiO <sub>2</sub> .....	8
Figure 2-5	The formation of a space charge layer in a large and small semiconductor particle in equilibrium with a solution redox system. ....	8
Figure 2-6	Schematic photoexcitation in a solid followed by deexcitation events.....	9
Figure 2-7	Optical absorption for (a) $h\nu = E_g$ , (b) $h\nu > E_g$ , and (c) $h\nu < E_g$ .....	10
Figure 2-8	The energies for various semiconductors in aqueous electrolytes at pH = 1.....	11
Figure 2-9	Kinetics of the primary steps in photoelectrochemical mechanism. Where TiOH represents the primary hydrated surface functionality of TiO <sub>2</sub> , $e_{cb}^-$ is a conduction-band, $e_{tr}^-$ is a trapped conduction band electron, $h_{vb}^+$ is a valence band hole, Red is an electron donor (i.e., reductant), Ox is an electron acceptor (i.e., oxidant), $[Ti^{4+}OH \cdot]^+$ is the surface-trapped valence band (VB) hole (i.e., surface-bound hydroxyl radical), and $[Ti^{3+}OH]$ is the surface-trapped conduction band (CB) electron. And the arrow lengths are representative of the respective time scales.....	11
Figure 2-10	Secondary reactions with activated oxygen species in the photoelectrochemical mechanism.....	12
Figure 2-11	Electron-transfer processes (a) for UV irradiation of TiO <sub>2</sub> with the self-photosensitized pathway (b) under visible light irradiation which subsequent to excitation of RhB dye.....	13
Figure 2-12	Formation and competitive reactions of $\bullet OH$ radicals during visible light irradiation of Rhodamine B.....	14
Figure 2-13	The process of sol-gel under acid condition. (a)Hydrolysis, (b)Condensation, and (c)Gelation.....	16
Figure 2-14	Gel process sequence.....	16
Figure 2-15	The relationship between gelation times and H <sub>2</sub> O:alkoxide ratio.....	17
Figure 2-16	The different structure of particles depend on pH.....	18
Figure 2-17	Schematic representation of the surface sol-gel process.....	19
Figure 2-18	Detail of liquid flow patterns of the containous process. $U$ is the withdrawal speed, $S$ is the station point, $\delta$ is the boundary layer, and $h$ is the thickness of the fluid film..	20



Figure 2-19	The production prepared by sol-gel-derived with different processes. ....	20
Figure 2-20	The structure of surface doped materials.....	21
Figure 2-21	Proposed V site transformations for V/TiO <sub>2</sub> in surface doped materials (A) and for bulk doped materials (B). [H] for models a and c indicates the presence/absence of hydrogen cannot be determined.....	22
Figure 2-22	The bonding diagram of the TiO <sub>2</sub> perfect crystal (rutile) proposed by Soratin and Schwarz.....	23
Figure 2-23	The DOS of metal-doped TiO <sub>2</sub> (Ti <sub>1-x</sub> A <sub>x</sub> O <sub>2</sub> : A=V or Ti). Gray lines means total DOS and black lines shows dopant's DOS. <sup>5</sup> .....	24
Figure 2-24	Band model of Ti <sub>1-x</sub> V <sub>x</sub> O <sub>2</sub> film electrodes at bias potential of 1 V vs. SCE in an electrolyte solution. ....	24
Figure 2-25	The photochemical mechanism in the present of transition metal ions.....	25
Figure 2-26	The energy level diagram calculated using large cluster models of (Ti <sub>15</sub> O <sub>56</sub> ) <sup>52-</sup> and (Ti <sub>11</sub> O <sub>34</sub> ) <sup>24-</sup> O* corresponding to the bulk and surface of rutile TiO <sub>2</sub> . ....	27
Figure 2-27	Surface and bulk electron carrier trapping.....	28
Figure 3-1	Flow chart of experimental design in this study. ....	30
Figure 3-2	The chemical structure of RhB. ....	30
Figure 3-3	The synthetic process of bulk doped materials. (a) the flow charts of the synthesis and (b) the recipes of precursor solutions. ....	32
Figure 3-4	The synthetic process of surface doped materials. (a) the flow charts of the synthesis of surface doped materials, (b) the recipes of precursor solutions, and (c) the surface sol-gel processes for coating. ....	34
Figure 3-5	A design chart and a photograph of surface sol-gel system.....	35
Figure 3-6	The geometric structure of pure, bulk and surface doped TiO <sub>2</sub> . ....	36
Figure 3-7	The UV lamp spectral distribution.....	40
Figure 3-8	The UV-Vis spectrum of 0.01 mM RhB. ....	41
Figure 3-9	A design chart for photocatalysis reactor and A photograph of photocatalytic reactor. ....	42
Figure 4-1	The morphology of pure TiO <sub>2</sub> calcined at (a) 150 °C for 3 h and (b) 150 and 300 °C for 3 h. ....	45
Figure 4-2	The SEM images of bulk doped materials.....	46
Figure 4-3	The SEM images of (a) surface doped materials and (b) cross sectional view of a V-doped TiO <sub>2</sub> film prepared by the surface sol-gel method. ....	46
Figure 4-4	The XRD patterns of bulk doped TiO <sub>2</sub> at different vanadium ion concentrations.	

.....	48
Figure 4-5 The effect of bulk defect on growth of crystal.....	49
Figure 4-6 The GI-XRD patterns of bulk doping materials. ....	50
Figure 4-7 The XRD patterns of surface doped materials at different vanadium ions concentration. ....	51
Figure 4-8 The GI-XRD patterns of surface doped materials. ....	52
Figure 4-9 The microstructures of bulk and surface doped TiO <sub>2</sub> . ....	53
Figure 4-10 UV-Vis DRS spectra of TiO <sub>2</sub> . The red solid line: Upper conduction band. The blue dash line: Lower conduction band.....	54
Figure 4-11 The UV-visible absorption spectra of all bulk doped materials at different vanadium ions concentration, except VT $1.22 \times 10^{-2}$ which is shown in inside graph. ....	55
Figure 4-12 Energy levels of impurity ions in rutile. ....	56
Figure 4-13 The concept of electronic structure for bulk doping materials. (a) low vanadium ions (< 1 mole%); (b) high vanadium ions (i.e. VT $1.22 \times 10^{-2}$ ).....	57
Figure 4-14 The UV-visible absorption spectra of the surface doped materials at different vanadium ions concentrations. ....	58
Figure 4-15 Schematic band energy diagram for the TiO <sub>2</sub> /V <sub>2</sub> O <sub>5</sub> composite semiconductor. ....	59
Figure 4-16 The electronic structure of surface doping materials.....	59
Figure 4-17 The decoloration of 0.01 mM RhB by pure and bulk doped TiO <sub>2</sub> under (a) 305 nm and (b) 365 nm UV irradiation.....	61
Figure 4-18 The rate constants of bulk doped materials at various vanadium ions concentration compared with pure TiO <sub>2</sub> under (a) 305 nm UV and (b) 365 nm UV irradiation. ....	62
Figure 4-19 The concept of higher content V <sup>4+</sup> at substitutional site in Q-size TiO <sub>2</sub> lattice. ....	64
Figure 4-20 The decoloration of 0.01 mM RhB by surface doping materials at various vanadium ions concentration compared with pure TiO <sub>2</sub> under (a) 305 nm UV and (b) 365 nm UV irradiation.....	65
Figure 4-21 The rate constants of surface doped materials at various vanadium ions concentration compared with pure TiO <sub>2</sub> under (a) 305 nm UV and (b) 365 nm UV irradiation. ....	66
Figure 4-22 The difference in EPR spectra of pure TiO <sub>2</sub> before and after irradiation of UV at 77K. ....	68
Figure 4-23 EPR spectra of pure and bulk doped TiO <sub>2</sub> at different vanadium contents at 77K in the dark. (a) The bulk V/Ti ratios ranged $0-5.09 \times 10^{-4}$ and (b) The bulk V/Ti ratios in the	

range $1.27 \times 10^{-3}$ - $1.22 \times 10^{-2}$ .....	70
Figure 4-24 The EPR spectra of vanadium ions doped in $\text{TiO}_2$ .....	71
Figure 4-25 EPR spectra of bulk doped materials at various vanadium concentrations under UV irradiation at 77K.....	71
Figure 4-26 The concept of bulk doping materials at low vanadium concentration.....	72
Figure 4-27 The concept of bulk doping materials at intermediate vanadium concentration.....	73
Figure 4-28 The concept of bulk doping materials at high vanadium concentration.....	74
Figure 4-29 EPR spectra of surface doping materials at various vanadium concentration in the dark at 77K.....	74
Figure 4-30 EPR spectra of surface doped materials at various vanadium concentrations under UV light at 77K.....	76
Figure 4-31 The concept of surface doped materials.....	77
Figure 4-32 The ERP spectrum of $\bullet\text{OH}$ -DMPO in the dark and UV irradiation.....	80
Figure 4-33 The mechanism of $\bullet\text{OH}$ -DMPO adducts formed upon trapping of OH radicals by the DMPO molecules.....	81



# Table Captions

Table 2-1	Milestone of TiO <sub>2</sub> -related reference .....	5
Table 2-2	The relationship between crystal size and stable phase . .....	6
Table 4-1	The bulk and surface V-to-Ti atomic ratios of bulk doped TiO <sub>2</sub> . .....	43
Table 4-2	The bulk and surface V-to-Ti atomic ratios of surface doped TiO <sub>2</sub> . .....	44
Table 4-3	The crystallite sizes, d-spacing of materials and weight ratio of rutile phase of bulk doped TiO <sub>2</sub> . .....	48
Table 4-4	The crystallite sizes of materials and weight ratio of rutile phase of surface doped TiO <sub>2</sub> . .....	51
Table 4-5	The band gap energy of bulk doped TiO <sub>2</sub> . .....	56
Table 4-6	The band gap energy of surface doped TiO <sub>2</sub> .....	58
Table 4-7	The rate constants of bulk doped TiO <sub>2</sub> at various vanadium concentration compared with pure TiO <sub>2</sub> under 365 and 305 nm UV irradiation. ....	63
Table 4-8	The rate constants of the surface doped TiO <sub>2</sub> at various V/Ti ratios. ....	67
Table 4-9	g value for various paramagnetic species. ....	78
Table 4-10	The integrated areas of •OH-DMPO signals obtained from the bulk doped TiO <sub>2</sub> suspension under UV irradiation. The suspensions were aerated with O <sub>2</sub> for 30 min in the dark before irradiation. ....	80
Table 4-11	The integrated areas of •OH-DMPO signals obtained from the surface doped TiO <sub>2</sub> suspension under UV irradiation. The suspensions were aerated with O <sub>2</sub> for 30 min in the dark before irradiation. ....	81

# Chapter 1 Introduction

## 1-1 Motivation

Titanium dioxide ( $\text{TiO}_2$ ) is the mostly used photocatalysts for decomposition of environmental pollutants because of cheap, nontoxic, and highly chemical stable characteristics<sup>1</sup>. To improve its photocatalytic activity, impurities including transition metal ions ( $\text{Fe}$ ,  $\text{V}$ )<sup>2-6</sup> and non-metal ions ( $\text{N}$ ,  $\text{C}$ )<sup>7-9</sup> were doped into the  $\text{TiO}_2$  lattice to modify its microstructures and electronic structures. The kinds of contributions of the modification to the photocatalytic activity include (1) inhibition of recombination by increasing the charge separation; (2) increase in the wavelength response range (i.e. excitation of wide band gap semiconductors by visible light); and (3) change in the selectivity or yield of a particular product.<sup>10-12</sup>

The types and chemical states of dopants determine the microstructure, band gaps and photoactivity of metal-doped  $\text{TiO}_2$  because of different electronic configurations and sizes of the ions. Panagiotis Bouras et al.<sup>4</sup> reported  $\text{Fe}^{3+}$ ,  $\text{Cr}^{3+}$  and  $\text{Co}^{2+}$  denoting visible-light photocatalyst were used to decompose Basic Blue 41, while photodegradation efficiency of the doped material was achieved only at very high doping levels. Kemp et al.<sup>13</sup> reported that doping of rutile with  $\text{Cr}^{3+}$ ,  $\text{V}^{5+}$  or  $\text{Mn}^{2+}$  reduces its photoactivity, while doping with  $\text{Mo}^{5+}$  or  $\text{W}^{5+}$  enhances its photocatalytic performance. Martin et al.<sup>14</sup> doped  $\text{TiO}_2$  with  $\text{V}^{5+}$  via coprecipitation method which also resulted in reduced photoreactivity. However, Klosek and Raftrey<sup>15</sup> reported V-doped  $\text{TiO}_2$  extended the wavelength range of the catalyst into the visible region (396-450 nm) and greatly improved the photocatalytic activity of titania under solar light irradiation. However, the effects of vanadium ions on the photocatalytic activity of  $\text{TiO}_2$  are still controversial.

Such uncertainties are attributed to the multiple oxidation states of vanadium ions ( $\text{V}^{3+}$ ,  $\text{V}^{4+}$  and  $\text{V}^{5+}$ ) which result in different nonstoichiometry and bandgaps of  $\text{TiO}_2$ . In addition, the doping sites affect the bulk and surface crystalline structure, thereby controlling the utility of photo-generated charge carriers. Balikdjian et al.<sup>16</sup> reported that the presence of V species in the bulk lattice of anatase inhibited the transformation of anatase into rutile. Generally, anatase  $\text{TiO}_2$  exhibits higher photocatalytic activity than rutile. In addition, the particle sizes of  $\text{TiO}_2$  become small after doping with  $\text{V}^{5+}$  ions.<sup>10</sup> Large amounts of surface defects of the small sized photocatalyst promote the diffusion of charge carrier toward the surface and enhance photocatalytic activity.<sup>17 18</sup> However, the defects in the bulk lattice also could deeply trap charge carriers and inhibit charge diffusion as well as reduce photocatalytic

activity.

In contrast to deep trapping in the bulk, defects on the surface sites not only trap charge carriers but also deliver the trapped charges to adsorbed reactants. The trapping time of carrier electrons at the surface level become longer with an increase in  $\Delta E_{\text{surface}}$  ( $\Delta E_{\text{surface}}$  means the energy different LUMO of bulk  $\text{TiO}_2$  and the lowest level of transition metal).<sup>19</sup> Moreover, surface defects can cause unsaturated coordination of  $\text{Ti}^{4+}$  and oxygen vacancies which serve as active sites for photocatalysis.<sup>20</sup> Chang et al.<sup>21</sup> reported Lewis acid sites of surface modified  $\text{TiO}_2$  readily chemisorbed water to generate reactive hydroxyl radicals. In addition, electron transfer from conduction band to adsorbed  $\text{O}_2$  was improved for efficient mediated photocatalysis. However, the effects of doping sites of vanadium ions on the physicochemical and photocatalytic properties have not been documented yet.

## 1-2 Objectives

This study aims to investigate the influence of bulk and surface doping sites on the micro-, electronic- structures and chemical states of V-doped  $\text{TiO}_2$ . The bulk and surface doped materials were prepared by sol-gel and surface sol-gel, respectively. In addition, the charge trapping and interfacial charge transfer properties were analyzed using EPR. The photocatalytic activities of the doped  $\text{TiO}_2$  were determined in terms of decoloration of rhodamine B. The photocatalytic behavior of the doped  $\text{TiO}_2$  with respect to its bulk and surface defects were discussed based on the physicochemical properties.

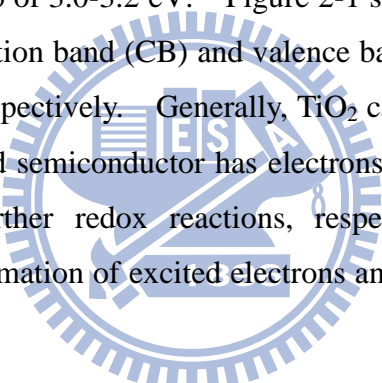
## Chapter 2 Background and theory

### 2-1 TiO<sub>2</sub> semiconductor photocatalysts

#### 2-1-1 Background and material properties

In 1972, Fujishima and Honda successfully found TiO<sub>2</sub> nanoparticles that can be used in photocatalytic reactors for degrading pollutions in water or air.<sup>22</sup> Afterward, scientific studies on development and fabricate of photocatalysis by semiconductor was blossomed, which are listed in Table 2-1. In order to improve the efficiency of photoactivity, some surface modification methods have been proposed for the development of advanced photocatalysts, including composite semiconductors, surface sensitization, and transition metal doping.<sup>5, 9, 17</sup> Nowadays, TiO<sub>2</sub> has been widely used in industrial application such as photocatalysis<sup>23</sup>, solar energy cell<sup>24</sup>, and gas sensors.<sup>25</sup>

TiO<sub>2</sub> possesses a bandgap of 3.0-3.2 eV. Figure 2-1 shows the total density of electronic states of TiO<sub>2</sub>. The conduction band (CB) and valence band (VB) of TiO<sub>2</sub> mainly consist of the Ti 3d and O 2p states, respectively. Generally, TiO<sub>2</sub> can be excited by energy in terms of heat or photon. The excited semiconductor has electrons and holes pairs within conduction and valence bands for further redox reactions, respectively. Thus, the principle of photocatalysis is the transformation of excited electrons and holes which play important roles in this system.<sup>17, 26</sup>



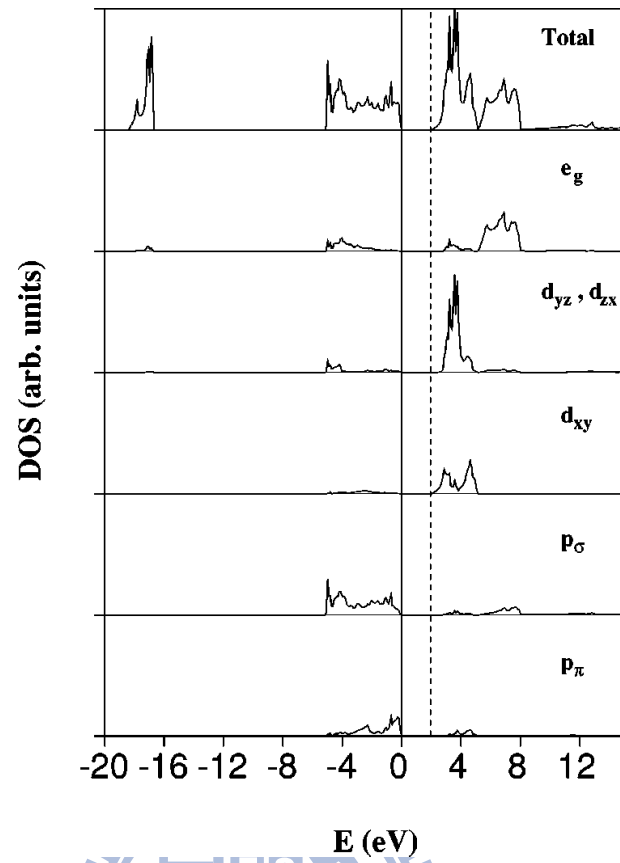


Figure 2-1 The density of electronic states of TiO<sub>2</sub>.<sup>27</sup>

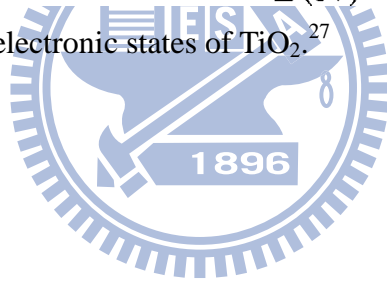




Table 2-1 Milestone of TiO<sub>2</sub>-related studies.

Year	Authors	The results and findings	Ref.
1972	Fujishima et al.	First finding about electrochemical photolysis of water at a semiconductor electrode.	22
1987	Matthews et al.	Photooxidation of organic impurities in water using thin films of titanium dioxide.	28
1994	Choi et al.	The summarization of metal-ion dopants in quantum-sized TiO <sub>2</sub> .	29
1994	Martin et al.	Photochemical mechanism of quantum-sized vanadium-doped TiO <sub>2</sub> particles	14
1995	Linsebigler et al.	Mechanisms of photocatalysis of TiO <sub>2</sub> , including surface modification method.	17
1999	Litter et al.	The mechanism of photocatalytic systems on transition metal ions doped in TiO <sub>2</sub> .	30
2002	Haber et al.	Surface doping of rutile by vanadium.	18
2003	Diebold et al.	The surface science of titanium dioxide.	31
2003	Weckhuysen et al.	Chemistry, spectroscopy and the role of supported vanadium oxides in heterogeneous catalysis	32
2004	Lee et al.	Electronic surface state of TiO <sub>2</sub> electrode doped with transition metals, studied with cluster model and DV-X alpha method	19
2007	Xin et al.	The mechanisms of photoinduced carriers separation and recombination for Fe <sup>3+</sup> -TiO <sub>2</sub> photocatalysts	3

TiO<sub>2</sub> has three types of crystalline structures: anatase, rutile, and brookite. At higher temperature above 623 K, anatase starts to transform to brookite and /or rutile, and then brookite transforms to rutile. At lower temperature below 623 K, the transformation between anatase and brookite may be reversible. The activation energy of transformation from anatase to brookite (11.9 KJ mol<sup>-1</sup>) is much lower than that from brookite to rutile (163 KJ mol<sup>-1</sup>). This means the brookite → rutile transformation occurs under higher temperature, and proceeds rapidly (frequency factor is large).<sup>33</sup> Figure 2-2 illustrates the variation of enthalpies of the three phases as a function of the particle size and Table 2-2 lists the range of crystal size on stable phase. If the crystal size of the three phases is equal, anatase can

transforms to brookite and then transforms to rutile.

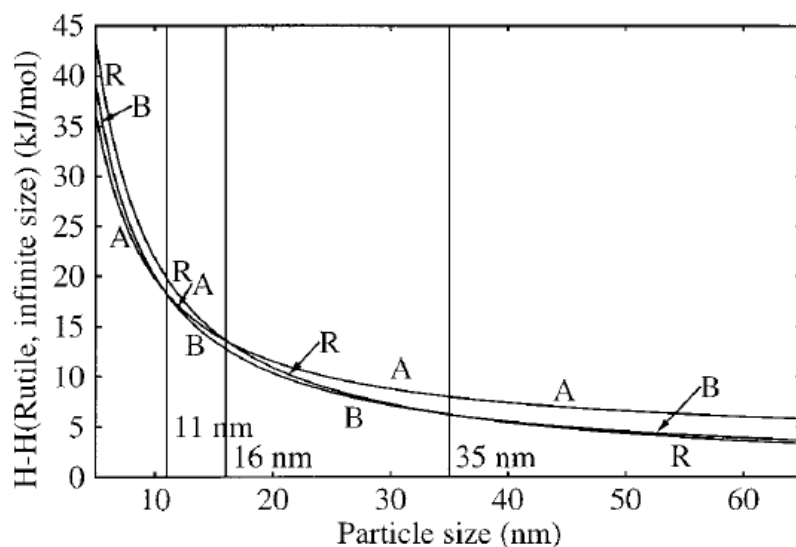


Figure 2-2 Variation of enthalpies of anatase, brookite, and rutile as a function of particle size.<sup>33</sup>

Table 2-2 The relationship between crystal size and stable phase<sup>33</sup>.

Crystal size	Most stability phase
< 11 nm	Anatase
11 ~ 35 nm	Brookite
> 35 nm	Rutile

Figure 2-3 shows the crystalline structures of anatase and rutile  $\text{TiO}_2$ . Each  $\text{Ti}^{4+}$  ion is surrounded by an octahedron of six  $\text{O}^{2-}$  ions. In the rutile structure, each octahedron is in contact with 10 neighboring octahedrons (two sharing edge oxygen pairs and eight sharing corner oxygen atoms), while in the anatase structure each octahedron is in contact with eight neighbors (four sharing an edge and four sharing a corner). These differences in lattice structures cause different mass densities and electronic band structures between anatase and rutile.<sup>17</sup> The octahedron in anatase is significantly distorted so that its symmetry is lower than orthorhombic. Therefore, anatase shows a higher adsorptive ability toward organic compounds<sup>23</sup> and lower rate of charge recombination<sup>34</sup>, while rutile shows a lower bandgap energy and higher thermal stability.<sup>17</sup>

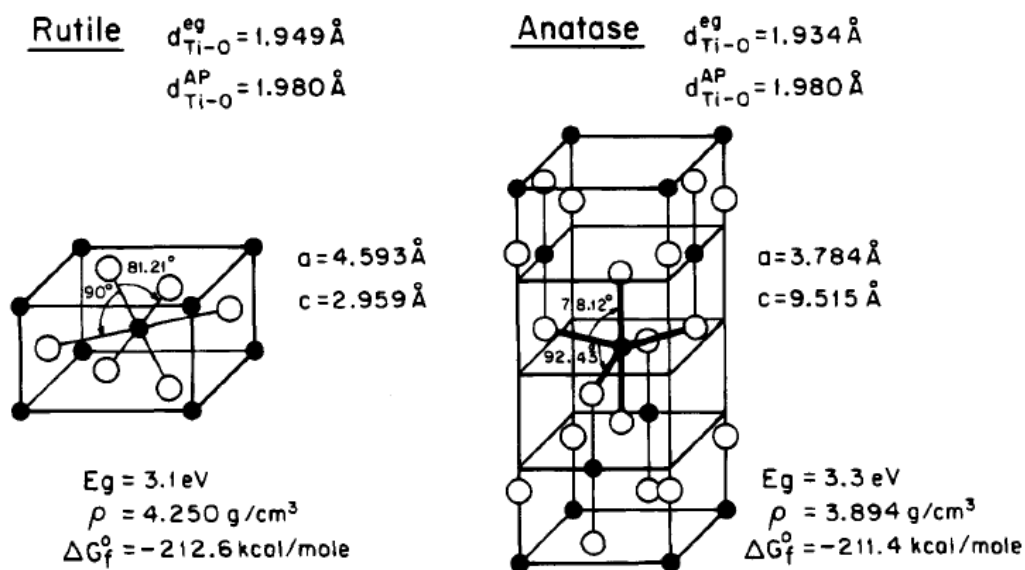


Figure 2-3 The crystal phases of  $\text{TiO}_2$ .<sup>17</sup>

When the crystallite dimension of a semiconductor particle falls below a critical radius of approximately 10 nm, the band gap increases and the band edges shift to yield larger redox potentials, as shown in Figure 2-4. Thus, the size-quantized semiconductor  $\text{TiO}_2$  particles may result in increased photo-efficiencies for systems in which the rate-limiting step is charge transfer. Figure 2-5 shows a high photo-reactivity of quantum-size  $\text{TiO}_2$  due to the lack of band bending, while both electrons and holes are readily available at the interface (or vary close). However, size-quantized  $\text{TiO}_2$  have been found to be less photoactive than their bulk-phase cases because surface speciation and surface defect density reduce photoactivity. Thus, the positive effects of increased over potentials (i.e., difference between  $E_{\text{vb}}$  and  $E_{\text{redox}}$ ) on quantum yields could be offset by unfavorable surface speciation and surface defects due to the preparation method of size-quantized semiconductor particles.<sup>26</sup>

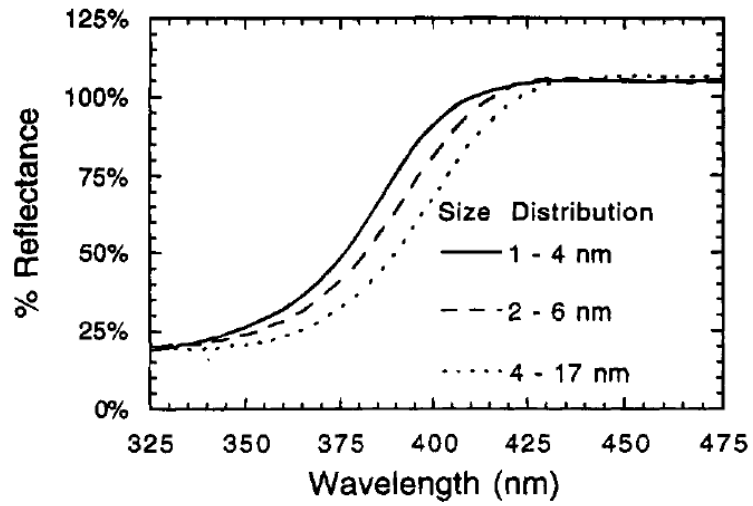


Figure 2-4 UV-Vis reflectance spectra of size-quantized  $\text{TiO}_2$ .<sup>26</sup>

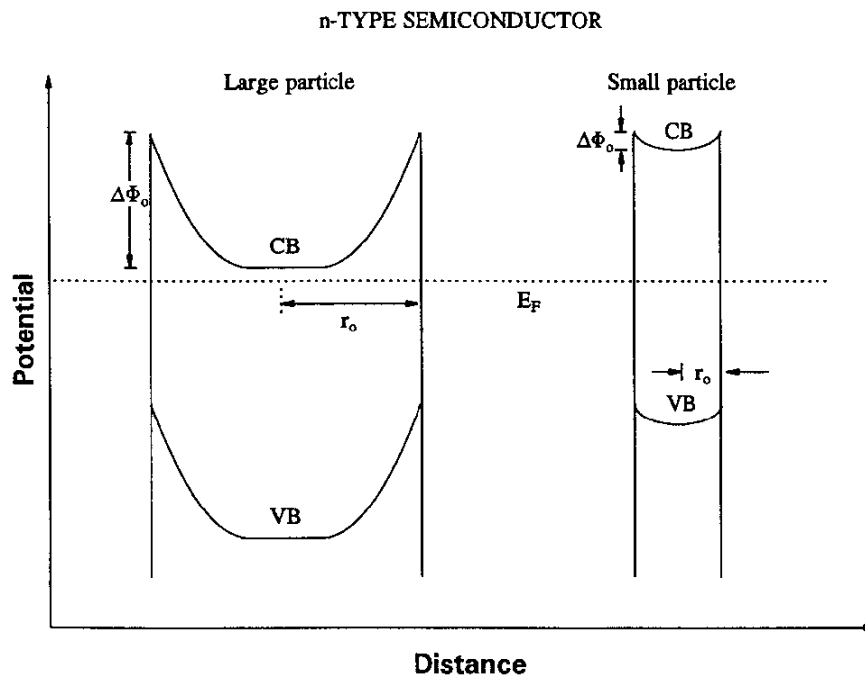


Figure 2-5 The formation of a space charge layer in a large and small semiconductor particle in equilibrium with a solution redox system.<sup>10</sup>

## 2-1-2 Principle of photocatalysis

Heterogeneous photocatalysis is one of the popular techniques for decontamination of air and wastewater, because photocatalyst can transform solar energy into chemical energy to degrade pollutants. The basic principles of heterogeneous photocatalysis can be simply summarized as follows. After the generation of charge carriers by absorbing UV-light with the energy over the band gap, the charge carriers undergo trapping, recombination, detrapping, and migration to the surface, as seen in Figure 2-6.<sup>14, 26, 29</sup>

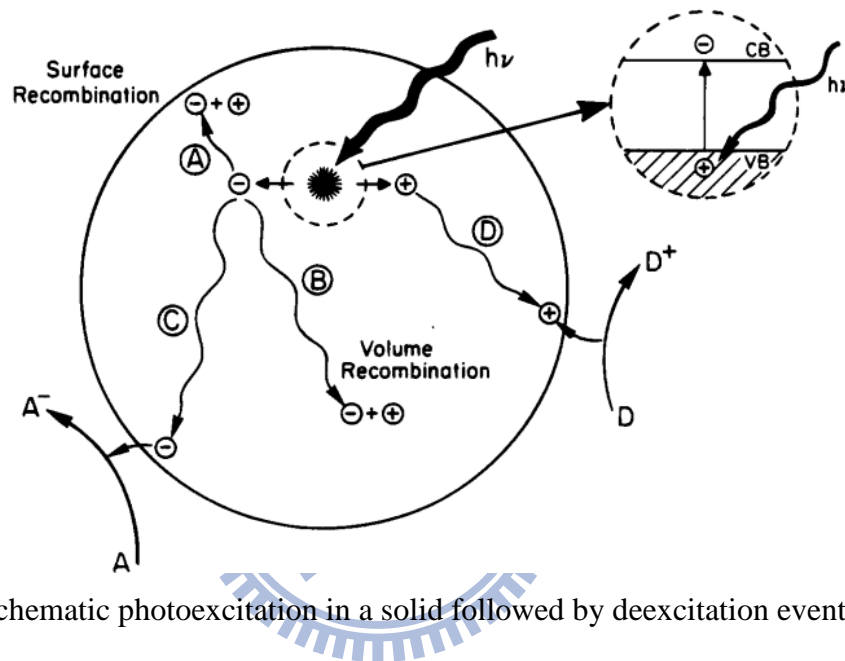


Figure 2-6 Schematic photoexcitation in a solid followed by deexcitation events.<sup>17</sup>

Figure 2-7 shows the basic transitions in a semiconductor, including intrinsic and extrinsic transitions. When the semiconductor is irradiated with UV light, photons are absorbed to create electron-hole pairs while the photon energy ( $h\nu$ ) is equal to or larger than the bandgap energy ( $E_g$ ). If  $h\nu$  is greater than  $E_g$ , excess energy is dissipated as heat, as shown in Figure 2-7 (b). These processes are called intrinsic transitions or band-to-band transitions. In addition, for  $h\nu$  is less than  $E_g$ , a photon will be absorbed by energy states which are created by chemical impurities or physical defects. Above performance is defined extrinsic transition, as shown in Figure 2-7 (c).<sup>35</sup>

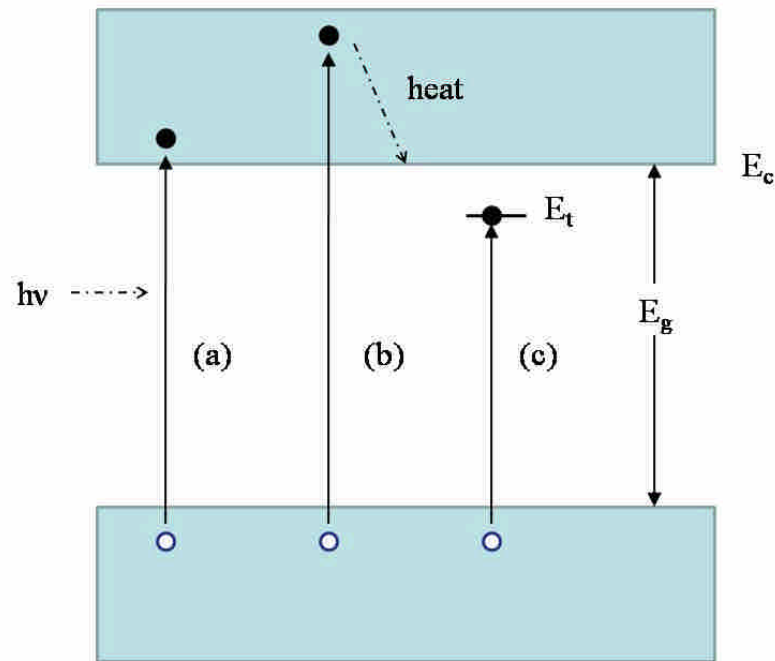


Figure 2-7 Optical absorption for (a)  $h\nu = E_g$ , (b)  $h\nu > E_g$ , and (c)  $h\nu < E_g$ .<sup>35</sup>

For thermodynamic view point, the band energy positions and the redox potential of semiconductors determine the ability of charge transfer to acceptors. Adsorbed pollutants can be reduced by conduction band (CB) electrons if they have redox potential more positive than the  $V_{fb}$  of the CB. Besides, the pollutants can also be oxidized by valence band (VB) holes if they have reduction potential more negative than the  $V_{fb}$  of the VB.<sup>30, 36</sup> Figure 2-8 shows the band edge positions for various semiconductors. Left axis presents the internal energy scale relative to the vacuum level and right one shows the comparison with normal hydrogen electrode (NHE). The positions are originated from the flat band potentials in a contact solution of aqueous electrolyte at  $\text{pH} = 1$ . Therefore, more pollutants can be decomposed in case the band gap is larger.

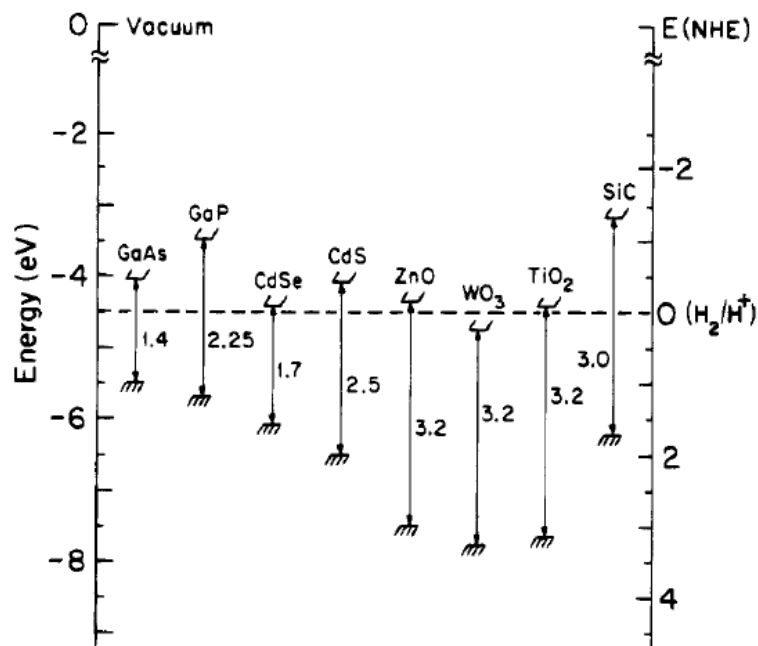


Figure 2-8 The energies for various semiconductors in aqueous electrolytes at pH = 1.<sup>17</sup>

Figure 2-9 shows the time scale of charge carrier generation, trapping, recombination, and interfacial transfer. After charge-carrier generation ( $\sim$ fs), recombination is mediated primarily by  $\text{Ti}^{3+}$  in the first 10 ns. Valence-band holes are sequestered as long-lived  $\text{TiOH}^+$  after 10 ns.  $\text{TiOH}$  is reformed by recombination with conduction band electrons or oxidation of the substrate on the time scale of 100 ns. However, the electrons transfer from CB to surface is micro-seconds, so the phenomena is determine step in photocatalysis.<sup>26</sup>

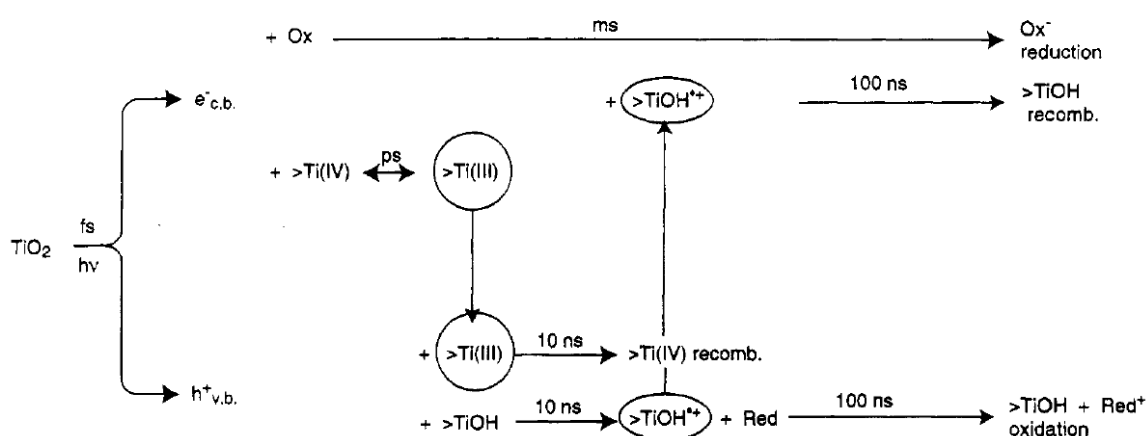


Figure 2-9 Kinetics of the primary steps in photoelectrochemical mechanism. Where  $\text{TiOH}$  represents the primary hydrated surface functionality of  $\text{TiO}_2$ ,  $e_{cb}^-$  is a conduction-band,  $e_{tr}^-$  is a trapped conduction band electron,  $h_{vb}^+$  is a valence band hole, Red is an electron donor (i.e., reductant), Ox is an electron acceptor (i.e., oxidant),

$[\text{Ti}^{4+}\text{OH}^{\bullet}]^+$  is the surface-trapped valence band (VB) hole (i.e., surface-bound hydroxyl radical), and  $[\text{Ti}^{3+}\text{OH}]$  is the surface-trapped conduction band (CB) electron. And the arrow lengths are representative of the respective time scales.<sup>26</sup>

Hoffmann et al.<sup>26</sup> and Hurum et al.<sup>37</sup> reported that the photogenerated holes recombine with surface electrons easily. So, the present of oxygen not only act as an electron acceptor, but also perform  $\text{H}_2\text{O}_2$  which is a direct source of hydroxyl radicals.<sup>26</sup> Besides, the hydroxyl radical ( $\bullet\text{OH}$ ) was proposed to be the primary oxidant in the degradation of organic water contaminants.<sup>38, 39</sup> Therefore, the processes of secondary reactions with activated oxygen are summarized in Figure 2-10. Figure 2-10 shows the oxidation occur by either oxidation via the surface-bound hydroxyl radical (i.e., trapped hole at the  $\text{TiO}_2$  surface) or via the other radicals (i.e., formation of superoxide radicals). And the reduction occurred by directly electrons diffusion under lower conduction states of  $\text{TiO}_2$ . Hence, it is important for the present of oxygen which plays as the primary electron acceptor.<sup>39</sup>

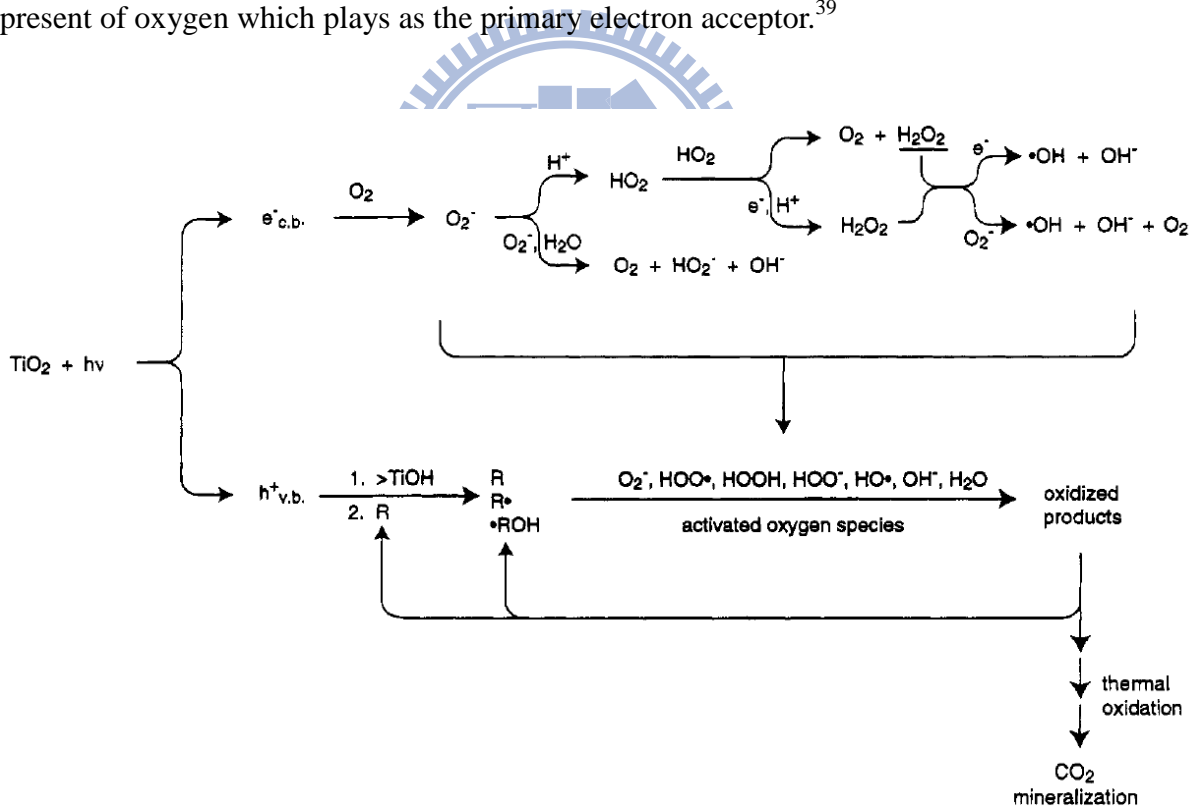


Figure 2-10 Secondary reactions with activated oxygen species in the photoelectrochemical mechanism.<sup>26</sup>



### 2-1-3 Photoassisted degradation of Rhodamine B

In general, the  $\text{TiO}_2$  degrade many organic pollutants and to mineralize completely under UV irradiation.<sup>26, 40</sup> In order to expand the wavelength range in visible light for the photocatalysts, surface sensitization of  $\text{TiO}_2$  via chemical or physic adsorbed dyes molecular were used to promote the efficiency of the charge carrier separation with visible irradiation.<sup>12, 17, 40</sup> For example, the chemisorbed RhB is excited at wavelengths longer than 470 nm to produce singlet and triplet states (denoted here simply as  $\text{RhB}^*_{\text{ads}}$ ). Subsequently,  $\text{RhB}^*_{\text{ads}}$  injects an electron into the conduction band (or to some surface state) of  $\text{TiO}_2$  with RhB being converted to the radical cation  $\text{RhB}^{*+}$ , as shown in Figure 2-11. Afterward, the electrons in the conduction band of  $\text{TiO}_2$  react with adsorbed oxidants, usually  $\text{O}_2$ , to produce reactive oxygen radicals (Equation 2-3 to 2-6).<sup>12</sup> Figure 2-12 shows the de-ethylation reaction since the radical cation  $\text{RhB}^{*+}$  ultimately reacts with reactive oxygen radicals and/or molecular oxygen.<sup>40</sup> Moreover, oxygen plays an additional important role to inhibit recombination between  $\text{RhB}^{*+}$  and  $e^-_{\text{CB}}$ . In addition, the secondary radical processes occurred might lead to mineralization. The semiconductor  $\text{TiO}_2$  acts as an electron-transfer mediator and the oxygen as an electron acceptor leading to efficient separation of the injected electron and the radical cation, thereby facilitating the degradation process.

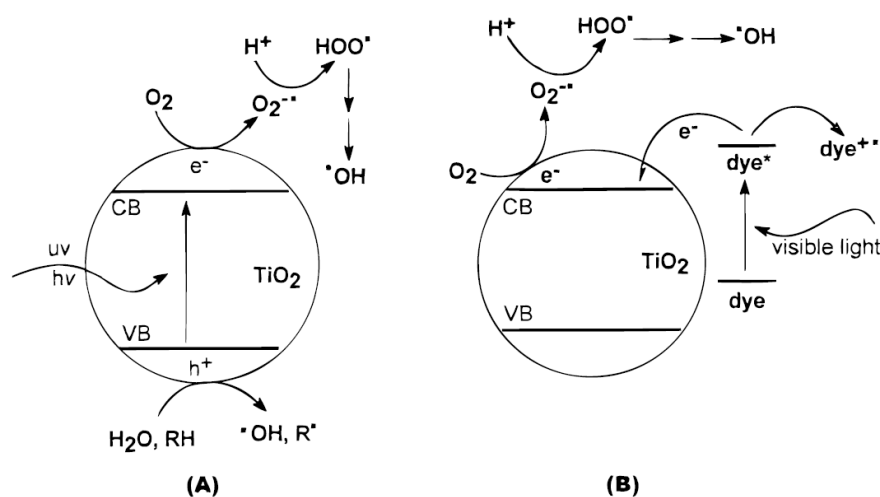


Figure 2-11 Electron-transfer processes (a) for UV irradiation of  $\text{TiO}_2$  with the self-photosensitized pathway (b) under visible light irradiation which subsequent to excitation of RhB dye.<sup>40</sup>

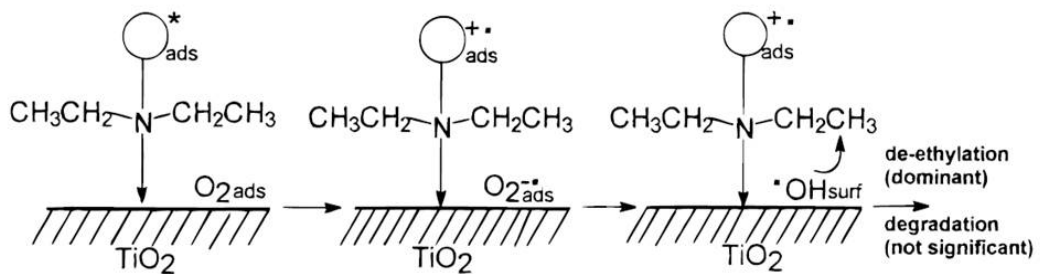
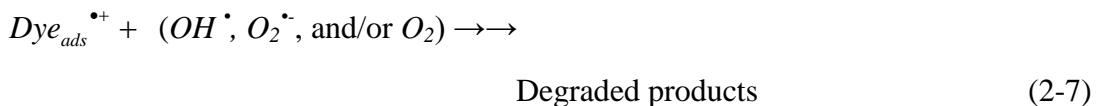


Figure 2-12 Formation and competitive reactions of  $\bullet OH$  radicals during visible light irradiation of Rhodamine B.<sup>22</sup>

## 2-2 Synthesis toward metal oxide

### 2-2-1 Sol-gel method

Sol-gel processes have been widely used to synthesize  $TiO_2$ , because there are many advantages of the sol-gel processes include cheaper, low reaction temperature, uniform structure, extreme purity, selective of precursor and widely applications. The sol-gel process can be characterized by a series of distinct steps.<sup>41</sup>

Step 1: In order to stable solutions of the alkoxide or solvated metal precursor (the *sol*), so the precursor would under hydrolysis and condensation for couple days.

Step 2: After hydrolysis and condensation, gelation resulting from the formation of an oxide- or alcohol-bridged network (the *gel*) by a polycondensation or polyesterification reaction that results in a dramatic increase in the viscosity of the solution. If so desired, the gel may be cast into a mold during this step.

Step 3: Aging of the gel (*syneresis*), during which the polycondensation reactions continue

until the gel transforms into a solid mass, accompanied by contraction of the gel network and expulsion of solvent from the gel pores. Ostwald ripening and phase transformations may occur concurrently with syneresis. The aging process of gels can exceed 7 days and is critical to the prevention of cracks in gels that have been cast.

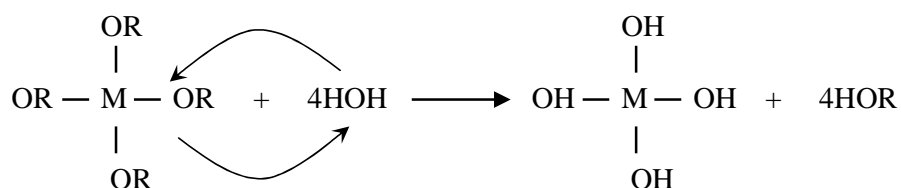
Step 4: Drying of the gel, to remove water and other volatile liquids from the gel network.

This process is complicated due to fundamental changes in the structure of the gel, which was occurred between 100 and 180 °C. If isolated by thermal evaporation, the resulting monolith is termed a *xerogel*. If the solvent is extracted under supercritical or nearsupercritical conditions, the product is an *aerogel*.

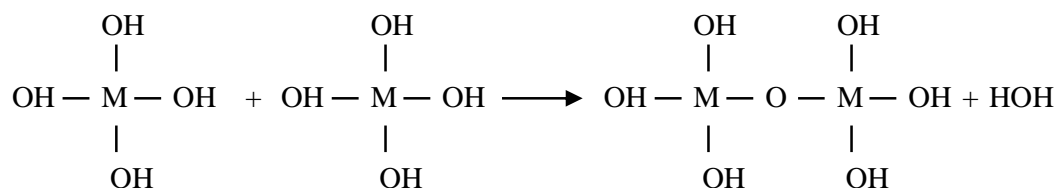
Step 5: Dehydration, during which surface-bound M-OH groups are removed, thereby stabilizing the gel against rehydration. This is normally achieved by calcining the monolith at temperatures up to 800°C. Besides, the calcination processes also cause crystal structure of materials to produce.

Figure 2-13 shows the reaction of sol-gel, including hydrolysis, condensation, and gelation. The hydrolysis occurs by the nucleophilic attack of the oxygen contained in water on the silicon atom as evidenced by the reaction of isotopically labeled water with TEOS that produces only unlabelled alcohol in both acid and basic catalyzed system. Besides, the polymerization to form siloxane bonds occurs by either an alcohol producing condensation reaction or a water-producing condensation reaction. Relative to different condition (i.e. pH), the typical of condensation products is monomer, dimer, linear trimer, cyclic trimer, cyclic tetramer and higher-order rings. In basic condition, particle growth in size with decrease in number; in acid condition, the particles aggregate into three-dimensional networks and form gel. So, the structure was linear or randomly branched polymer under acid condition, while it was branched cluster under basic condition. And the final process is drying and calcination which lead to the structure of gels stable by thermal treatment.<sup>41</sup> In addition, Figure 2-14 shows the processing steps involved in making sol-gel-derived.

(a) Hydrolysis



(b) Condensation



(c) Gelation

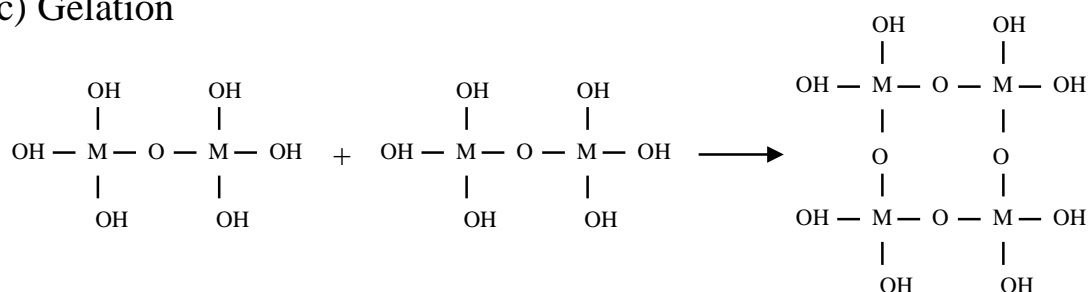


Figure 2-13 The process of sol-gel under acid condition. (a)Hydrolysis, (b)Condensation, and (c)Gelation.<sup>41</sup>

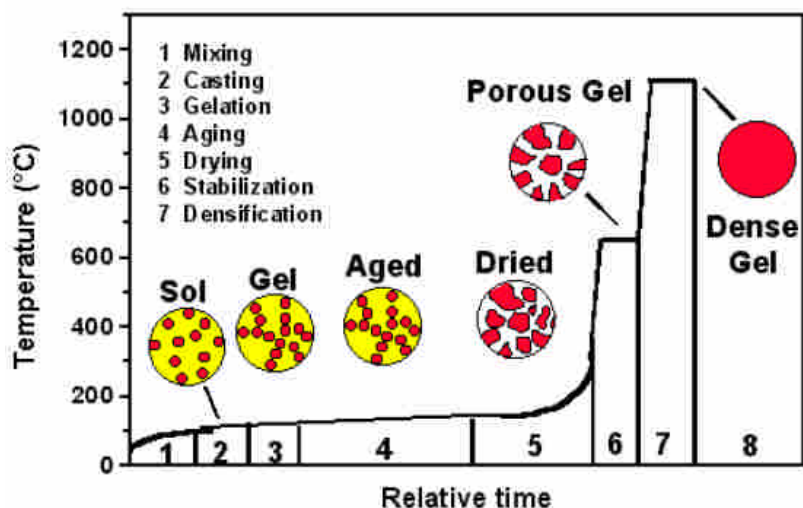


Figure 2-14 Gel process sequence.<sup>42, 43</sup>

Generally speaking, the transition metal systems are distinguished from silicates by greater chemical reactivity resulting from the lower electronegativity of the metal and its

ability to exhibit several coordination states, so that coordination expansion occurs spontaneously upon reaction with water or other nucleophilic reagents.<sup>44</sup> Therefore, the sol-gel processes of silicon and titanium precursors were similar, silicon was used to make example in this study. Sol-gel processes appear to be a simple operation, but several variables can influence the properties of the final products. Such as, pH of the reaction medium, water:alkoxide ratio, reaction temperature, and polarity of solvent. Therefore, by varying these processing parameters, materials with different physicochemical properties can be obtained. Thus the different parameters were introduced below.

The introduction of water to the  $\text{Si}(\text{OR})_2$  precursor initiates hydrolysis, as shown in Figure 2-15. The water:alkoxide ratio determines the sol-gel chemistry and the structural characteristics of the hydrolyzed gel. High water:alkoxide ratios in the reaction medium ensure a more complete hydrolysis of alkoxides, favoring nucleation versus particle growth. Thus precursor solution reacts very quickly with water especially in the presence of excess of water. The rapid initial hydrolysis results a solution with a high degree of supersaturation of hydroxylated metal oxide. This leads to a high rate of nucleation and the formation of small particles or crystallites.<sup>44, 45</sup>

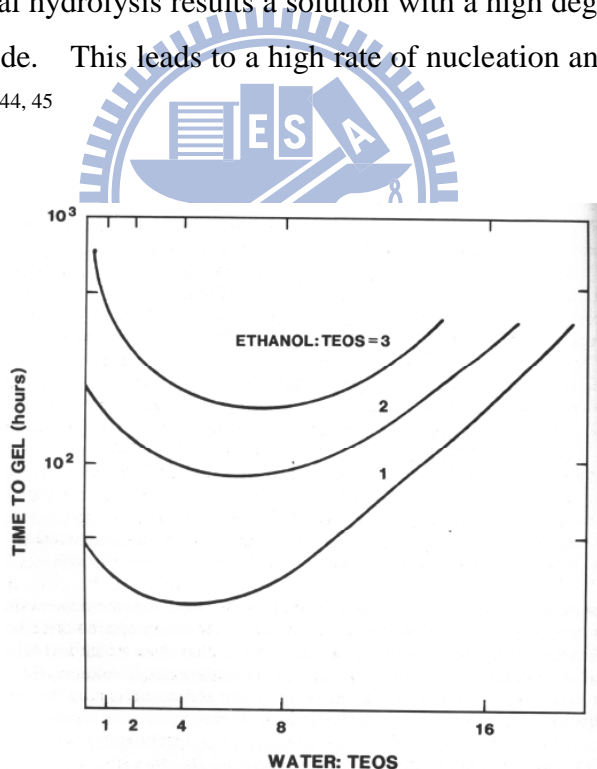


Figure 2-15 The relationship between gelation times and  $\text{H}_2\text{O}$ :alkoxide ratio.<sup>44</sup>

Whether the hydrolysis is acid or base catalyzed also has important consequences for the structure of the resulting gel network. For acidic conditions ( $\text{pH} < 4$ ), the rate of hydrolysis will always exhibit faster kinetics than the rate of condensation due to the ability of  $-\text{OR}$  groups to better stabilize the transition states. Besides, the gelatin process was delayed in

the synthesis with HCl addition, so that a turbid gel was formed instead of white precipitates. HCl serves not only as an acid catalyst, but also as an electrolyte to prevent particle growth or agglomeration through electrostatic repulsion.<sup>46</sup> Besides, under basic conditions, the silica products tend to form large agglomerates that eventually cross-link.<sup>44</sup> Therefore, the differences between acid and base catalyzed reactions and the consequences for particle morphology are conceptually represented in Figure 2-16.

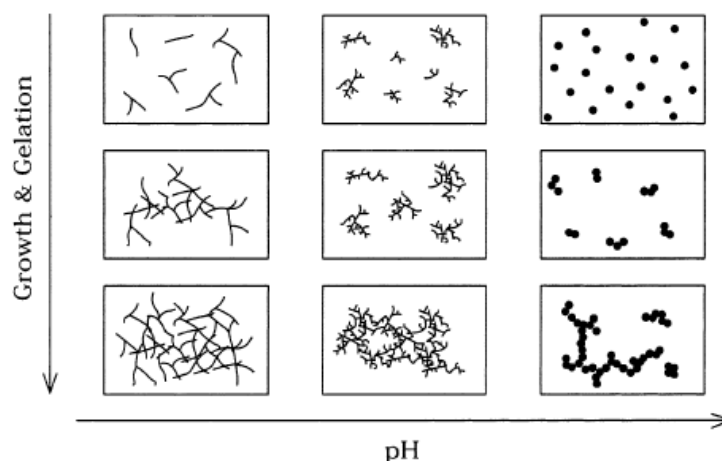


Figure 2-16 The different structure of particles depend on pH.<sup>41</sup>

The polarity of solvent affects the hydrolysis process, because the hydrolysis reaction proceeds via nucleophilic reaction mechanism with  $\text{OH}^-$  as the nucleophile. This phenomenon facilitate further attack of the nucleophile on the silicon atom which is more positive charge on the silicon atom after the hydrolysis of the first alkoxy group, because  $\text{OH}^-$  is a marginally better leaving group than  $-\text{OR}$  while the condensation process can occur. Thus, the rate of hydrolysis and condensation reaction followed sequence 1-butanol > methanol > 1-propanol > ethanol > 2-propanol, because the reaction rate was caused by hydrogen bonding and steric effect in solvent alcohol. If the hydrogen bonding ability is the only one factor, then increasing hydrogen bonding ability of solvent decreases the mobility of water to react with TEOS while the rate of hydrolysis reaction followed order 1-butanol > methanol > 1-propanol > ethanol > 2-propanol.<sup>47, 48</sup> However, in order to slow down the rate of hydrolysis, 2-propanol is the better chose for solvent.

### 2-2-2 Surface sol-gel method

In addition to sol-gel method, surface sol-gel can fabricate ultra-thin films with molecular-scale. Figure 2-17 shows the process of surface sol-gel. This process is

composed of chemisorption of alkoxide, rinse, hydrolysis of the chemisorbed alkoxides, and drying.<sup>44, 49</sup> The moving substrate entrains liquid in a fluid mechanical boundary layer carrying some of the liquid toward the deposition region, where the boundary layers split in two (see Figure 2-18). The inner layer moves upward with the substrate, while the outer layer is returned to the bath. The thickness of the deposited film is related to the position of the streamline dividing the upward- and downward-moving layers.

Therefore, there are six forces in the film deposition region govern the film thickness and position of the streamline: (1) viscous drag upward on the liquid by the moving substrate, (2) force of gravity, (3) resultant force of surface tension liquid in the concavely curved meniscus, (4) inertial force of the boundary layer liquid arriving at the deposition region, (5) surface tension gradient and (6) the disjoining or conjoining pressure (important for films less than 1  $\mu\text{m}$  thick). When the liquid viscosity and substrate speed are high enough to lower the curvature of the meniscus, then the deposited film thickness balances the viscous drag and gravity force.<sup>44</sup>

According to surface sol-gel principle, the process could be applied to various materials surfaces irrespective of their shape, size and structure. Besides, it is applicable to a wide range of metal precursor (metal alkoxides).<sup>49</sup> Therefore, the reaction between the surface  $\text{TiO}_2$  hydroxyl groups with vanadia precursor molecules is therefore the best route to obtain well-defined surface concentrations of vanadium. However, Figure 2-19 shows the structure of production was prepared with different path way.

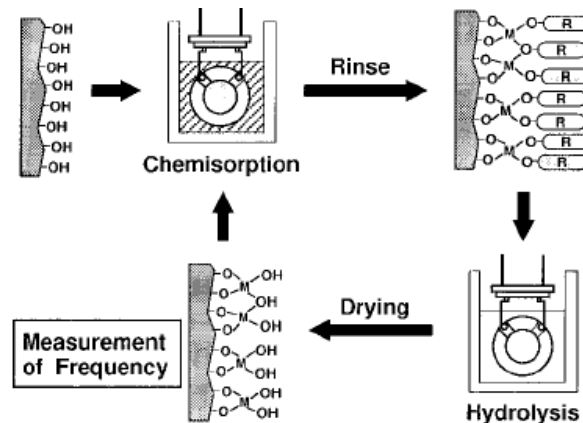


Figure 2-17 Schematic representation of the surface sol-gel process.<sup>49</sup>

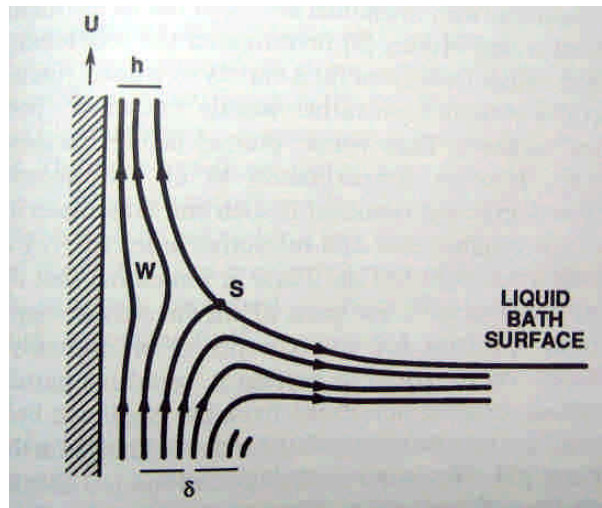


Figure 2-18 Detail of liquid flow patterns of the continuous process.  $U$  is the withdrawal speed,  $S$  is the station point,  $\delta$  is the boundary layer, and  $h$  is the thickness of the fluid film.<sup>44</sup>

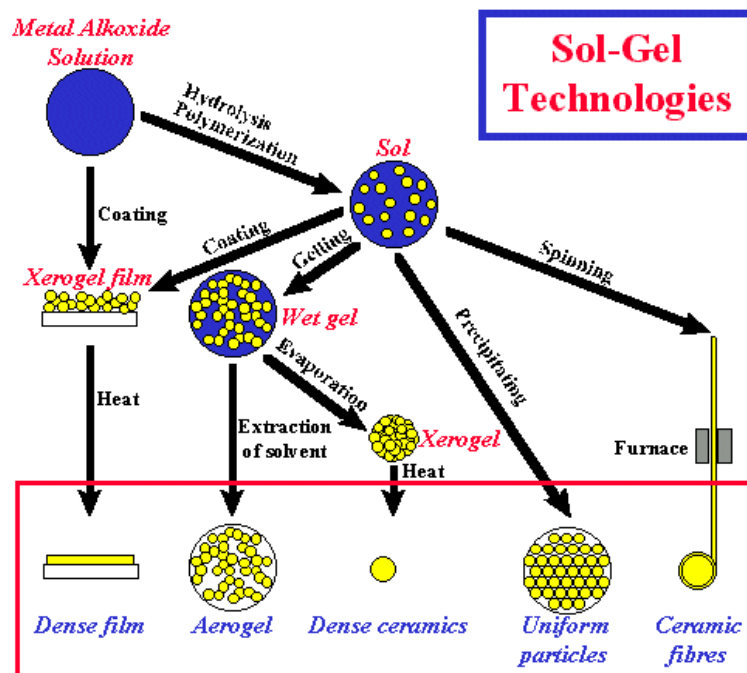


Figure 2-19 The production prepared by sol-gel-derived with different processes.<sup>42, 44</sup>

### 2-3 Doping TiO<sub>2</sub> with impurities

Photocatalytic activity of a particular semiconductor system for the stated purpose is measured by several factors including the stability of the semiconductor under irradiation, the efficiency of the photocatalytic process, the selectivity of the products, and the wavelength range response. Therefore, photocatalyst for a particular use can be surmounted by modifying the surface of the semiconductor. Three benefits of modifications to



photocatalytic semiconductor systems have been studied: (1) inhibiting recombination by increasing the charge separation; (2) increasing the wavelength response range (i.e. excitation of wide band gap semiconductors by visible light); and (3) changing the selectivity or yield of a particular product. For examples, impurities like transition metal ions (Fe, V)<sup>2-5, 50</sup>, and non-metal ions (N, C)<sup>7-9</sup> were mostly used to dope into crystalline structure of TiO<sub>2</sub> to vary some physicochemical properties of original TiO<sub>2</sub>, including microstructure, electronic structure, and photocatalysis.

In order to define the structure of vanadium doped in TiO<sub>2</sub>, the catalysts have been studied by in situ FT-Raman. Figure 2-20 and Figure 2-21 show the structure of surface and bulk doped materials. For surface doped materials, there are two kinds of forms of VO<sub>x</sub> species attached to the TiO<sub>2</sub> surface: monomeric vanadyl and polymeric vanadates.<sup>51-53</sup> In particular, the coordination of the surface oxygen atoms plays a key role in reactivity. All of the potentially active oxygen sites proposed to be vanadyl V=O (1030 cm<sup>-1</sup>), bridging V-O-V (822 cm<sup>-1</sup>), interface V-O-Ti, and surface Ti-O-Ti (638 cm<sup>-1</sup>). For hydrogen atomic adsorption, the most reactive sites are those located at the interface between the V<sub>2</sub>O<sub>5</sub> and the TiO<sub>2</sub> unit (V-O-Ti), while the vanadyl V=O bonds are more stable.<sup>53, 54</sup> So, while the number of vanadium centers in the polyvanadates increase, the number of terminal V=O (930 cm<sup>-1</sup>) groups per vanadium decreases to accommodate V-O-V (822 cm<sup>-1</sup>) linkages.<sup>51-53</sup> It meant the vanadium ions were preferred to perform V<sub>2</sub>O<sub>5</sub> under higher vanadium concentration. For bulk doped materials, the V<sup>4+</sup> ions were substituted Ti<sup>4+</sup> of TiO<sub>2</sub> structure, because two cations have the similar ionic charge ( $rV_{6c}^{4+} = 0.590 \text{ \AA}$  and  $rTi_{6c}^{4+} = 0.605 \text{ \AA}$ ).<sup>55</sup>

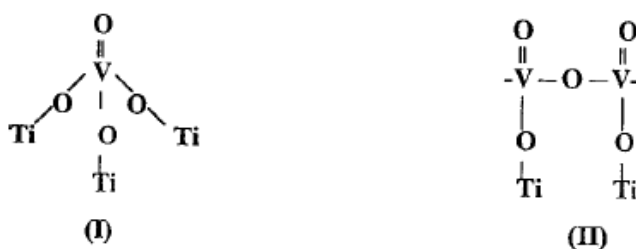


Figure 2-20 The structure of surface doped materials.<sup>52</sup>

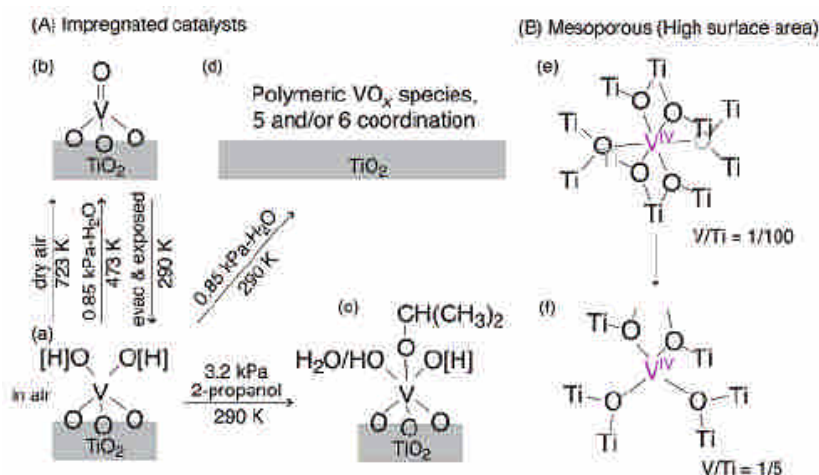


Figure 2-21 Proposed V site transformations for V/TiO<sub>2</sub> in surface doped materials (A) and for bulk doped materials (B). [H] for models a and c indicates the presence/absence of hydrogen cannot be determined.<sup>55</sup>

Figure 2-22 shows the bonding diagram of the TiO<sub>2</sub> perfect crystal (rutile). The conduction band (CB) and valence band (VB) of TiO<sub>2</sub> mainly consist of the Ti 3d and O 2p states, respectively. Besides, the bottom of the lower CB consisting of the T d<sub>xy</sub> orbital contributes to the metal-metal interactions due to the  $\sigma$  bonding of the Ti t<sub>2g</sub> – Ti t<sub>2g</sub> states.<sup>56</sup> Therefore, if transition metal ions doped in TiO<sub>2</sub>, the bandgap energy of TiO<sub>2</sub> shifted a lower energy due to extra energy level caused by 3d dopants (transition metal ions).<sup>5</sup> So, in case of V/TiO<sub>2</sub>, total density of electrons is shown in Figure 2-23. The V<sup>5+</sup>/V<sup>4+</sup> redox level was lied 1.4 eV above the top of the valence band in rutile. The V<sup>4+</sup>/V<sup>3+</sup> level lies 0.8 eV below the bottom of the conduction band.<sup>29, 57</sup> While both redox levels remain with the band gap in the TiO<sub>2</sub> colloids, both holes and electrons can be trapped by V<sup>4+</sup> which will cause disappearance of the V<sup>4+</sup> EPR signal.<sup>29, 57</sup>

In order to define hyperfine parameter of various species containing a V<sup>4+</sup> paramagnetic ion, I have used subscripts 6c, 5c and 4c to stand hexa-, penta-, and tetraordinated V<sup>4+</sup> species. In this notation, vanadyl ions are formally labeled (VO<sup>2+</sup>)<sub>ic</sub> were referred to the global vanadium coordination. However, there are three distinct ligand field geometries can thus be distinguished, as shown below.<sup>58</sup>

1. Vanadyl ions in a square pyramidal (VO<sup>2+</sup>)<sub>5c</sub> or in an axially distorted octahedral symmetry (VO<sup>2+</sup>)<sub>6c</sub>. ( $g = 1.955 \sim 1.980$ )
2. Vanadium ions in a tetrahedral geometry, (V<sup>4+</sup>)<sub>4c</sub>.
3. Vanadium ions in a biaxially distorted octahedral symmetry, (V<sup>4+</sup>)<sub>6c</sub>. ( $g = 1.920 \sim$

1.950)

Moreover, the coordination sphere of these vanadyl ions ( $\text{VO}^{2+}$ ) may then be completed either by some surface oxygen anions ( $\text{O}^{2-}$ ) of the  $\text{TiO}_2$  sublattice or by adsorbed water molecules. And  $(\text{V}^{4+})_{6c}$  is shown a vanadium ions located at the center of the rutile unit cell is surrounded by a slightly distorted oxygen octahedron.<sup>58</sup>

In addition, the atomic ratio of V/Ti can influence the electronic structure. Figure 2-24 shows the band model of  $\text{Ti}_{1-x}\text{V}_x\text{O}_2$  at bias potential of 1V vs. SCE in an electrolyte solution at various atomic ratio of V/Ti. For V/Ti = 0.025 and 0.05 samples, the recombination time was larger than V/Ti=0 sample, because the V 3d level in the bandgap inhibited the electron-hole recombination. But, it seemed the increasing photocurrent with the potential was stronger for V/Ti  $\geq$  0.1 samples. This can probably be ascribed to the connection of the filled V 3d level with the conduction band, which result in the semi-metal behavior. Summary, the different atomic ratio of V/Ti can influence the electronic structure of materials.

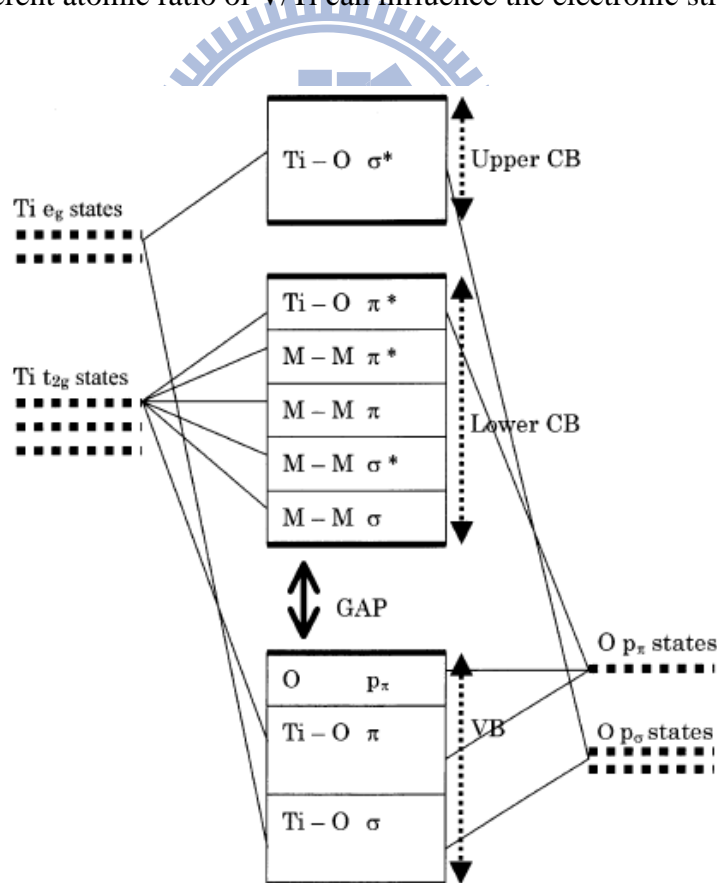


Figure 2-22 The bonding diagram of the  $\text{TiO}_2$  perfect crystal (rutile) proposed by Soratin and Schwarz.<sup>5, 56</sup>

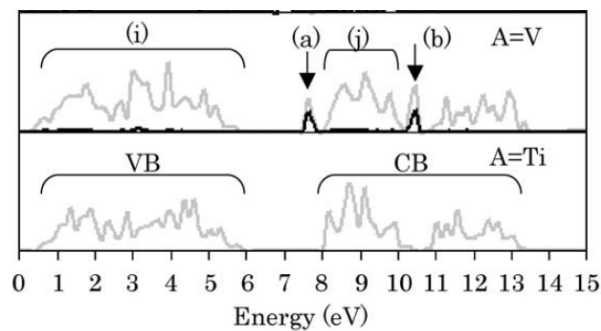


Figure 2-23 The DOS of metal-doped  $\text{TiO}_2$  ( $\text{Ti}_{1-x}\text{A}_x\text{O}_2$ ;  $\text{A}=\text{V}$  or  $\text{Ti}$ ). Gray lines means total DOS and black lines shows dopant's DOS.<sup>5</sup>

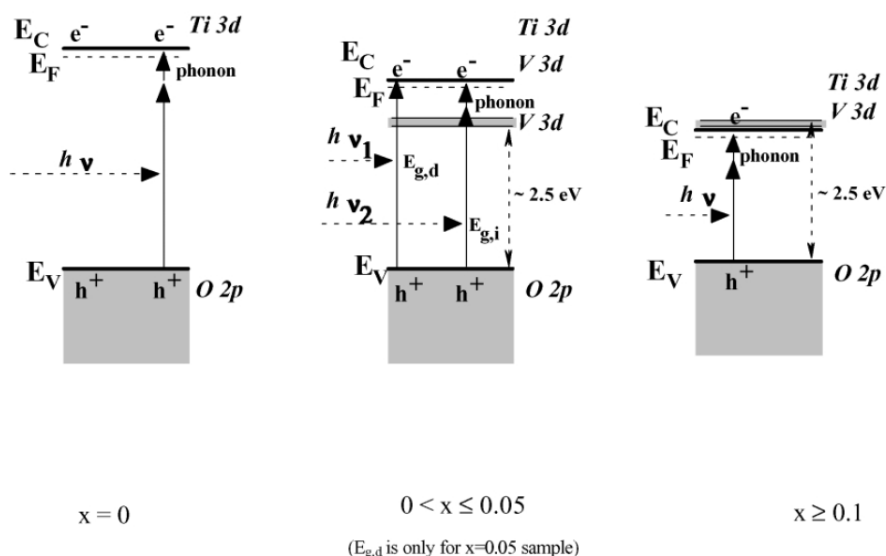
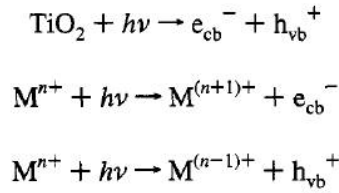


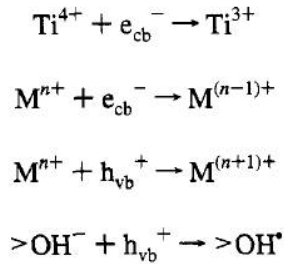
Figure 2-24 Band model of  $\text{Ti}_{1-x}\text{V}_x\text{O}_2$  film electrodes at bias potential of 1 V vs. SCE in an electrolyte solution.<sup>59</sup>

The extra energy caused by dopant affect photocatalysis of  $\text{TiO}_2$  because the defect performed by dopants can trap either an electron or a hole alone.<sup>29</sup> So, a general photochemical charge-trapping, recombination, detrapping, and migration mechanism in the presence of transition metal ion dopants is proposed as Figure 2-25:

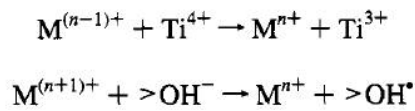
charge pair generation



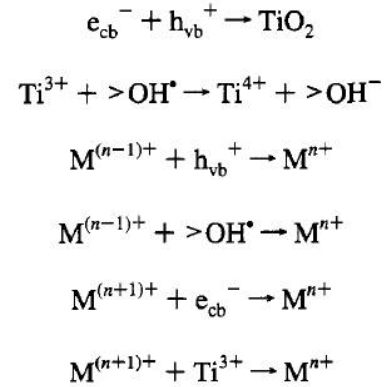
charge trapping



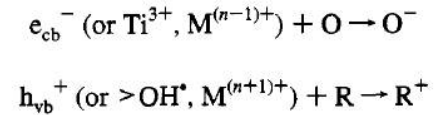
charge release and migration



recombination



interfacial charge transfer



**Where  $\text{M}^{n+}$  is a metal ion dopant, O is an electron acceptor (oxidant), and R is an electron donor (reductant).**

Figure 2-25 The photochemical mechanism in the present of transition metal ions.<sup>29</sup>

It has hypothesized that the addition of transition metals to titania increases the rate of photocatalytic oxidation, due to the electron scavenging by the transition metal ions at the semiconductor surface through the following reaction :  $\text{M}^{n+} + e_{\text{CB}}^- \rightarrow \text{M}^{(n-1)+}$ , where  $\text{M}^{n+}$  represents transition metal ions.<sup>60</sup> This reaction prevents electron-hole recombination and results in an increase rate of formation of  $\bullet\text{OH}$  radical. Besides, when dopant acts as both electrons trapping and holes trapping, it would decrease the rate of recombination. For example, the present of vanadium in the  $\text{TiO}_2$  lattice act as both electrons and holes trapping. Thus, the photoactivity of  $\text{V}^{5+}$  is significantly higher than the photoactivity of  $\text{V}^{4+}$ .<sup>29</sup>

## 2-4 Bulk and surface doping sites

Lee et al. reported<sup>19</sup> that the surface levels of TiO<sub>2</sub> were the levels of mixed orbitals, which are composed of 3d orbitals of Ti and 2p orbitals of the surface oxygen. Therefore, the electronic density of bulk and surface are different, which is shown in Figure 2-26. The effect of vanadium doping positions on the electronic structure of TiO<sub>2</sub> could be different. Most of the dopant levels related to the surface are found between conduction and valence bands of bulk TiO<sub>2</sub>. Therefore, it is expected that the doping of a transition metal to a TiO<sub>2</sub> surface increases the surface trapping rate of carrier electrons and the trapping effect becomes larger with increasing in the atomic number of a transition metal dopant. Lee et al.<sup>19</sup> reported that the number and energy of surface levels are deeply affected by impurities found on the surface of TiO<sub>2</sub>. And the trapping time of carrier electrons at the surface level become longer with an increase in  $\Delta E_{\text{surface}}$ . ( $\Delta E_{\text{surface}}$  means the energy different LUMO of bulk TiO<sub>2</sub> and the lowest dopant level). It refers that transition metal doped on TiO<sub>2</sub> surface increases the surface trapping rate of carrier electrons. However, the bulk doping site caused by transition metals performed extra energy level between VB and CB. Although the defects retard the charge recombination by trapping, the trapped electrons/holes can not migrate to substance surface for following reduction or oxidation of adsorbed reactants. Thus, the surface doping sites can promote the electrons to transfer to surface efficiently, while bulk doing sites could be detrimental to the photocatalytic activity. However, there are few papers to discuss the mechanism of photocatalysis with different V-doping positions.

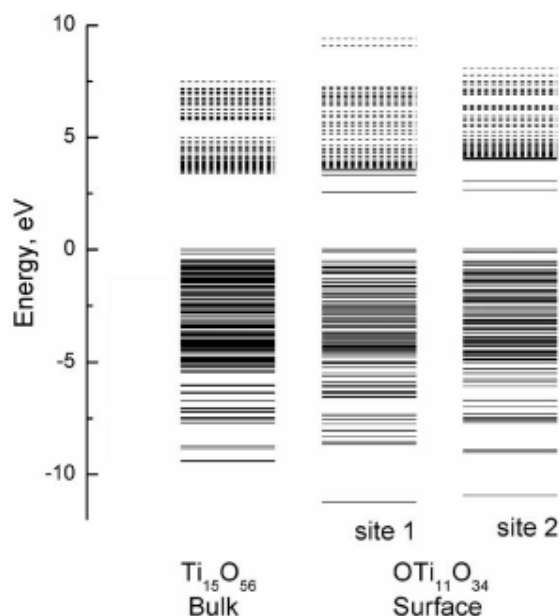


Figure 2-26 The energy level diagram calculated using large cluster models of  $(\text{Ti}_{15}\text{O}_{56})^{52-}$  and  $(\text{Ti}_{11}\text{O}_{34})^{24-}\text{O}^*$  corresponding to the bulk and surface of rutile  $\text{TiO}_2$ .<sup>19</sup>

Doping  $\text{TiO}_2$  with  $\text{V}^{4+}/\text{V}^{5+}$  at different sites also influences the crystal structures. Balikdjian and Davidson et al<sup>16</sup> reported that the presence of V species into the bulk lattice of anatase did not affect the transformation of anatase into rutile, but the V species deposited on the surface of anatase grain boundary favored rutile transformation. In addition, the particle sizes of  $\text{TiO}_2$  become small after doping with  $\text{V}^{5+}$  ions and result in significant band bending.<sup>10</sup> To fully understand the influence of doping on the nature and extent of charge transfer, particle size and crystal structure need to be investigated.<sup>10, 61</sup>

In heterogeneous system, the photoactivity occurs on the surface of materials. The defects on the  $\text{TiO}_2$  surface are easily formed by thermal treatment because the oxygen vacancy site leaves an exposed  $\text{Ti}^{3+}$  ion which may be visualized as a  $\text{Ti}^{4+}$  ion associated with a somewhat localized electron. In addition, the exposed  $\text{Ti}^{3+}$  atoms diffuse from the bulk to the surface during calcination, so the thermal treatment causes the incorporation of oxygen vacancy into the surface layer of  $\text{TiO}_2$ . Surface trapping sites were supposed to promote the photocatalytic activity efficiency than bulk trapping sites due to a lack of surface oxygen defects. Figure 2-27 shows bulk and surface trapping sites, respectively. The electrons trapped by bulk defect called bulk trapping, and the electrons trapped by surface defect called surface trapping. However, there are too less papers to discuss the difference between bulk and surface doping sites on physiochemical properties of V-doped materials.

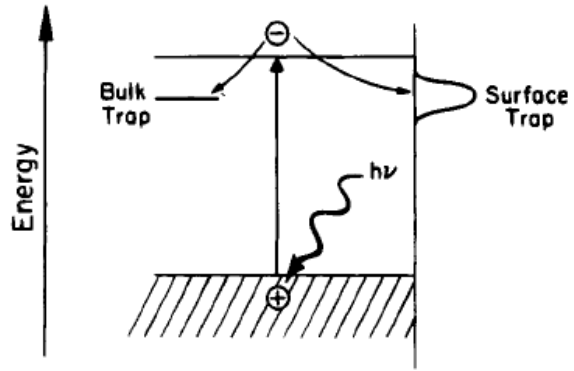


Figure 2-27 Surface and bulk electron carrier trapping.<sup>17</sup>



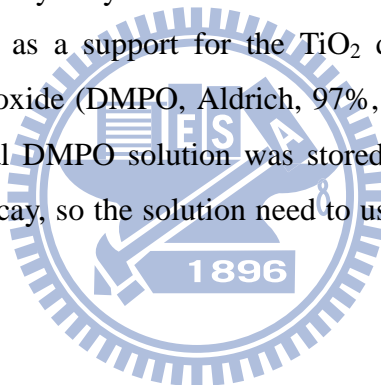


## Chapter 3 Materials and methods

Figure 3-1 shows the flow chart of the experimental design in this study. Catalysts are synthesized with sol-gel and surface sol-gel methods.

### 3-1 Materials

Titanium isopropoxide (TTIP, Acros, 98 %+) and vanadium (V) oxytriisopropoxide (VTIP, Aldrich, 99 %+) were used as the precursors of titania and vanadium, respectively. 2-propanol ( $C_3H_7OH$ , J.Backer, 100 %) was used as solvent to dissolve titanium isopropoxide and vanadium (V) triisopropoxide. Rohdamine B (RhB,  $C_{28}H_{31}N_2O_3Cl$ , Sigma Aldrich, Dye content 95 %) was used as the target compound for photocatalysis and its structure is shown in Figure 3-2. Hydrogen acid (HCl, Crown, 35 ~ 37 %) was used to adjust the pH of sol solution to slow down the hydrolysis. Filter membrane (Critical, 47 mm in diameter, 0.2  $\mu m$  in pore size) was used as a support for the  $TiO_2$  during its surface coating process. 5,5-dimethyl-1-pyrroline N-oxide (DMPO, Aldrich, 97%,  $d= 1.05$  g/mL) was used as a  $\bullet OH$  trapped agent. The original DMPO solution was stored at  $- 25$  °C. In addition, DMPO diluted by DI water were decay, so the solution need to use immediately for least 2 two days stored at 4 °C.



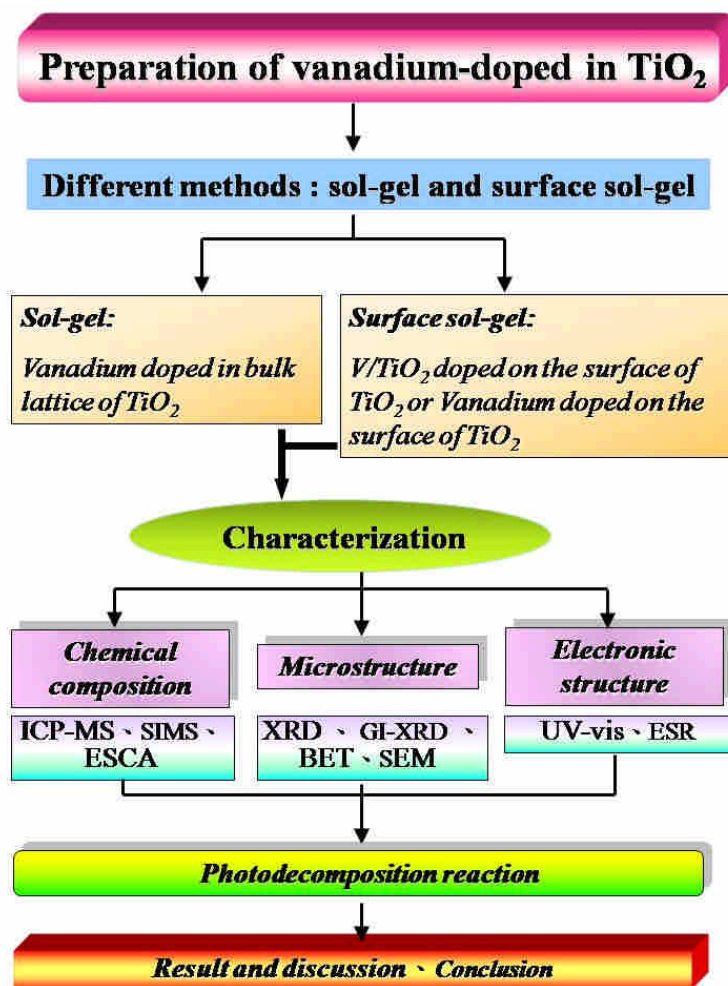


Figure 3-1 Flow chart of experimental design in this study.

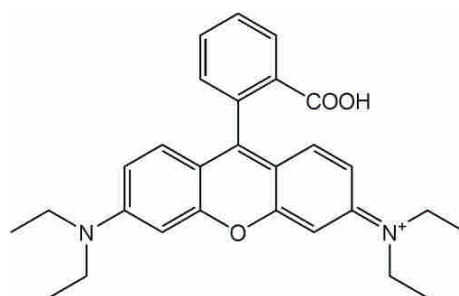
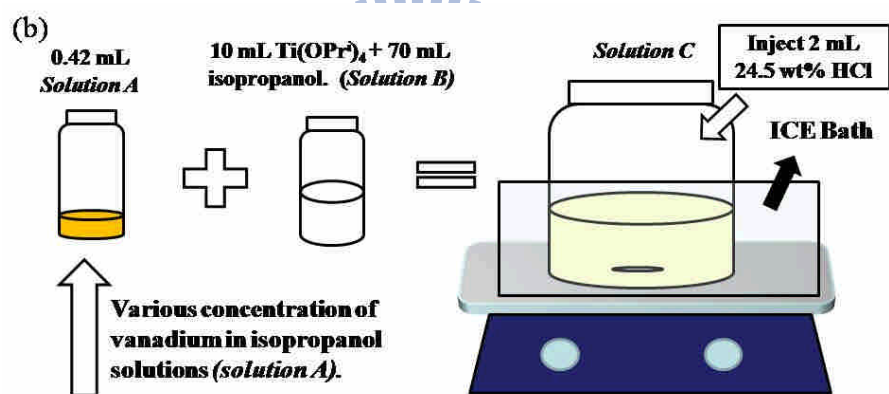
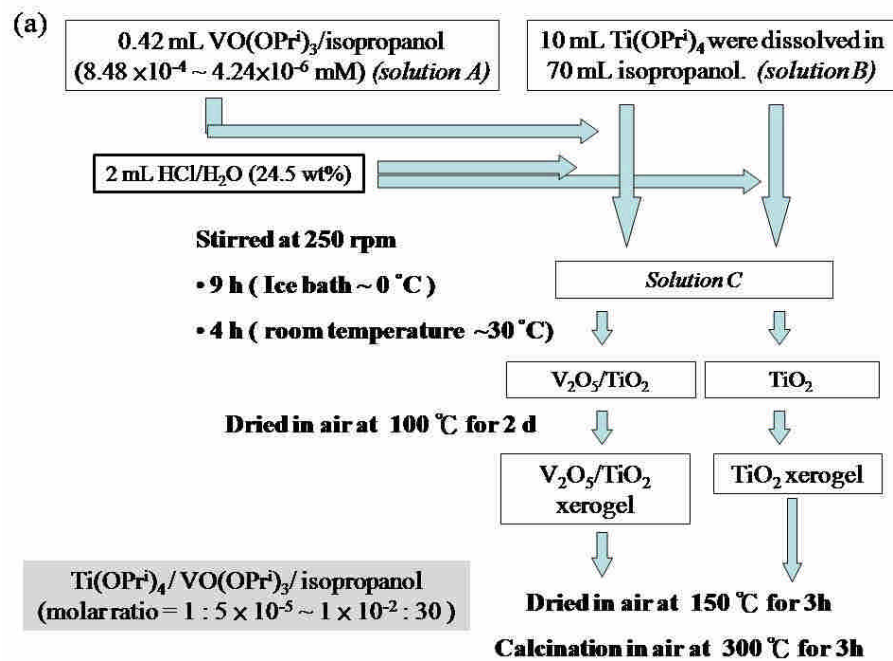


Figure 3-2 The chemical structure of RhB.

### 3-2 Preparation of bulk doped TiO<sub>2</sub> via sol-gel process

Figure 3-3 shows the preparation procedure for bulk doped TiO<sub>2</sub>. Firstly, TTIP and VTIP were dissolved in 70 mL isopropanol in sample vials (110 mL) to reach various V/Ti atomic ratios ( $1 \times 10^{-5} \sim 1 \times 10^{-2}$ ). Then, 2 mL hydrogen chlorate acid (24.5%, HCl) was injected into the mixtures at 4°C with stirring at 250 rpm. The solutions were maintained at this temperature for 9 h to complete the hydrolysis of TTIP and VTIP. Afterward, the solutions underwent gelation at room temperature for 4 h. The doped TiO<sub>2</sub> powders were obtained through evaporating solvent at 100°C for 2 d followed by 150°C for 3 h. The solids were then calcined under air at 300 °C for 3 h. The resulting xerogels were called VT.





<i>Solution A</i>	Vanadium precursors	Isopropanol
$8.48 \times 10^{-4}$ mM	0.21 mL $\text{VO}(\text{Pr})_3$	0.84 mL
$8.48 \times 10^{-5}$ mM	0.21 mL ( $8.48 \times 10^{-4}$ mM $\text{VO}(\text{Pr})_3/\text{IPA}^a$ )	1.89 mL
$4.24 \times 10^{-5}$ mM	0.21 mL ( $8.48 \times 10^{-4}$ mM $\text{VO}(\text{Pr})_3/\text{IPA}^a$ )	3.99 mL
$8.48 \times 10^{-6}$ mM	0.21 mL ( $8.48 \times 10^{-5}$ mM $\text{VO}(\text{Pr})_3/\text{IPA}^a$ )	1.89 mL
$4.24 \times 10^{-6}$ mM	0.21 mL ( $4.24 \times 10^{-5}$ mM $\text{VO}(\text{Pr})_3/\text{IPA}^a$ )	1.89 mL

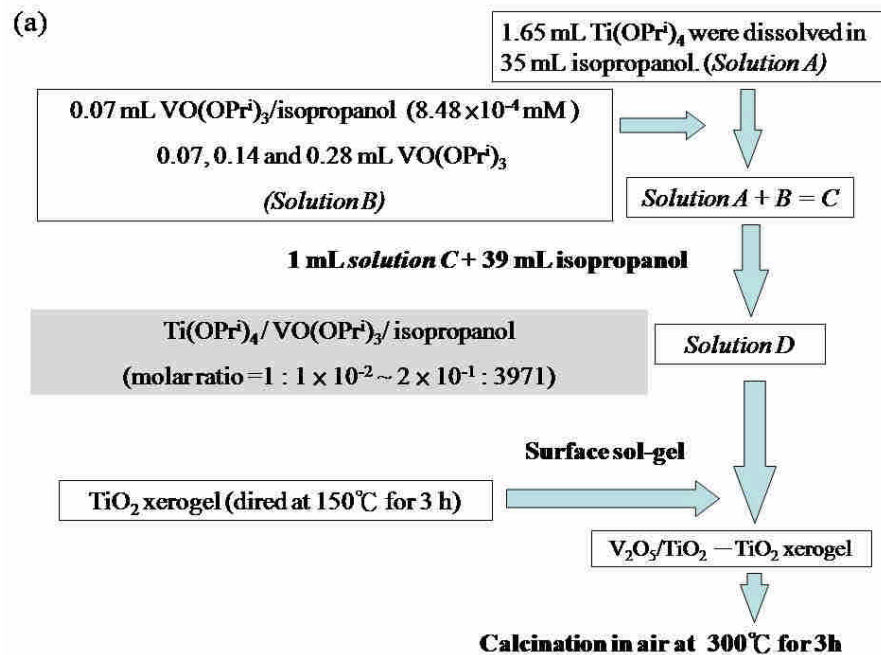
<sup>a</sup> Isopropanol.

Figure 3-3 The synthetic process of bulk doped materials. (a) the flow charts of the synthesis and (b) the recipes of precursor solutions.

### 3-3 Preparation of surface doped TiO<sub>2</sub> via surface sol-gel process

Figure 3-4 shows the preparation procedure for surface doped TiO<sub>2</sub>. Surface doped materials were prepared via coating a thin V-doped TiO<sub>2</sub> layer onto TiO<sub>2</sub> using surface sol-gel process. Figure 3-5 shows the carton and photograph of surface sol-gel system. Moreover, the dried TiO<sub>2</sub> powders were obtained through evaporating solvent at 100°C for 2 d followed by 150°C for 3 h. The dried TiO<sub>2</sub> powders were stood between Teflon and filter paper, which were immersed in shallow container filled with *solution D*. And the *solution D* at different TTIP/VTIP atomic ratios was prepared as following: Firstly, TTIP and VTIP were dissolved in 35 mL isopropanol to reach varies VTIP/TTIP atomic ratios ( $1 \times 10^{-2} \sim 2 \times 10^{-1}$ ). Then, 1 mL of above mixing solution (*solution C*) was injected into 39 mL isopropanol for dilution, and the diluted solutions were named *solution D*, as shown in Figure 3-4.

The dried TiO<sub>2</sub> powders were immersed in *solution D* about 10 minutes. Then the dried TiO<sub>2</sub> were raised by hand and then the powders were separated from diluted precursor by gravity. Afterward, the solids were dried at 100 °C for few minutes and then were calcined at 300 °C for 3 h. The resulting xerogels obtained were named SVT. In addition, the pure V<sub>2</sub>O<sub>5</sub> coated on the surface of TiO<sub>2</sub> were named SVTP, which was shown in Appendix F. To summary the structures of bulk doped and surface doped TiO<sub>2</sub>, Figure 3-6 shows the three type materials in this study.



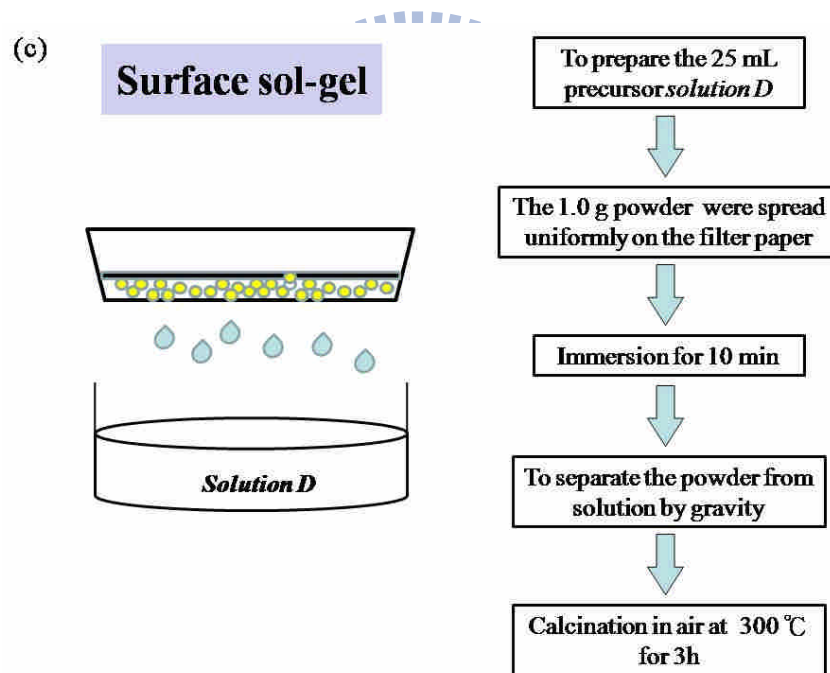
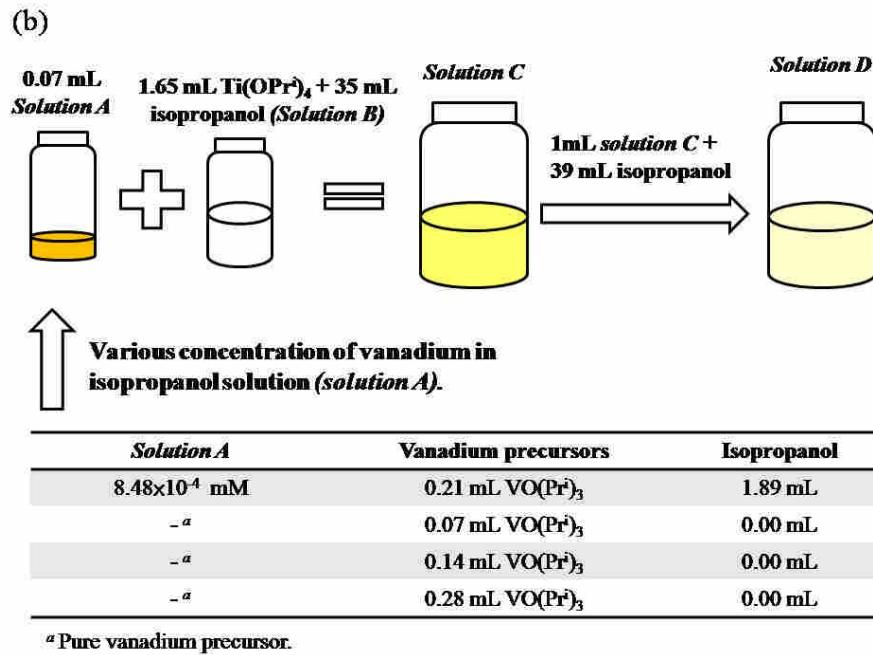


Figure 3-4 The synthetic process of surface doped materials. (a) the flow charts of the synthesis of surface doped materials, (b) the recipes of precursor solutions, and (c) the surface sol-gel processes for coating.

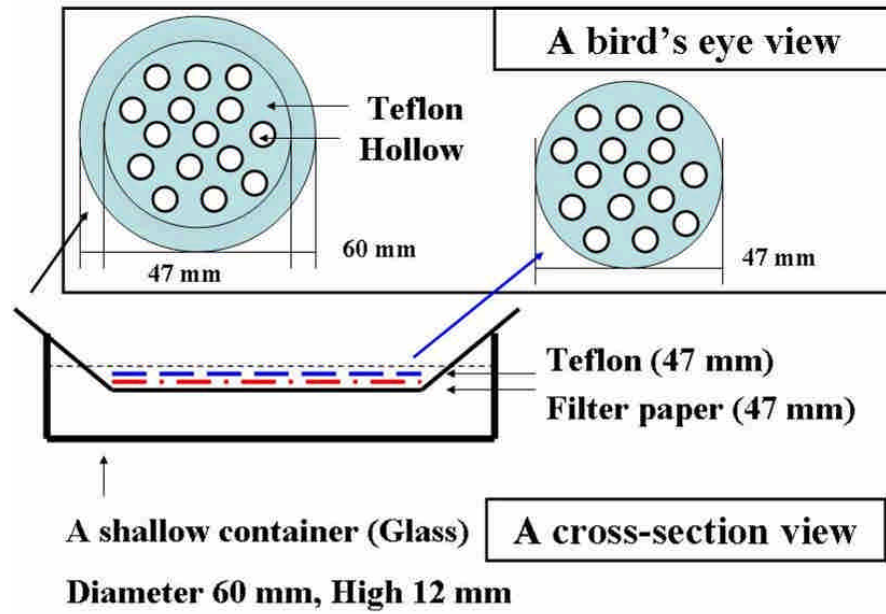


Figure 3-5 A design chart and a photograph of surface sol-gel system.

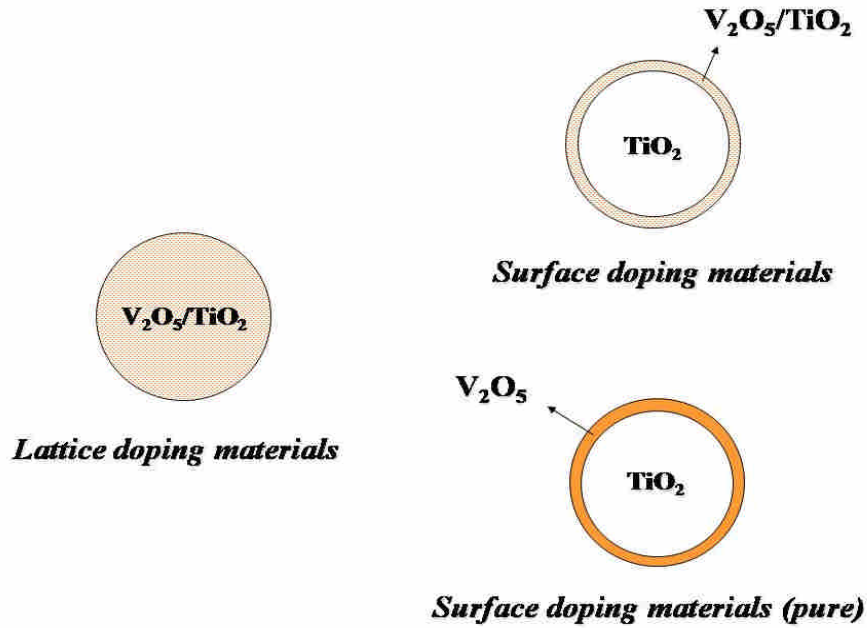


Figure 3-6 The geometric structure of pure, bulk and surface doped TiO<sub>2</sub>.

### 3-4 Characterization

#### 3-4-1 X-ray photoelectron spectroscopy (XPS)

XPS measurements were performed with an ESCA PHI 1600 spectrometer using an Al K $\alpha$  radiation (1486.6 eV). The photoelectrons were collected into the analyzer with a 23.5 eV pass energy. The collection step size in wide range scan and high-resolution analysis are 1.0 eV and 0.1 eV, respectively. All analytical process was controlled under ultrahigh vacuum at the pressure below  $1.4 \times 10^{-9}$  Torr. In addition, bulk chemical compositions were detected after etching by Ar ion for 60 seconds. At low V loading, a charging effect occurs and was corrected using the C 1s peak at 284.8 eV as a reference. For advanced qualification and quantification of each element, curve fitting of XPS spectra was performed on program. The atomic ratio was calculated from the integrated peak areas normalized to sensitive factors. The equation for atomic ratio calculation is shown:

$$\frac{n_1}{n_2} = \frac{I_1/ASF_1}{I_2/ASF_2} = \frac{A_1/ASF_1}{A_2/ASF_2} \quad (3-1)$$

Where  $n$  denotes the atomic numbers,  $I$  is the intensity of species on XPS spectra,  $A$  is the peak area,  $ASF$  stands for the atomic sensitive factor of element and Arabic number represents



elemental types.

### 3-4-2 Time-of-Flight Secondary Ion Mass Spectrometer (TOF-SIMS)

SIMS measurements were performed with a TOF-SIMS IV (ION-TOF, Munich, Germany) spectrometer. The TOF-SIMS spectra were recorded at 25 °C in positive detection modes. The primary ion source was a pulsed Ga<sup>+</sup> source (pulsing current 1.0 pA, pulse width 30 ns) operated at 25 keV. An area of 100×100 μm<sup>2</sup>, a sputter time of 120 s, a data acquisition time of 150 s and charge compensation by applying low energy electrons (~30 eV) from a pulsed flood gun were used for all measurements. The pressure of the main chamber was kept around 10<sup>-9</sup> mbar. The m/z of mass spectra in the positive mode was ranged from 40 to 60.

The surface atomic ratio was calculated from the intensity of secondary ions which are normalized to relative sensitivity factor. A relative sensitivity factor (RSF) is a conversion factor from secondary ion intensity to atom density. The RSF is defined by sub-equation<sup>62</sup>

$$\rho_i = \frac{I_i}{I_m} RSF \quad (3-2)$$

Where  $\rho_i$  is the impurity atom density in atoms/cm<sup>3</sup>,  $I_i$  is the impurity isotope (V, m/z=47.9) secondary ion intensity in counts/s,  $I_m$  is the matrix isotope (Ti, m/z= 50.8) secondary ion intensity in counts/s, and  $RSF$  has unit of atoms/cm<sup>3</sup>.

### 3-4-3 Scanning electronic microscopy (SEM)

Scanning electronic microscopy (SEM, Hitachi, S-4700, Type II) was used to observe the morphology of the doped TiO<sub>2</sub> under an accelerating voltage of 25 KV and a pressure of 3×10<sup>-6</sup> Pa. The samples for the SEM observation were prepared by suspending the powders in 15 mL acetone solution via ultrasonic vibration for 20 minutes. The suspension was then directly dropped on the glass and dried at 100°C. To prevent charge accumulation, the samples were pre-coated with a Au film by Ion coater (Eiko IB-2) for 3 minutes which thickness was 200 Å.

### 3-4-4 X-ray diffractometry

Powder X-ray diffraction patterns of the samples after calcination were recorded with a computer controlled X-ray powder diffractometer (XRPD, MAC Science, MXP18) using Cu K $\alpha$  radiation and operating at accelerating voltage of 30 kV and an emission current of 20 mA. The scanning 2 $\theta$  range is from 10° to 80° at a sampling width of 0.02° and scanning speed is 4 °/min. If a sample only contains anatase and rutile, the weight ratio of rutile phase ( $W_R$ ) can be calculated from the following equation:<sup>33</sup>

$$W_R = \frac{A_R}{0.884 A_A + A_R} \quad (3-3)$$

where  $A_A$  is intensity of anatase (101) peak and  $A_R$  is intensity of rutile (110) peak. The crystalline size ( $D$ ) of all samples was calculated from Scherrer's equation:<sup>63</sup>

$$D = \frac{K \times \lambda}{\beta \times \cos \theta} \quad (3-4)$$

Where  $d$  is the crystalline size,  $\lambda$  is the x-ray wavelength (Cu K $\alpha$  = 0.15406 nm),  $\beta$  is the width of the peak (full width at half maximum, FWHM) after correcting for instrumental peak broadening ( $\beta$  expressed in radians),  $\theta$  is the Bragg angle and  $K$  is the Scherrer constant. According to Bragg's law, the d-spacing could be calculated by this law, and geometric figure is shown in Figure 3-11.

$$d = \frac{n\lambda}{2 \sin \theta} \quad (3-5)$$

Where  $d$  is the d-spacing (nm),  $\lambda$  is the wavelength of incident X-ray,  $\theta$  is the Bragg angle and  $n=1$ .

To investigate the surface structures of the samples, the V<sub>2</sub>O<sub>5</sub>/TiO<sub>2</sub> films were coated onto glasses and dried at 100°C for few minutes. The coated film were analyzed by a grazing incident X-ray diffractometer (GI-XRD, Rigaku · RU-H3R), which use Cu K $\alpha$  radiation with incident angle of 1° and operate at accelerating voltage of 60 kV and an

emission current of 300 mA. The scanning  $2\theta$  range is from  $15^\circ$  to  $80^\circ$  at a sampling width of  $0.02^\circ$  and scanning speed is  $4^\circ/\text{min}$ .

### **3-4-5 UV/Vis diffuse reflectance spectroscopy (UV-Vis DRS)**

The UV-vis diffused reflectance spectra were recorded on a U-3010 Hitachi spectrometer with an integrating sphere reflectance accessory. The spectra were recorded from 900 to 200 nm at a scanning rate of 300 nm/min. Aluminum oxide, which was considered to exhibit total reflections, was used to be the reference. The spectra were transformed into absorptions according to Kubelka-Munk equation shown in equation 3-6.<sup>64</sup>

$$F(R) = \frac{(1 - R)^2}{2R} = \frac{k}{S} \quad (3-6)$$

Where  $k$  is absorption coefficient,  $S$  is scattering coefficient and  $R$  represents %R reflectance

### **3-4-6 Inductively Coupled Plasma Mass Spectrometry (ICP-MS)**

ICP-MS (Perkin Elmer, SCIEX ELAN 5000) was used to analyze bulk chemical compositions for V/Ti weight ratio of all samples. All solid of samples were digested with acid solution coupled with microwave.

### **3-4-7 Specific surface area**

The Brunauer, Emmett, and Teller (BET) surface area of catalysts were measured by  $N_2$  physisorption using a TriStar 3000 gas adsorption analyzer. The BET model was used to estimate the surface area of the samples according to the  $N_2$  adsorption data. For providing sufficient surface area for model calculation, over 0.2 g of powders was used for analysis. Because the calcination temperature of V-doped materials was  $300^\circ\text{C}$ , as-prepared sample was degassed at  $120^\circ\text{C}$  for 6 h.

### **3-4-8 Electron paramagnetic resonance (EPR)**

The photo-induced charge carriers were examined by an electron paramagnetic resonance spectrometer (EPR, Bruker EMX-10/12) working at X-band frequency. A 250 W Hg lamp (Moritex, MUV-250U-L) having a major output wavelength at 365 nm was

positioned at a fixed distance from a sample cavity. In addition, Figure 3-7 shows the distribution of the UV light system (Moritex, MUV-250U-L). The measurements were carried out at 77 K either in the dark or under irradiation. The instrumental conditions were set at a center field of 3400 G and a sweep width of 200.0 G. The microwave frequency was 9.50 GHz and the power was 8.0 mW.

The EPR spin trapping experiments using DMPO were performed at room temperature. The 0.03 M DMPO solution was prepared by adding 0.0345 mL DMPO into 10 mL DI water, and it was stored at 4°C. Each sample was aerated with 30 min O<sub>2</sub> before analysis. After addition of 1 mL of 0.03 M DMPO into 10 mL catalyst suspension (1g/l), the mixtures were shaken by hand to reach a homogeneous condition. Subsequently, the samples were delivered to a quartz capillary tube and analyzed the spin-trapped adducts under irradiation of UV light at room temperature. The settings for the EPR spectrometer were center field = 3480.0 G; sweep width = 200.0 G; microwave frequency 9.77 GHz; modulation frequency 50.0 kHz and power 10 mW. To minimize measurement errors, the same quartz capillary tube was used throughout the EPR measurements.

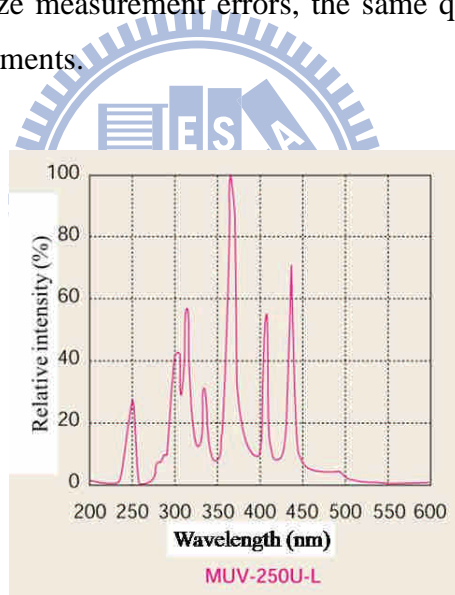


Figure 3-7 The UV lamp spectral distribution.<sup>65</sup>

### 3-4-9 Transmission Electron Microscope (TEM)

The particle size and shape of nanocrystals were examined by a transmission electronic microscopy (TEM, JEM 1200) at an accelerating voltage of 120 KV. The specimen was prepared by dispersing of powders into acetone with ultrasonic vibration. The colloid was dropped on a holey carbon film supported on a Cu grid (Ted Pella, Inc., 200 meshes). TEM images are displayed in Appendix I.

### 3-5 Photocatalytic of RhB decomposition

Rhodamine B (RhB) was selected as the target compound to test the photocatalytic activity of the doped TiO<sub>2</sub>. Figure 3-8 shows the UV-Vis spectrum of 0.01 mM RhB at 400-700 nm. The most intensive absorption peak appeared at 553 nm. The degradation of the RhB was monitored according to the decreasing intensity of this characteristic peak. The catalysts (20.0 mg) were dispersed ultrasonically into 20 mL of RhB solutions at concentration of 0.01 mM in a fused-silica tube. Prior to irradiation, the suspension was purged with O<sub>2</sub> in the dark with stirring for 30 minutes for equilibrium of adsorption and desorption of RhB and saturation of the solution with O<sub>2</sub>. The purging was continued during photocatalysis. The photocatalysis was carried out under irradiation of 8 UV lamps each of (8 W) at 365/305 nm. Figure 3-9 displays the cartoon diagram and photographs of the photocatalytic system.

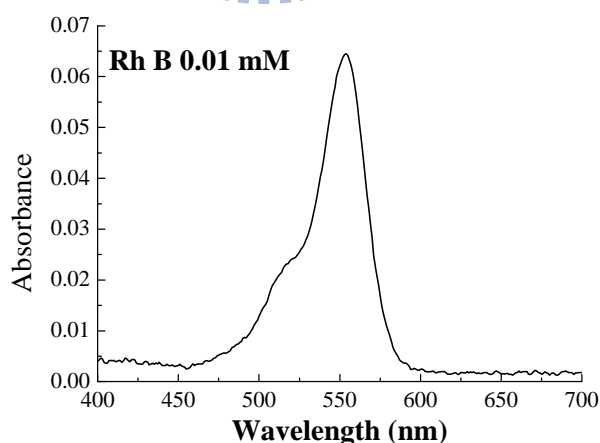


Figure 3- 8 The UV-Vis spectrum of 0.01 mM RhB.

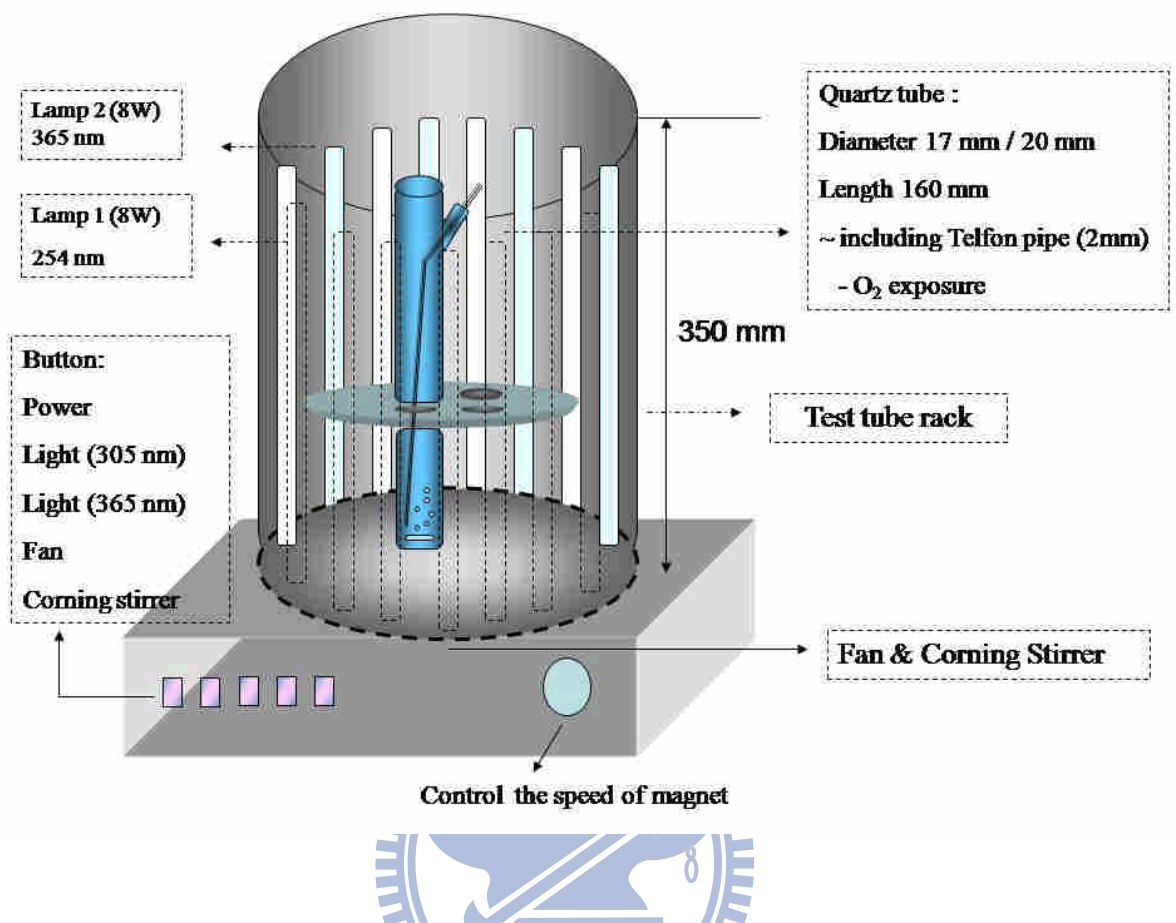


Figure 3-9 A design chart for photocatalysis reactor and A photograph of photocatalytic reactor.

## Chapter 4 Results and discussion

### 4-1 Chemical compositions

To understand the chemical compositions and chemical states of vanadium ions in the bulk lattice and surface sites of the doped TiO<sub>2</sub>, samples were characterized using ICP-MS, SIMS and XPS. Table 4-1 lists the bulk and surface V/Ti atomic ratios of bulk doped materials. Because the vanadium solutions were diluted by 2-isopropanol, the solution creates the errors between added V/Ti ratios and the measured bulk ratios. The bulk V/Ti ratios ranged between  $4.41 \times 10^{-5}$  and  $1.22 \times 10^{-2}$  which were similar to the added ratios (ranged between  $5.00 \times 10^{-5}$  and  $1.00 \times 10^{-2}$ ). However, the surface V/Ti ratios ranging  $3.03 \times 10^{-5}$ - $1.67 \times 10^{-2}$  were slightly larger than the bulk ratios. These results indicate that almost vanadium ions were successfully doped into TiO<sub>2</sub> in the sol-gel process. In addition, higher amounts of the doped vanadium ions were accumulated in the surface lattice.

Table 4-1 The bulk and surface V-to-Ti atomic ratios of bulk doped TiO<sub>2</sub>.

Added V/Ti ratios	Bulk V/Ti ratios <sup>a</sup>	Surface V/Ti ratios <sup>b</sup>	Sample name
$5.00 \times 10^{-5}$	$4.41 \times 10^{-5}$	$7.26 \times 10^{-5}$	VT $4.41 \times 10^{-5}$
$1.00 \times 10^{-4}$	$1.34 \times 10^{-4}$	$2.36 \times 10^{-4}$	VT $1.34 \times 10^{-4}$
$5.00 \times 10^{-4}$	$5.09 \times 10^{-4}$	$6.72 \times 10^{-4}$	VT $5.09 \times 10^{-4}$
$1.00 \times 10^{-3}$	$1.27 \times 10^{-3}$	$1.84 \times 10^{-3}$	VT $1.27 \times 10^{-3}$
$1.00 \times 10^{-2}$	$1.22 \times 10^{-2}$	$1.67 \times 10^{-2}$	VT $1.22 \times 10^{-2}$

<sup>a</sup> determined by ICP-MS, <sup>b</sup> determined by SIMS.

Table 4-2 lists the bulk and surface V/Ti atomic ratios for the surface doped materials with increasing contents of vanadium ions. The surface doped TiO<sub>2</sub> contained bulk and surface V/Ti ratios of  $1.73 \times 10^{-3}$  -  $1.10 \times 10^{-2}$  and  $1.54 \times 10^{-2}$  -  $2.97 \times 10^{-1}$ , respectively. Since the surface doped samples were prepared by coating a thin V/TiO<sub>2</sub> film on the TiO<sub>2</sub> particles, the bulk V/Ti ratios were much smaller than the surface ones. Similar to the bulk doped TiO<sub>2</sub>, the surface V/Ti ratios were 1.5 - 2.7 times larger than the added V/Ti ratios of the surface coating ( $1.00 \times 10^{-2}$  -  $2.00 \times 10^{-1}$ ), indicating the migration of the vanadium ions from the bulk toward the surface. Davidoson and Che<sup>58</sup> reported that metal ions migrated to the surface of substance above the Tammann temperature at which the thermal vibrations of cations were strong enough for lattice diffusion. The Tammann temperature is 0.37-0.53 T<sub>f</sub>,

where  $T_f$  represents the melting temperature of oxides. The  $T_f$  of  $TiO_2$  is 2190 K, thus its Tammann temperature is 780-1118 K.<sup>16, 58</sup> However, the enhanced mobility of  $V^{5+}$  is associated with its lower Tammann temperature of  $V_2O_5$  (i.e. 209 °C) compare to  $TiO_2$ .<sup>66</sup> So, some vanadium ions migrated from bulk lattice toward to surface lattice of  $TiO_2$ .

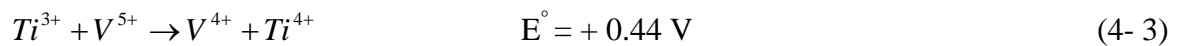
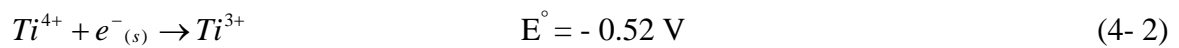
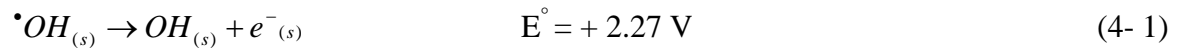
Herein, the bulk chemical compositions determined by ICP-MS were used to name all the doped samples. For example, the bulk doped  $TiO_2$  with total V/Ti ratio of  $4.41 \times 10^{-5}$  was called VT  $4.41 \times 10^{-5}$ . For surface doped  $TiO_2$ , the sample with total V/Ti of  $1.10 \times 10^{-2}$  was named as SVT  $1.10 \times 10^{-2}$ . In addition, the sample which was coated pure  $V_2O_5$  on  $TiO_2$  was named SVTP. Its total bulk V/Ti ratio was  $4.74 \times 10^{-3}$ , as shown in Appendix F.

Table 4-2 The bulk and surface V-to-Ti atomic ratios of surface doped  $TiO_2$ .

Added V/Ti ratios of the coating layer	Bulk V/Ti ratios <sup>a</sup>	Surface V/Ti ratios <sup>b</sup>	Sample name
$2.00 \times 10^{-1}$	$1.10 \times 10^{-2}$	$2.97 \times 10^{-1}$	SVT $1.10 \times 10^{-2}$
$1.00 \times 10^{-1}$	$6.40 \times 10^{-3}$	$2.03 \times 10^{-1}$	SVT $6.40 \times 10^{-3}$
$5.00 \times 10^{-2}$	$3.47 \times 10^{-3}$	$1.37 \times 10^{-1}$	SVT $3.47 \times 10^{-3}$
$1.00 \times 10^{-2}$	$1.73 \times 10^{-3}$	$1.54 \times 10^{-2}$	SVT $1.73 \times 10^{-3}$

<sup>a</sup> determined by ICP-MS, <sup>b</sup> determined by SIMS.

The chemical states of the vanadium ions in the bulk and the surface lattices were determined using ESCA (see Appendix D). The vanadium ions at the surface sites were mainly  $V^{5+}$  form, while  $V^{4+}$  were observed in the bulk lattices. The reduction of  $V^{5+}$  to  $V^{4+}$  was attributed to thermal-induced dehydroxylation which preliminarily led to the formation of  $Ti^{3+}$  sites followed by the consecutive electron transfer from the  $Ti^{3+}$  to  $V^{5+}$  sites.<sup>67-69</sup> These processes can be expressed schematically by the following set of reactions.





## 4-2 Morphology

Figure 4-1 shows the SEM images of as-dried and calcined TiO<sub>2</sub>. The surface of the as-dried TiO<sub>2</sub> was smooth. However, the particles were composed of small grains with sizes smaller than 100 nm after calcination at 300 °C. In general, the particles are agglomerated and basically irregular in shape with a substantial variation in particle sizes. The results indicate that degree of agglomeration tended to increase with increasing calcination temperature.<sup>70</sup> Thus, polycrystalline structure and agglomerated phenomena occurred during calcination at temperature of 300 °C. Figure 4-2 shows the SEM image of the bulk doped TiO<sub>2</sub> calcined at 300 °C. Similar to the pure TiO<sub>2</sub>, the bulk doped TiO<sub>2</sub> was also consisted by small grains which was smaller than 100 nm. Figure 4-3 shows the SEM images of surface doped TiO<sub>2</sub> particles and the cross sectional view of its V-doped TiO<sub>2</sub> coating. The surface coating film contained a thickness of around 50 nm. Different from the bulk doped TiO<sub>2</sub>, the surface doped TiO<sub>2</sub> was smooth due to rapid hydrolysis while surface sol-gel processes did not add HCl. In addition, the SVTP  $4.74 \times 10^{-3}$  coated a thin film of V<sub>2</sub>O<sub>5</sub> on TiO<sub>2</sub> also exhibited smooth morphology (see Appendix F). These findings suggest that the thin film prepared by surface sol-gel was uniform which resulted from lack of HCl.

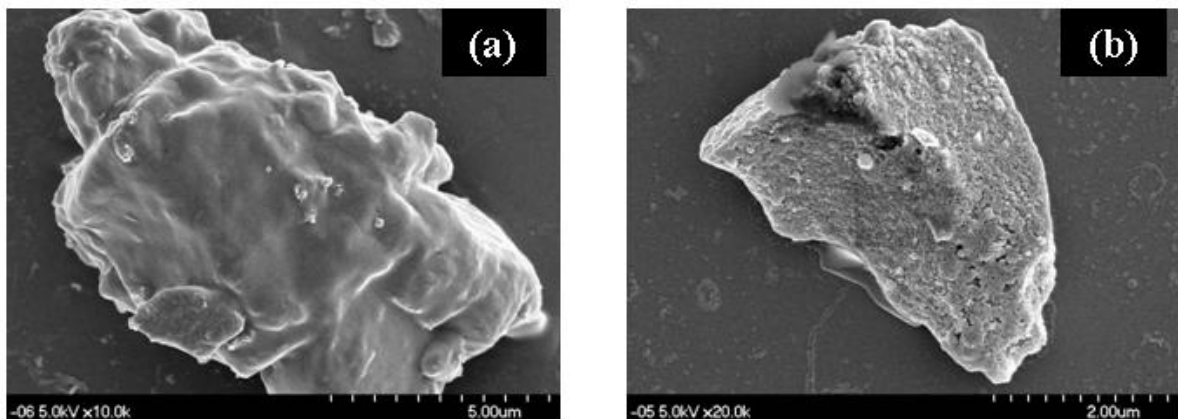


Figure 4-1 The morphology of pure TiO<sub>2</sub> calcined at (a) 150 °C for 3 h and (b) 150 and 300 °C for 3 h.

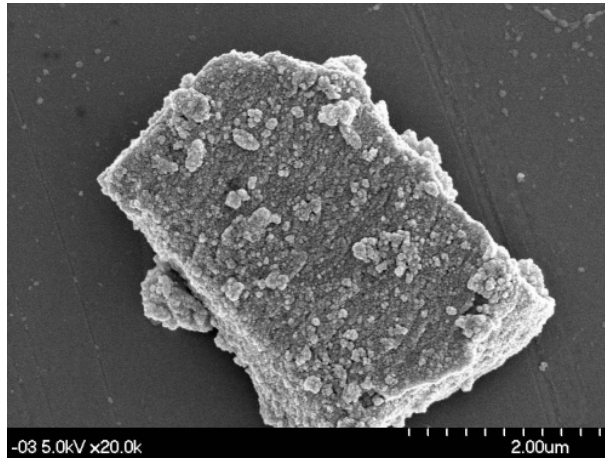


Figure 4-2 The SEM images of bulk doped materials

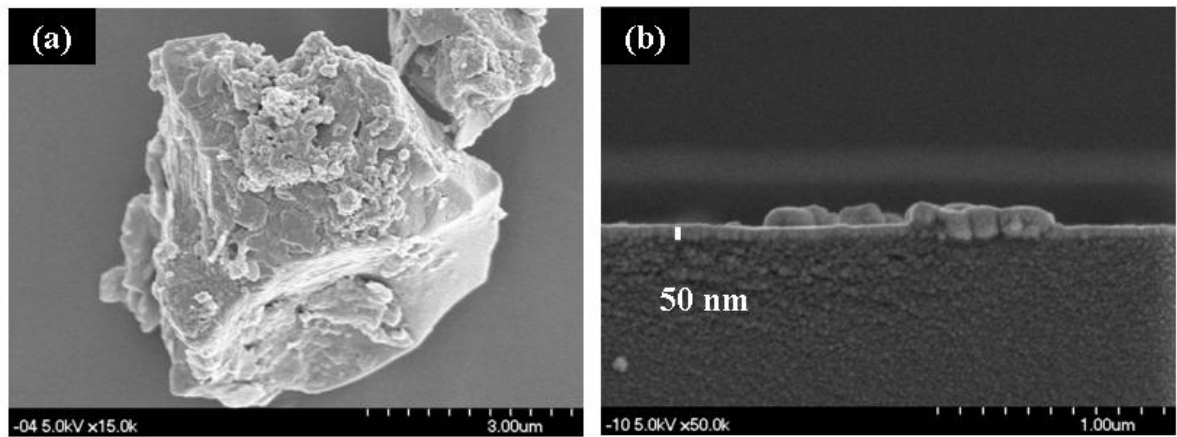


Figure 4-3 The SEM images of (a) surface doped materials and (b) cross sectional view of a V-doped TiO<sub>2</sub> film prepared by the surface sol-gel method.

### 4-3 Microstructures

To examine the effect of doping sites on the crystalline structure, grain size, d-spacing and specific surface area, all samples were analyzed by XRD and BET. Figure 4-4 displays the crystalline structures of pure and bulk doped TiO<sub>2</sub>. The peaks of the anatase (101) and rutile (110) profiles centered at 25.4 and 27.5° 2θ positions, respectively. It indicated the coexistence of anatase and rutile phases in the pure TiO<sub>2</sub> and the weight ratio of rutile was 31.1wt% which error bar is 5 wt%. The weight ratio of rutile (i.e. 21.3-26.5 wt%) of bulk doped materials slightly decreased while V/Ti atomic ratio was lower than 1.27×10<sup>-3</sup>. Besides, the rutile phase was not detected while the V/Ti atomic ratio was higher than 1.27×10<sup>-3</sup>, indicating that the presence of V<sup>4+</sup>/V<sup>5+</sup> inhibits the anatase-to-rutile transformation. The anatase-rutile transformation was restrained by formation of V<sub>2</sub>O<sub>5</sub> phase occurred at high vanadium ions and low calcination temperature.<sup>71</sup> No diffraction peaks corresponding to vanadium oxide were observed in the XRD pattern. Therefore, the vanadium ions were either highly dispersed in the TiO<sub>2</sub> matrix or formed as tiny vanadia crystallites having the size beyond the detection capacity of the powder X-ray diffraction technique (less than 5 nm). Table 4-3 lists the d-spacing, crystallite sizes and weight ratios of rutile phases of the bulk doped TiO<sub>2</sub>. The d-spacing of (101)<sub>a</sub> of the bulk doped TiO<sub>2</sub> were 351 pm. This value was similar to that of pure TiO<sub>2</sub> (350 pm) and the d-spacing was slightly increased from 530 to 353 pm even under heavily doping (See Appendix E). Since the ionic radius of V<sup>4+</sup>/V<sup>5+</sup> is 72/68 pm which is closed to that of Ti<sup>4+</sup> (74.5 pm),<sup>72</sup> the vanadium ions are doped into the TiO<sub>2</sub> lattice by substituting Ti<sup>4+</sup> ions.

The average crystallite sizes of pure TiO<sub>2</sub>, estimated from the broadening of the anatase (101) diffraction peak, are 6.1 nm which error bar is 0.6 nm. Compare with pure TiO<sub>2</sub>, the crystallite sizes (i.e. 6.0-6.5 nm) of bulk doped materials had no obviously difference. The results show the concentration of vanadium-ion (V/Ti < 1.00×10<sup>-2</sup>) is too low to affect the crystallite size. However, when V/Ti atomic ratio increased to 2.00×10<sup>-1</sup>, the crystallite size of anatase decreased from 6.1 to 5.2 nm, as shown in Appendix E. The inhibition of the growth of crystallite sizes was resulted from increasing surface energy and surface stress caused by lattice vanadium ions.<sup>58, 67</sup> Figure 4-5 schematically illustrates the inhibited growth of crystallite sizes of bulk doped TiO<sub>2</sub>.

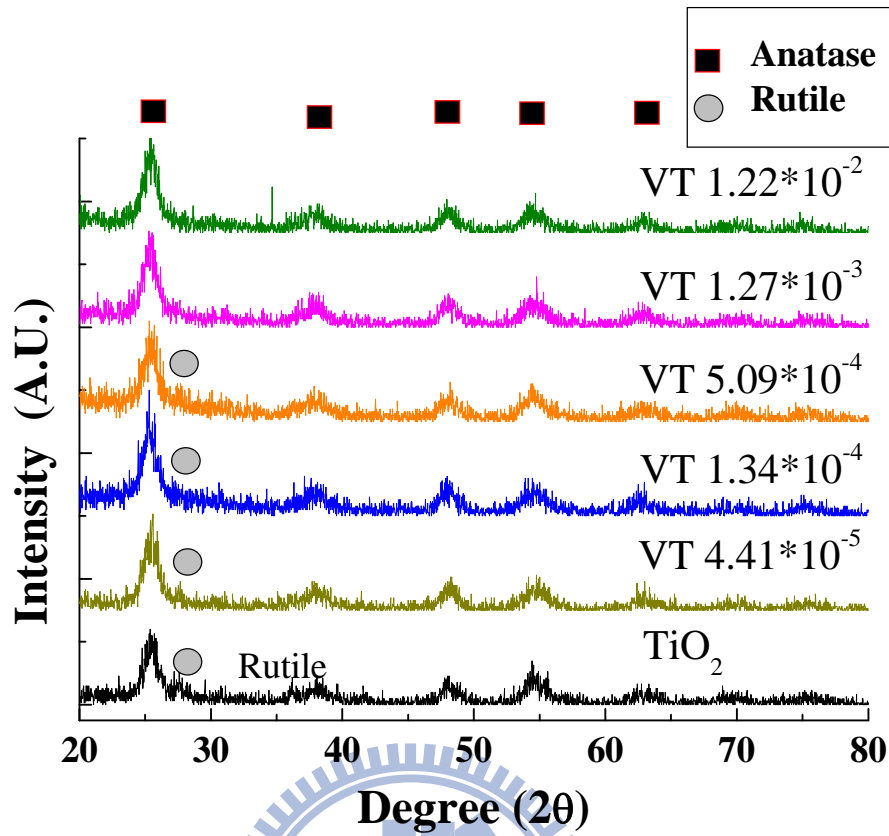


Figure 4-4 The XRD patterns of bulk doped  $\text{TiO}_2$  at different vanadium ion concentrations.

Table 4-3 The crystallite sizes, d-spacing of materials and weight ratio of rutile phase of bulk doped  $\text{TiO}_2$ .

Bulk doped $\text{TiO}_2$			
Materials	Crystallite size (nm)	d-spacing (pm) (n = 1)	Weight ratio of Rutile (wt %)
$\text{TiO}_2$	$6.1 \pm 0.6$	$350 \pm 0$	$31.1 \pm 5.0$
$\text{VT } 4.41 \times 10^{-5}$	6.0	351	21.3
$\text{VT } 1.34 \times 10^{-4}$	6.4	351	24.0
$\text{VT } 5.09 \times 10^{-4}$	6.3	351	26.5
$\text{VT } 1.27 \times 10^{-3}$	6.5	351	—
$\text{VT } 1.22 \times 10^{-2}$	6.2	351	—

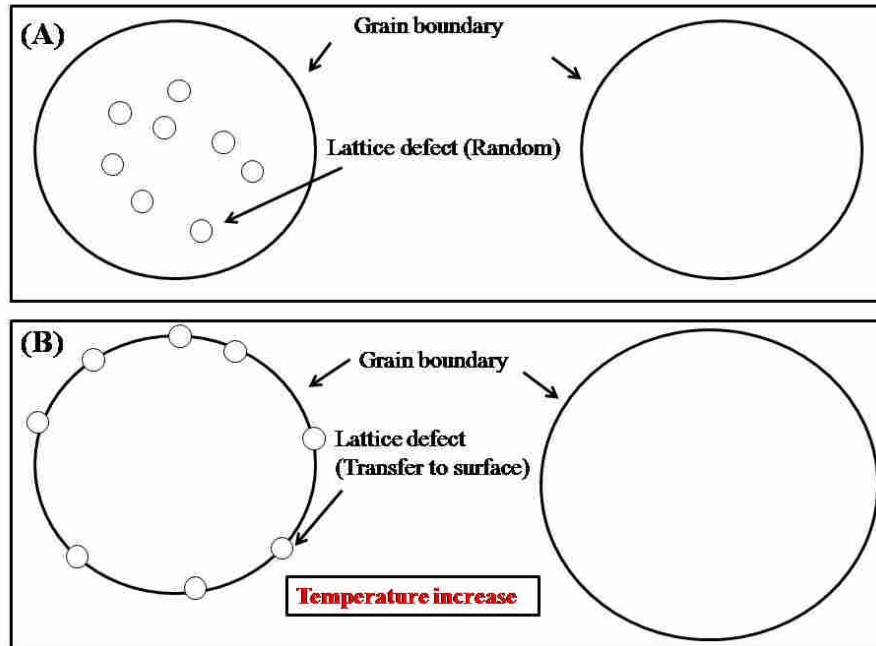


Figure 4-5 The effect of bulk defect on growth of crystal.

To analyze the surface microstructure of the V-doped  $\text{TiO}_2$ , GI-XRD was used to examine the surface crystalline properties of the samples. Figure 4-6 shows the GI-XRD patterns of bulk doped  $\text{TiO}_2$ . The two peaks centered at  $25.4^\circ$  and  $19.2^\circ$   $2\theta$  positions were denoted to anatase and  $\text{V}_2\text{O}_5$ , respectively. In addition, the relative intensity of  $\text{V}_2\text{O}_5$  increased with increasing vanadium ions. The data indicate parts of vanadium ions transferred toward surface of matrix and agglomerated to perform  $\text{V}_2\text{O}_5$  at  $300^\circ\text{C}$ , while the chemical state of vanadium ions was  $\text{V}^{5+}$ .

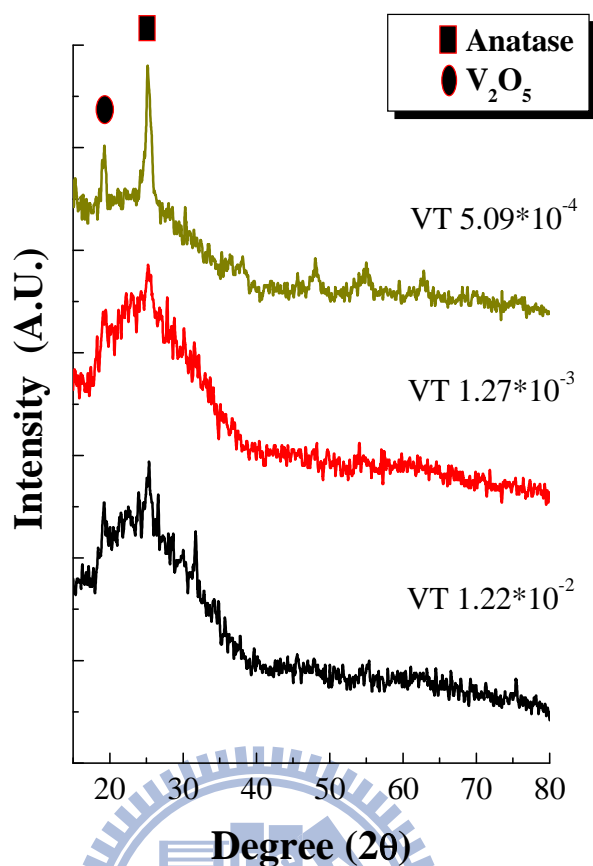


Figure 4-6 The GI-XRD patterns of bulk doping materials.

Figure 4-7 shows the XRD patterns of surface doped  $\text{TiO}_2$ . Table 4-4 lists the d-spacing, crystal sizes and weight ratios of rutile phases of the surface doped  $\text{TiO}_2$ . The crystallite sizes of anatase  $\text{TiO}_2$  were in the range of 6.0-6.5 nm, while their d-spacing of anatase (101) profile were in the range of 350-352 pm. In addition, the weight ratio of rutile were not detected except SVT  $1.73 \times 10^{-3}$  since these characters were similar to those of pure  $\text{TiO}_2$ , surface doped  $\text{V}^{5+}$  ions had little effects on the bulk microstructures of  $\text{TiO}_2$ . Figure 4-8 displays the  $\text{V}_2\text{O}_5/\text{TiO}_2$  thin films coated on glass which were prepared by surface sol-gel. In contrast to bulk doped  $\text{TiO}_2$ ,  $\text{V}_2\text{O}_5$  crystallites were observed only on the surface of substances. This phenomenon revealed that the  $\text{TiO}_2$  was coated with  $\text{V}_2\text{O}_5$  as a core-shell structure in the surface doped  $\text{TiO}_2$  samples. Therefore, the chemical status of vanadium in bulk doped  $\text{TiO}_2$  co-existed both  $\text{V}^{4+}$  and  $\text{V}^{5+}$ . The chemical status is an important evidence to deduce whether vanadium was located in the  $\text{TiO}_2$  octahedral lattice. The  $\text{V}^{4+}$  was possible in the octahedral lattice of  $\text{TiO}_2$ , while  $\text{V}^{5+}$  may be  $\text{V}_2\text{O}_5$  highly dispersed within crystalline of  $\text{TiO}_2$ . In addition, both the intensity and crystal sizes of  $\text{V}_2\text{O}_5$  (i.e. 11.2 nm) did not alter with increasing vanadium ions.

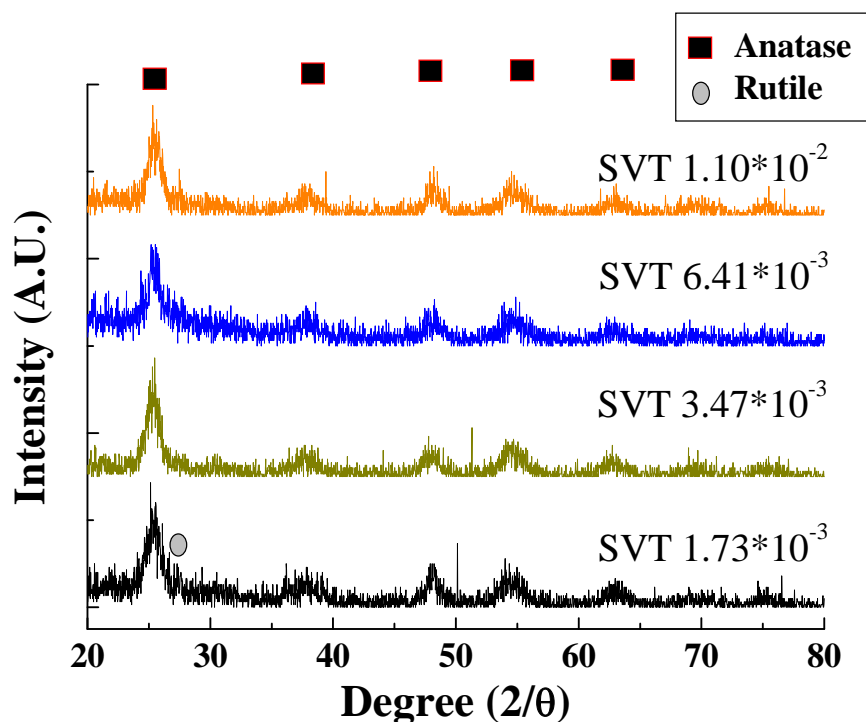


Figure 4-7 The XRD patterns of surface doped materials at different vanadium ions concentration.

Table 4-4 The crystallite sizes of materials and weight ratio of rutile phase of surface doped  $\text{TiO}_2$

Surface doped materials			
Materials	Crystal size (nm)	d-spacing (pm) (n = 1)	Weight ratio of Rutile (%)
$\text{SVT } 1.73 \times 10^{-3}$	6.0	351	25.5
$\text{SVT } 3.47 \times 10^{-3}$	6.5	352	—
$\text{SVT } 6.40 \times 10^{-3}$	6.2	350	—
$\text{SVT } 1.10 \times 10^{-2}$	6.2	350	—

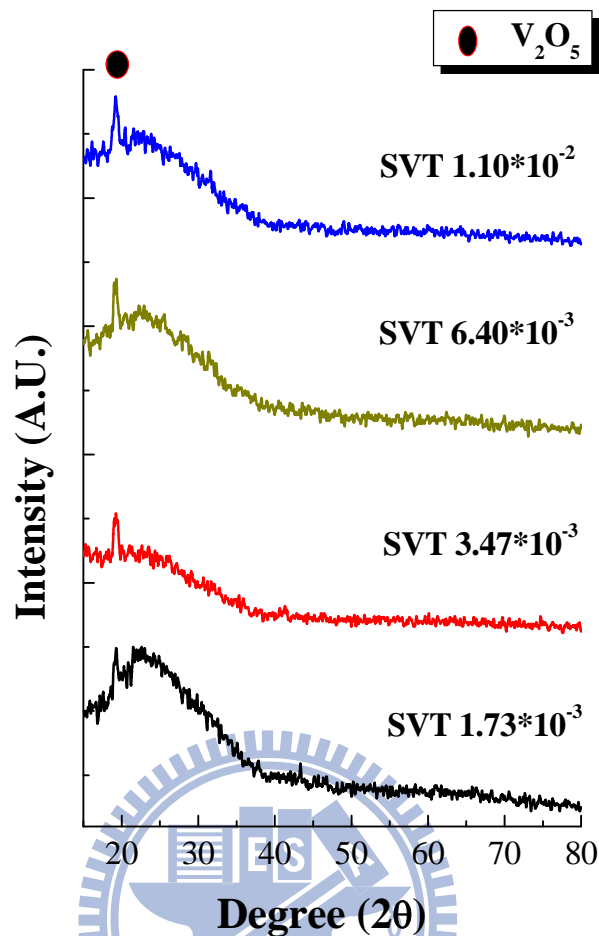


Figure 4-8 The GI-XRD patterns of surface doped materials.

Figure 4-9 illustrates the microstructures of bulk and surface doped  $TiO_2$ . In the bulk doped  $TiO_2$ , vanadium ions were substitutionally doped in the anatase lattice while few  $V_2O_5$  crystals were existed in the surface layers. However,  $TiO_2/V_2O_5$  core-shell structures were formed in the surface doped  $TiO_2$ . The specific surface area of bulk and surface doped  $TiO_2$  were listed in Appendix C. The specific surface areas of bulk doped materials were ranged between 99 and 110  $m^2/g$ , while the surface doped materials exhibited their specific surface areas of 99-105  $m^2/g$ . Either doping  $TiO_2$  with  $V^{4+}/V^{5+}$  ions in the bulk lattice or on the surface sites had little effects on the specific surface areas because the as-dried oxides are usually amorphous, they must be calcined at high temperature for crystallization. Unfortunately, the decreasing crystallite size increased the surface area of the photocatalysts.

70, 73



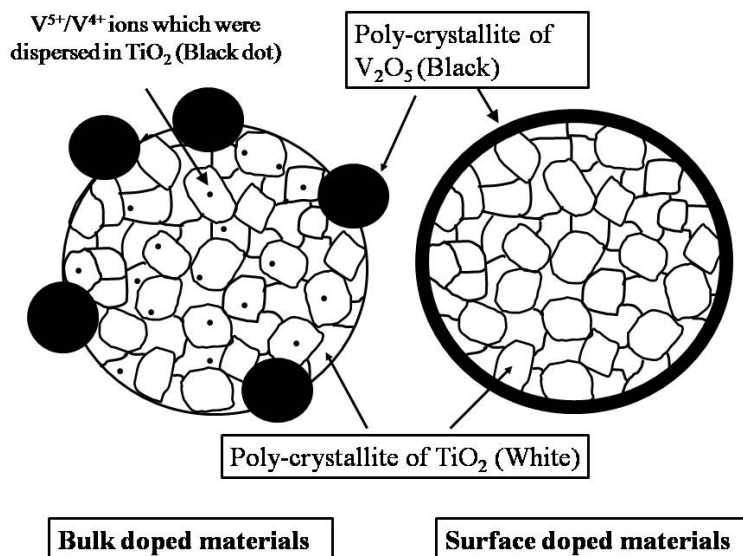


Figure 4-9 The microstructures of bulk and surface doped TiO<sub>2</sub>.

#### 4-4 UV-Visible absorption

In order to elucidate the optical properties for photocatalysts, UV-vis diffuse reflectance spectroscopy (DRS) was applied to study the bonding information of the V-doped TiO<sub>2</sub>. Figure 4-10 shows the optical absorbance of pure TiO<sub>2</sub> from wavelength of 900 to 200 nm. The absorption edge was at 405 nm, corresponding to 3.1 eV of the bandgap energy. Below 405 nm, there were two bands separated at 263 nm. One broad band was ranged between 200-300 nm and centered at 233 nm which was denoted to upper CB.<sup>74, 75</sup> The upper band centered at 233 nm was assigned to a charge-transfer transition between the oxygen ligands and a central Ti<sup>4+</sup> ion with a tetrahedral coordination (4-fold).<sup>74, 75</sup> The other band centered at 353 nm which was denoted to lower CB.

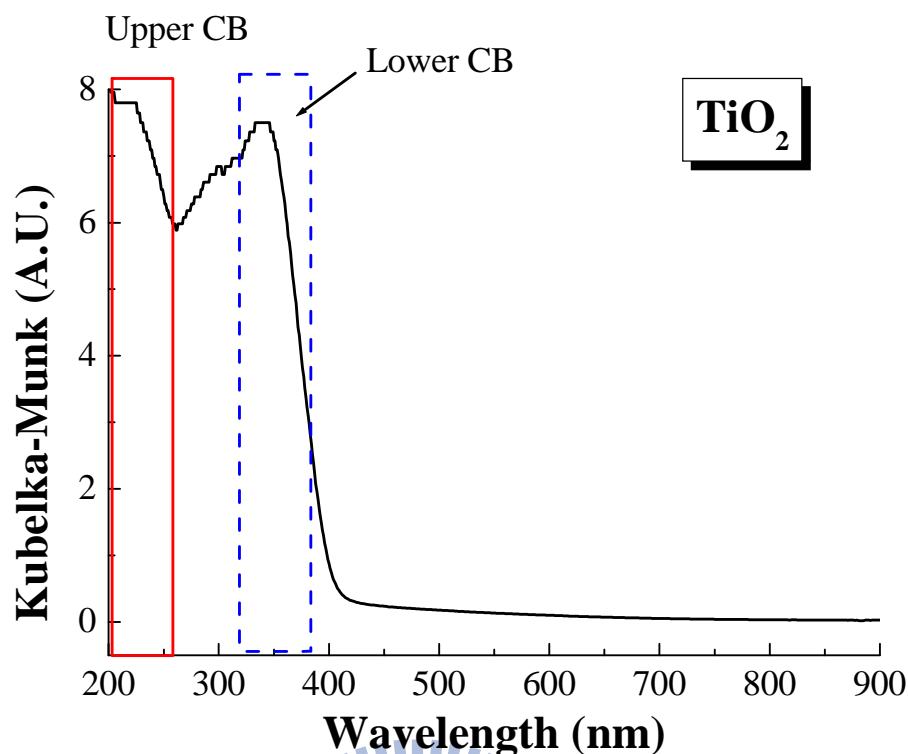


Figure 4-10 UV-Vis DRS spectra of TiO<sub>2</sub>. The red solid line: Upper conduction band. The blue dash line: Lower conduction band.

Figure 4-11 shows the optical absorbance of bulk doped TiO<sub>2</sub> with various contents of vanadium-ion doping. The spectra of bulk doped materials showed similar absorption behavior at an absorption edge of around 405 nm (3.1 eV), except VT  $1.22 \times 10^{-2}$  which exhibited the absorption edge of 426 nm (2.9 eV). Table 4-5 lists the band gaps of the bulk doped TiO<sub>2</sub> containing varies V/Ti ratios. The bulk doped TiO<sub>2</sub> with vanadium ions, which was lower  $1 \times 10^{-2}$ , showed a broad adsorption peak ranged 250-320 nm and centered at 289 nm, which was denoted to V<sup>5+</sup>.<sup>76</sup> The V<sup>5+</sup> broad band was occurred between upper and lower CB. So, the V<sup>5+</sup> (3d) bands lied in the CB edge of TiO<sub>2</sub>, and the intensity of V<sup>5+</sup> peak increased with raising vanadium ions. However, when V/Ti was larger than 1 mol %, the d-d transition of V<sup>4+</sup> occurred. The results show a broad adsorption from 779 nm in the inside graph of Figure 4-11. So, the V<sup>5+</sup> ions reduced to V<sup>4+</sup> under higher vanadium concentration.

Because a spontaneous reduction of V<sup>5+</sup> to V<sup>4+</sup> occurred at the vanadium oxide and titanium oxide interface during calcination at temperatures above 450 °C,<sup>68, 77</sup> the chemical states of vanadium ions of bulk doped materials was V<sup>5+</sup> mainly under lower vanadium concentration (V/Ti < 1 mol %) and lower calcination temperature (300 °C < 450 °C). In

addition, the  $V^{4+}$  reduced by  $V^{5+}$  performed extra band located above VB 1 eV when V/Ti was larger than 1 mol %, as shown in Figure 4-12.<sup>29, 78</sup> In this study, Figure 4-13 shows the different electronic structure with high and low vanadium contents.

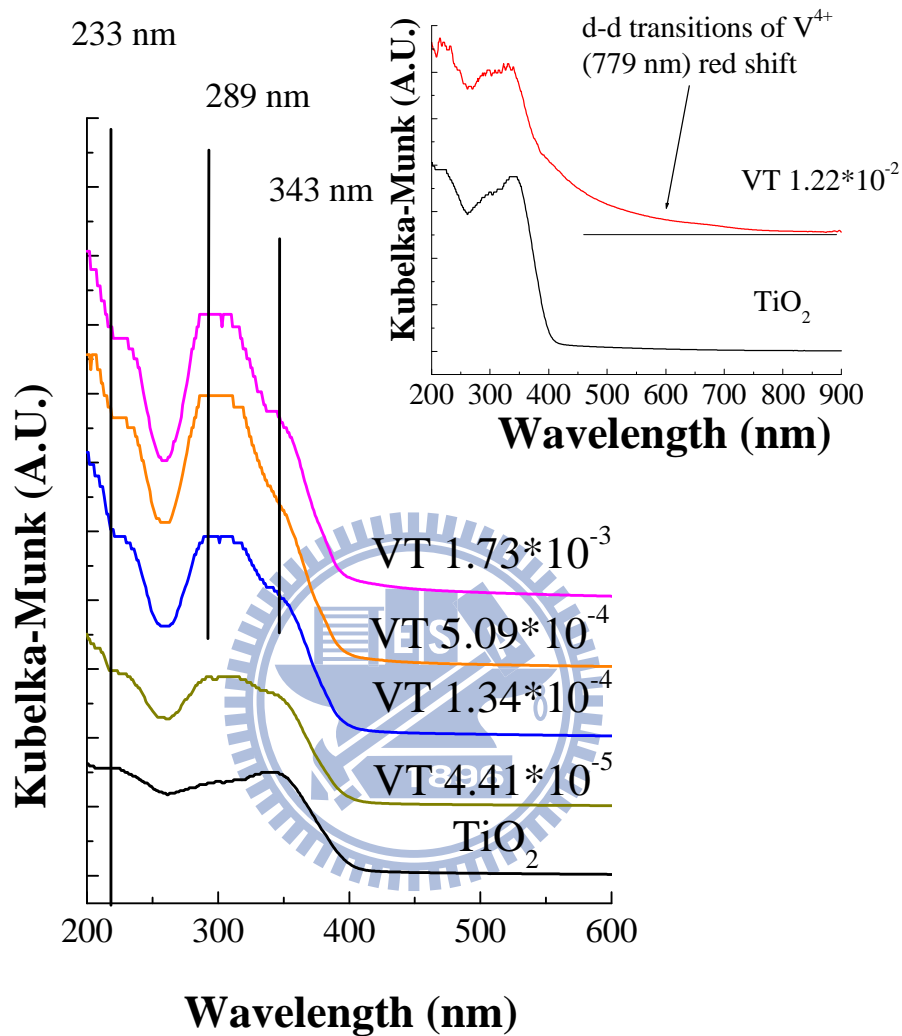


Figure 4-11 The UV-visible absorption spectra of all bulk doped materials at different vanadium ions concentration, except  $VT 1.22 \times 10^{-2}$  which is shown in inside graph.

Table 4-5 The band gap energy of bulk doped TiO<sub>2</sub>.

Bulk doped TiO <sub>2</sub>	
Materials	Band gap (eV)
TiO <sub>2</sub>	3.1
VT $4.41 \times 10^{-5}$	3.1
VT $1.34 \times 10^{-4}$	3.1
VT $5.09 \times 10^{-4}$	3.1
VT $1.27 \times 10^{-3}$	3.1
VT $1.22 \times 10^{-2}$	2.9

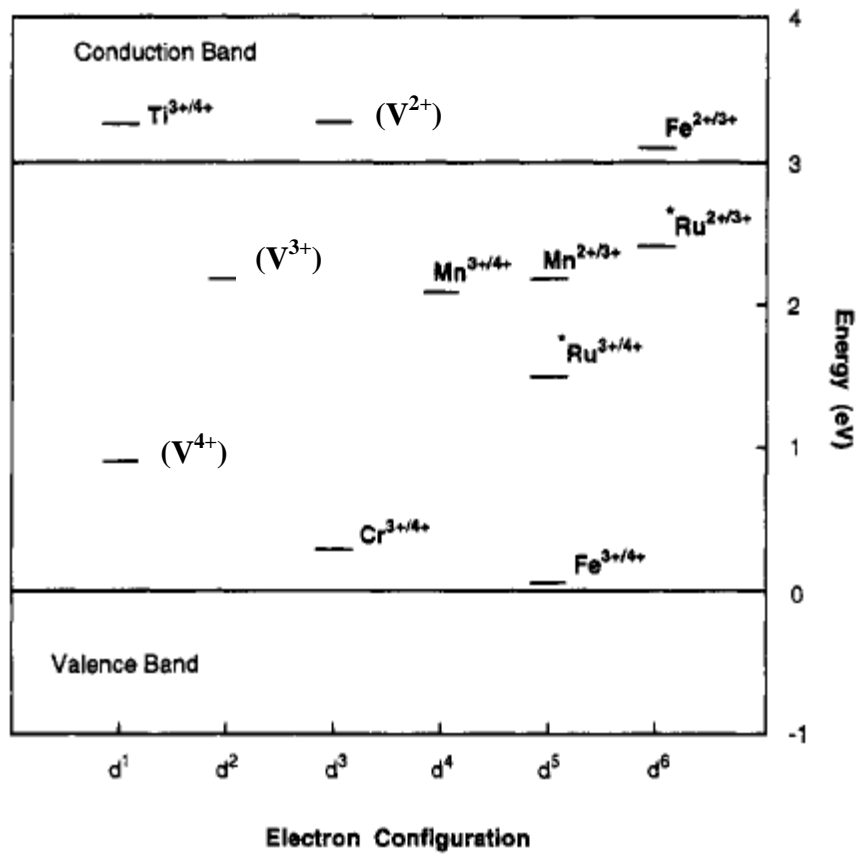


Figure 4-12 Energy levels of impurity ions in rutile.<sup>29</sup>

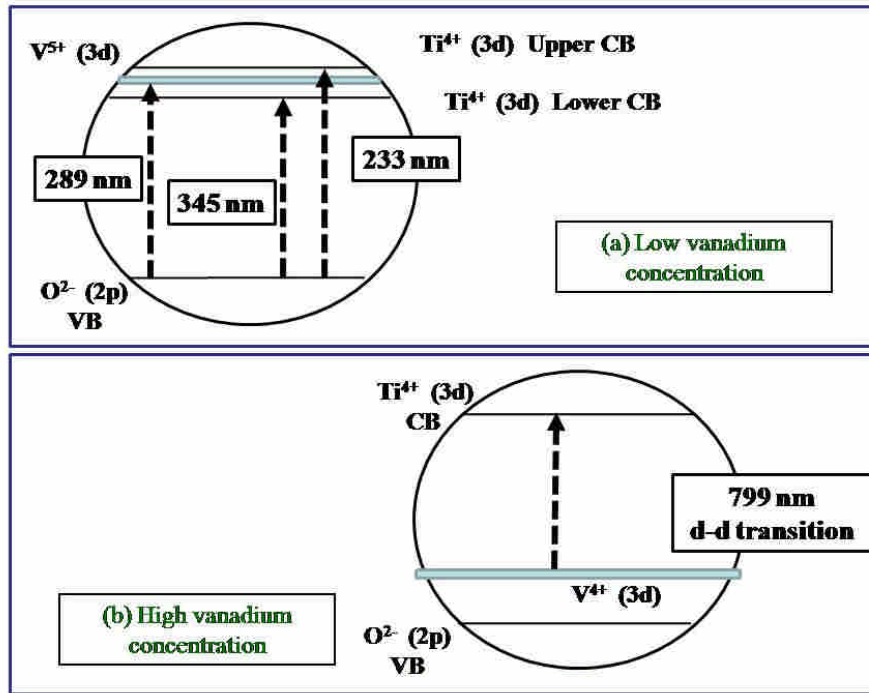


Figure 4-13 The concept of electronic structure for bulk doping materials. (a) low vanadium ions (< 1 mole%); (b) high vanadium ions (i.e. VT  $1.22 \times 10^{-2}$ ).

Figure 4-14 displays the optical absorbance of surface doped  $TiO_2$  from wavelength of 900 to 200 nm. The similar absorption behaviors of surface doped materials at an absorption edge of around 405 nm (3.1 eV) are shown in Figure 4-14. Table 4-6 lists the band gap of surface doped  $TiO_2$  at various vanadium ions concentration. The band gap surface doped  $TiO_2$  was around 3.1 eV.

The results show that vanadium ions doped on the surface of  $TiO_2$  had no obvious effect on the electronic structure of  $TiO_2$ . Clearly, the findings indicate that the bulk doping sites had more obvious effect than surface doping site on electronic structure of  $TiO_2$ . Besides, Figure 4-15 illustrates the scheme of electronic structure of  $TiO_2/V_2O_5$  composite semiconductors. It refers that the CB of  $V_2O_5$  was lower than  $TiO_2$ , because d-orbital energy of the highest occupied atomic d-orbital of vanadium was lower than that of titanium.<sup>79, 80</sup> Therefore, to summarize the salient features of the analysis, the image electronic structure of bulk and surface doped  $TiO_2$  were illustrated in Figure 4-13 and Figure 4-16 respectively.

Table 4-6 The band gap energy of surface doped TiO<sub>2</sub>

Surface doped TiO <sub>2</sub>	
Materials	Band gap (eV)
SVT 1.73×10 <sup>-3</sup>	3.1
SVT 3.47×10 <sup>-3</sup>	3.1
SVT 6.40×10 <sup>-3</sup>	3.1
SVT 1.10×10 <sup>-2</sup>	3.1
SVTP 4.74×10 <sup>-3</sup>	3.1

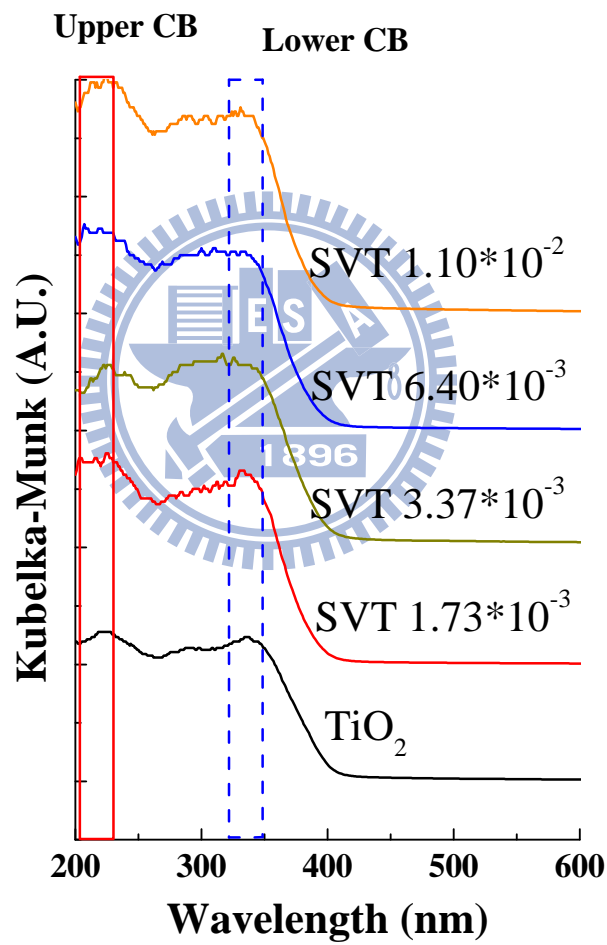


Figure 4-14 The UV-visible absorption spectra of the surface doped materials at different vanadium ions concentrations.

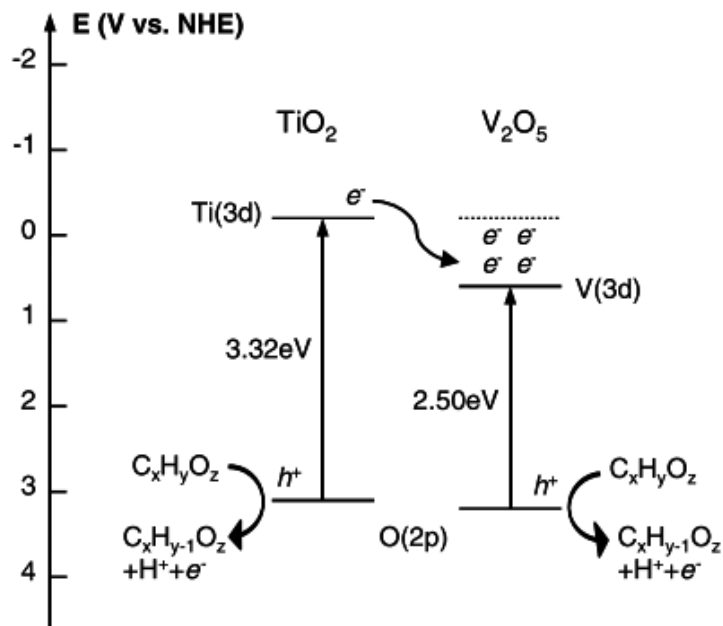


Figure 4-15 Schematic band energy diagram for the TiO<sub>2</sub>/V<sub>2</sub>O<sub>5</sub> composite semiconductor.<sup>80</sup>

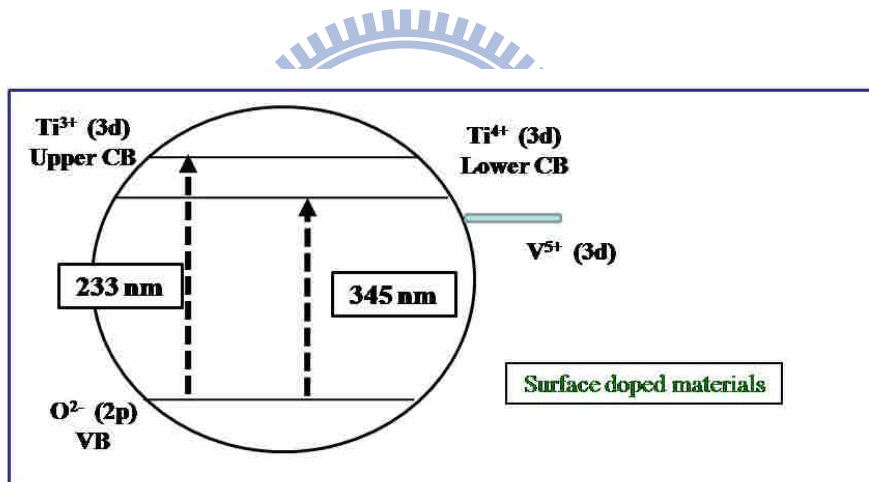


Figure 4-16 The electronic structure of surface doping materials.

## 4-5 Photocatalytic activity

The photocatalytic activities of vanadium ions doped TiO<sub>2</sub> was examined by the decoloration of 0.01 mM RhB monitored at 553 nm. Figure 4-17 displays the photocatalytic activities of bulk doped TiO<sub>2</sub> irradiated with UV light at 365 and 305 nm, respectively. In the absence of a photocatalyst, RhB was stable when irradiated with UV light at 365 and 305 nm. The photodecomposition of RhB followed pseudo-first-order kinetics with 305 nm irradiation. The degradation of RhB in the presence of the prepared nanocrystals indicated each of the bulk doped photocatalysts exhibited lower photoactivity. Since all bulk doped TiO<sub>2</sub> exhibit anatase form and similar band gaps (3.1-2.9 eV); it is suggested that the extra energy band caused by vanadium ions had negative influence on the photoactivities, because V<sup>4+</sup> reduced by V<sup>5+</sup> acted as recombination center, as shown in Figure 4-18. Moreover, the decreased photocatalytic activities were caused by increasing vanadium-ion doping. In addition, the tendency of photodecomposition of RhB with 365 nm irradiation was similar to 305 nm irradiation. Figure 4-18 displays the dependence of photocatalytic rate constants of bulk doped TiO<sub>2</sub> on the V/Ti ratios under irradiation of UV light at 365 and 305 nm. According to Langmuir-Hinshelwood (LH) kinetics, the photodecomposition of RhB was followed zero-order kinetics under 365 nm UV irradiation and that was followed pseudo-order kinetics with 305 nm irradiation. The difference was presumably due to fewer amounts of charge carriers were generated under irradiation of the UV light with higher wavelength. Thus, the effective concentration of RhB was augmented and zero-order kinetics was followed under this situation.

Table 4-7 lists the degradation rate constant (min<sup>-1</sup>) of bulk doped samples with UV light at 365 and 305 nm. The VT 4.41×10<sup>-5</sup> (k = 5.60×10<sup>-2</sup> min<sup>-1</sup>) exhibited the highest rate of decomposition of RhB with UV at 305 nm, followed by, TiO<sub>2</sub> (k = 5.20×10<sup>-2</sup> min<sup>-1</sup>), VT 1.34×10<sup>-4</sup> (k = 5.10×10<sup>-2</sup> min<sup>-1</sup>), VT 5.09×10<sup>-4</sup> (k = 4.00×10<sup>-2</sup> min<sup>-1</sup>), VT 1.27×10<sup>-3</sup> (k = 3.30×10<sup>-2</sup> min<sup>-1</sup>) and VT 1.22×10<sup>-2</sup> (k = 1.50×10<sup>-2</sup> min<sup>-1</sup>). Under 365 UV irradiation, the samples with bulk doped ratios lower than 5.09×10<sup>-4</sup> exhibited similar rate constants (k = 1.33×10<sup>-2</sup> mM/min) for decomposition of RhB followed by VT 1.27×10<sup>-3</sup> (k = 1.00×10<sup>-2</sup> mM/min) and VT 1.22×10<sup>-2</sup> (k = 6.00×10<sup>-3</sup> mM/min).



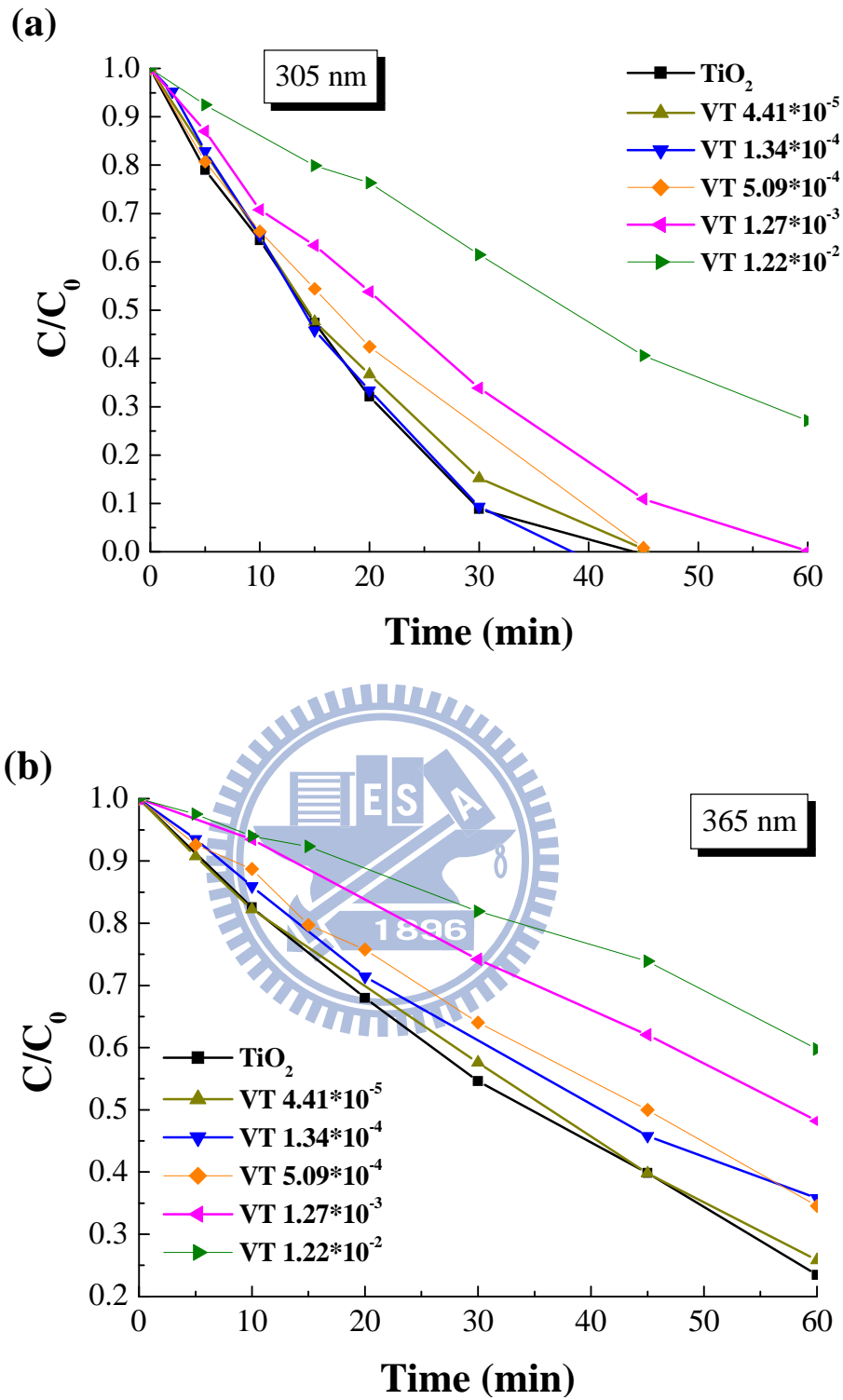


Figure 4-17 The decoloration of 0.01 mM RhB by pure and bulk doped TiO<sub>2</sub> under (a) 305 nm and (b) 365 nm UV irradiation.

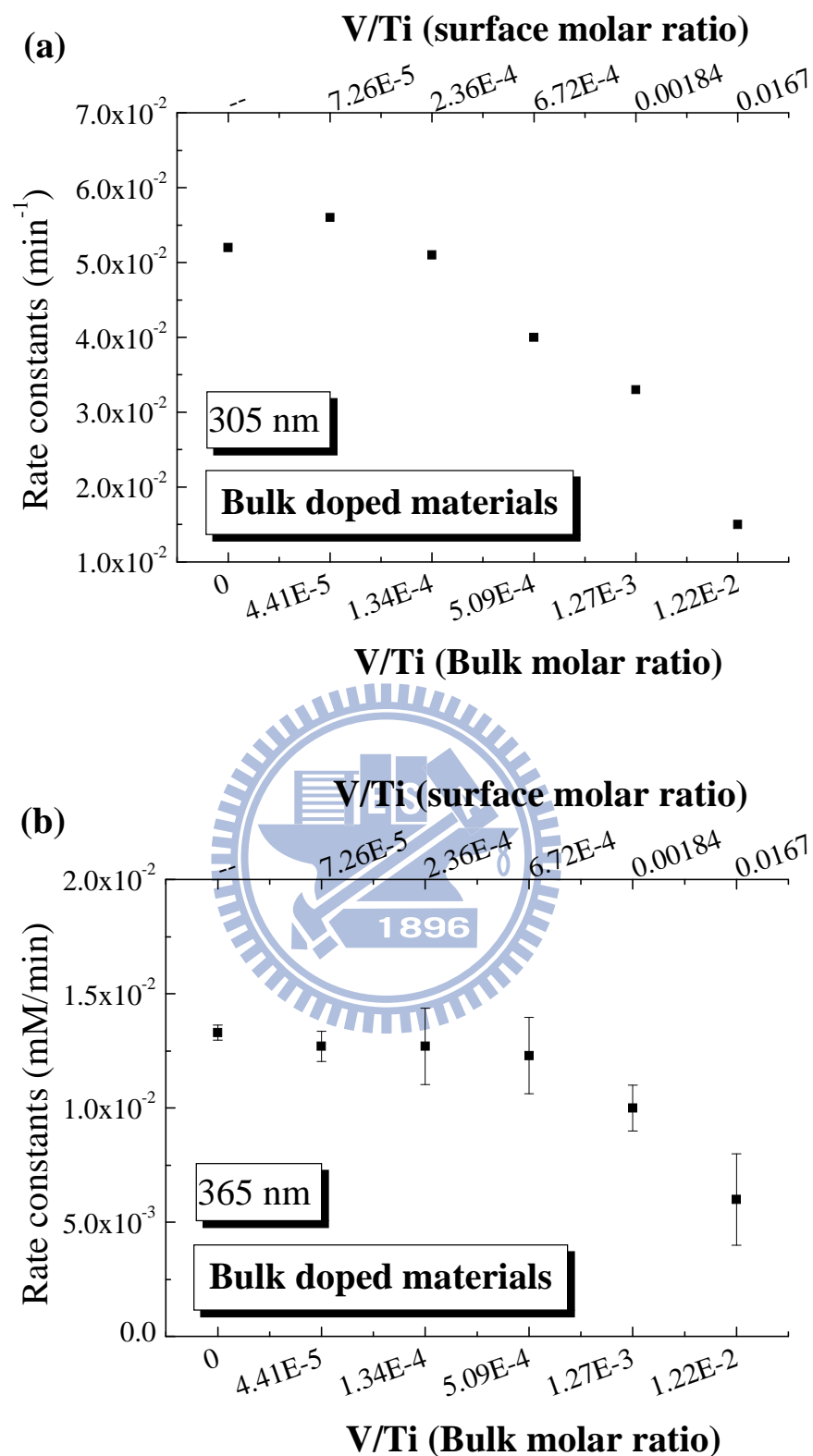


Figure 4-18 The rate constants of bulk doped materials at various vanadium ions concentration compared with pure  $\text{TiO}_2$  under (a) 305 nm UV and (b) 365 nm UV irradiation.

Table 4-7 The rate constants of bulk doped TiO<sub>2</sub> at various vanadium concentration compared with pure TiO<sub>2</sub> under 365 and 305 nm UV irradiation.

Bulk doped TiO <sub>2</sub>			
Sample name	Surface V/Ti ratio <sup>a</sup>	Rate constants at 365 nm UV irradiation (mM/min)	Rate constants at 305 nm UV irradiation (min <sup>-1</sup> )
TiO <sub>2</sub>	- <sup>b</sup>	$1.33 \times 10^{-2} \pm 3.33 \times 10^{-4}$	$5.20 \times 10^{-2}$
VT $4.41 \times 10^{-5}$	$7.26 \times 10^{-5}$	$1.27 \times 10^{-2} \pm 6.67 \times 10^{-4}$	$5.60 \times 10^{-2}$
VT $1.34 \times 10^{-4}$	$2.36 \times 10^{-4}$	$1.27 \times 10^{-2} \pm 1.67 \times 10^{-3}$	$5.10 \times 10^{-2}$
VT $5.09 \times 10^{-4}$	$6.72 \times 10^{-4}$	$1.23 \times 10^{-2} \pm 1.67 \times 10^{-3}$	$4.00 \times 10^{-2}$
VT $1.27 \times 10^{-3}$	$1.84 \times 10^{-3}$	$1.00 \times 10^{-2} \pm 2.00 \times 10^{-3}$	$3.30 \times 10^{-2}$
VT $1.22 \times 10^{-2}$	$1.67 \times 10^{-2}$	$6.00 \times 10^{-3} \pm 2.00 \times 10^{-3}$	$1.50 \times 10^{-2}$

<sup>a</sup> determined by SIMS. <sup>b</sup> not available.

For pure TiO<sub>2</sub> with 305 nm irradiation, the rate constant was  $5.20 \times 10^{-2} \text{ min}^{-1}$ . When the V/Ti ratio increased to  $1.34 \times 10^{-4}$ , the photoactivity increased to  $6.10 \times 10^{-2} \text{ min}^{-1}$  which was similar to pure TiO<sub>2</sub>. The photo-electrons were trapped in bulk-V<sup>5+</sup> sites which position was lower than upper CB after 305 nm UV irradiation while the lots of generated holes performed at the same time. Unfortunately, it was hard to confirm the photo-holes migrated to surface and reacted with donors without recombined with electrons. Moreover, the photocatalytic activities of bulk doped materials with low vanadium-ion doping were similar to pure TiO<sub>2</sub>. Nevertheless, when the bulk V/Ti higher than 1.00 atomic percent, the photoactivity decreased from  $6.10 \times 10^{-2}$  to  $1.50 \times 10^{-2} \text{ min}^{-1}$ . Because parts of generated holes were trapped by V<sup>4+</sup> ions reduced from V<sup>5+</sup>, the trapped holes could not react with donors. Moreover, the substitution V<sup>4+</sup> in the lattice of quantum-size TiO<sub>2</sub> acted primarily as a charge-carrier recombination center that with a net reduction:  $V^{3+} + V^{5+} \rightarrow 2 V^{4+}$  when the electrons/holes were hard to migrate to surface and react with acceptors/donors, as shown in Figure 4-19.<sup>14</sup>

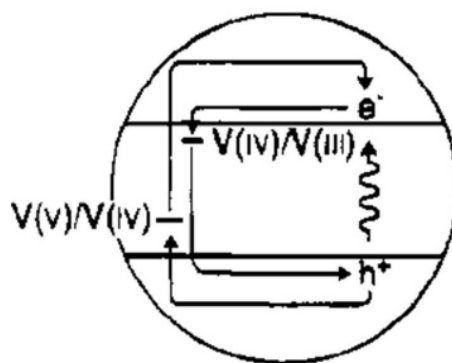


Figure 4-19 The concept of higher content  $V^{4+}$  at substitutional site in Q-size  $TiO_2$  lattice.<sup>14</sup>

Figure 4-20 displays photocatalytic activity of surface doped  $TiO_2$  irradiated with UV light at 365 and 305 nm. The photodecomposition of RhB was followed pseudo-first-order kinetics with 305 nm irradiation and it was followed zero-order kinetics with 365 nm irradiation. The tendency of photoactivities with 305 nm was similar to 365 nm irradiation. Therefore, the mechanism of photocatalysis at 305 nm irradiation was discussed since all surface doped  $TiO_2$  exhibited anatase form and similar band gaps (3.1 eV); it suggested that the surface structural properties had a greater influence on the photoactivities rather than the bulk ones do.

Figure 4-21 displays the dependence of photocatalytic rate constants of surface doped  $TiO_2$  on the V/Ti ratios under irradiation of UV light at 365 and 305 nm. Table 4-8 lists the dependence of photocatalytic rate constants of the surface doped  $TiO_2$  irradiated with 305 and 365 nm UV light on the various V/Ti ratios. And the SVT  $1.10 \times 10^{-2}$  sample ( $k = 9.80 \times 10^{-2} \text{ min}^{-1}$ ) exhibited the highest rate of decomposition of RhB with 305 nm irradiation, followed by SVT  $6.40 \times 10^{-3}$  ( $k = 6.30 \times 10^{-2} \text{ min}^{-1}$ ), SVT  $3.47 \times 10^{-3}$  ( $k = 5.90 \times 10^{-2} \text{ min}^{-1}$ ),  $TiO_2$  ( $k = 5.20 \times 10^{-2} \text{ min}^{-1}$ ), SVT  $5.09 \times 10^{-4}$  ( $k = 4.60 \times 10^{-2} \text{ min}^{-1}$ ). Under 365 UV irradiation, the SVT  $1.10 \times 10^{-2}$  sample ( $k = 1.80 \times 10^{-2} \text{ mM/min}$ ) exhibited the highest rate of decomposition of RhB, followed by SVT  $6.40 \times 10^{-3}$  ( $k = 1.40 \times 10^{-2} \text{ mM/min}$ ),  $TiO_2$  ( $k = 1.33 \times 10^{-2} \text{ mM/min}$ ), SVT  $3.47 \times 10^{-3}$  ( $k = 1.25 \times 10^{-2} \text{ mM/min}$ ), SVT  $5.09 \times 10^{-4}$  ( $k = 1.07 \times 10^{-2} \text{ mM/min}$ ).

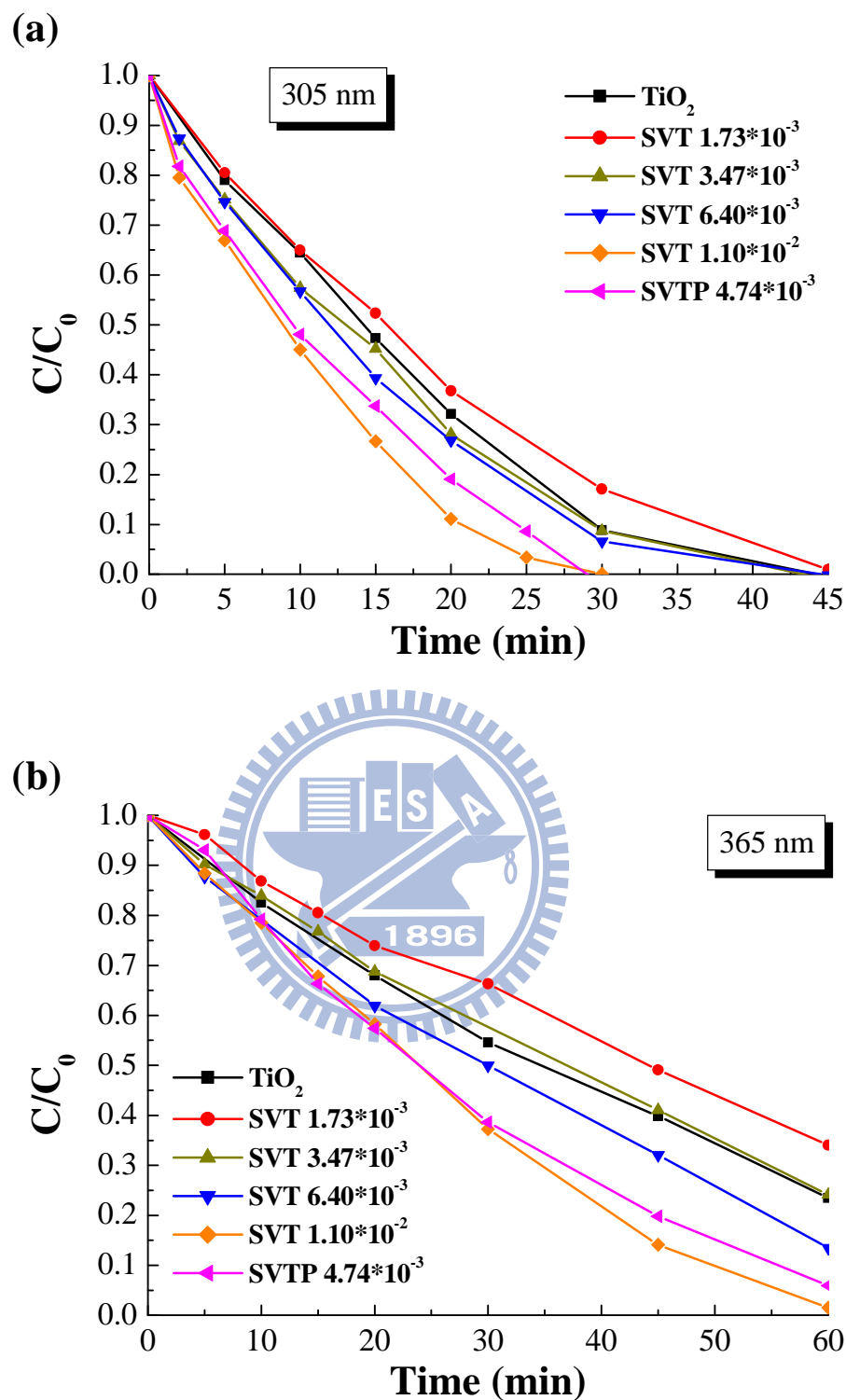


Figure 4-20 The decoloration of 0.01 mM RhB by surface doping materials at various vanadium ions concentration compared with pure  $\text{TiO}_2$  under (a) 305 nm UV and (b) 365 nm UV irradiation.

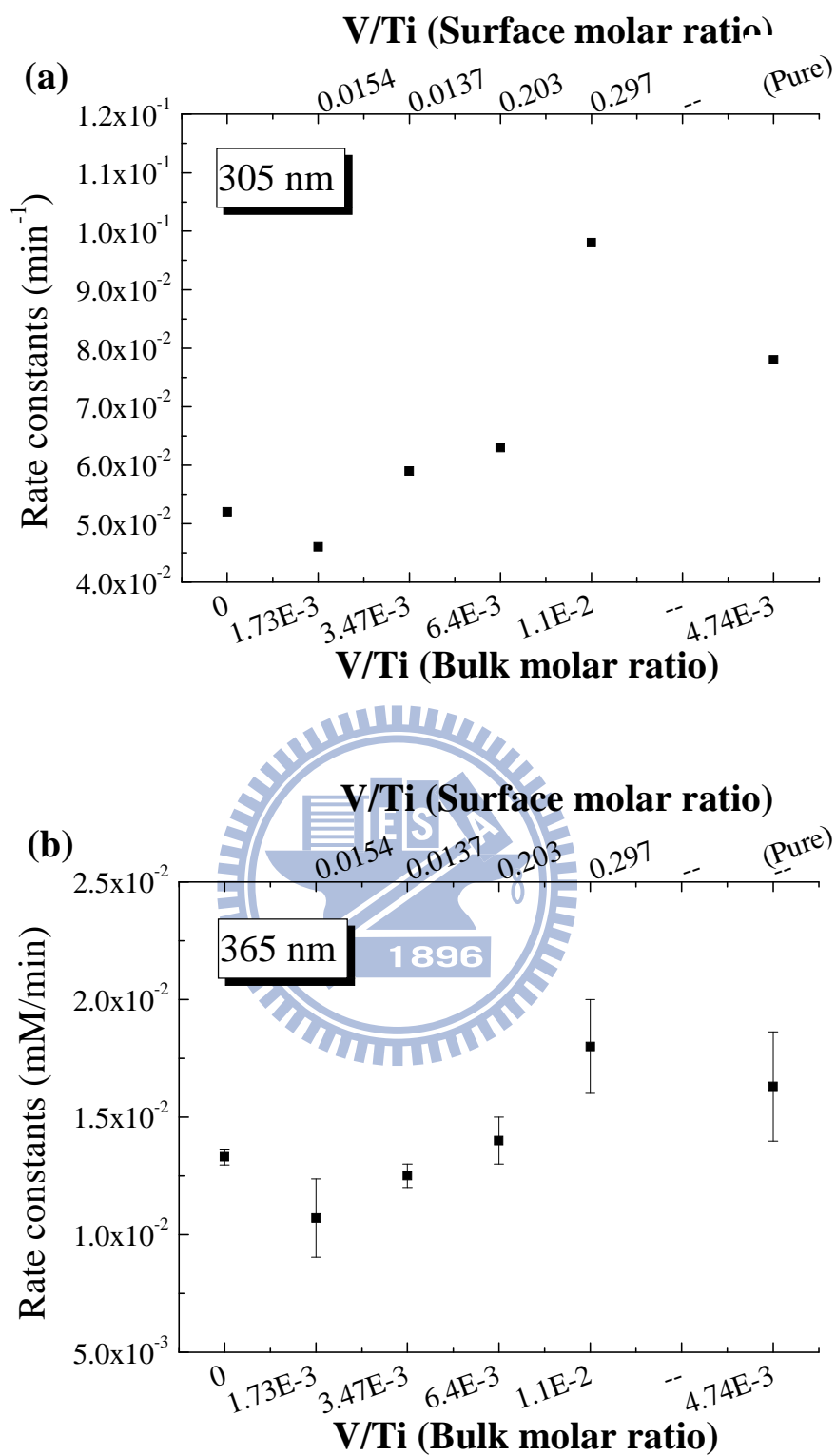


Figure 4-21 The rate constants of surface doped materials at various vanadium ions concentration compared with pure  $\text{TiO}_2$  under (a) 305 nm UV and (b) 365 nm UV irradiation.

Table 4-8 The rate constants of the surface doped TiO<sub>2</sub> at various V/Ti ratios.

Surface doped TiO <sub>2</sub>			
Sample name	Surface V/Ti <sup>a</sup>	Rate constants at 365 nm UV irradiation (mM/min)	Rate constants at 305 nm UV irradiation (mM/min)
SVT 1.73×10 <sup>-3</sup>	2.97×10 <sup>-1</sup>	1.07×10 <sup>-2</sup> ± 1.67×10 <sup>-3</sup>	4.60×10 <sup>-2</sup>
SVT 3.47×10 <sup>-3</sup>	2.03×10 <sup>-1</sup>	1.25×10 <sup>-2</sup> ± 5.00×10 <sup>-4</sup>	5.90×10 <sup>-2</sup>
SVT 6.40×10 <sup>-3</sup>	1.37×10 <sup>-1</sup>	1.40×10 <sup>-2</sup> ± 1.00×10 <sup>-3</sup>	6.30×10 <sup>-2</sup>
SVT 1.10×10 <sup>-2</sup>	1.54×10 <sup>-2</sup>	1.80×10 <sup>-2</sup> ± 2.00×10 <sup>-3</sup>	9.80×10 <sup>-2</sup>

<sup>a</sup> determined by SIMS.

For pure TiO<sub>2</sub>, the rate constant was 6.30×10<sup>-2</sup> min<sup>-1</sup>. When the V/Ti ratio increased to 1.73×10<sup>-3</sup>, the photoactivity of surface doped materials decreased to 4.60×10<sup>-2</sup> min<sup>-1</sup>. The low photocatalytic activity was attributed to improved charge recombination at surface defect sites. When the V/Ti atomic ratios ranged between 3.47×10<sup>-3</sup> - 6.40×10<sup>-3</sup>, the rate constants were similar to pure TiO<sub>2</sub>. In contrast to the pure and V-doped TiO<sub>2</sub>, the photocatalytic activities of SVT 1.10×10<sup>-2</sup> showed the highest photoactivity (i.e. 9.80×10<sup>-2</sup> min<sup>-1</sup>), which was 2 times higher than that of pure TiO<sub>2</sub>. The existence of V<sub>2</sub>O<sub>5</sub> shell on the surface promoted charge diffusion to its conduction band and then effectively conducted the charge carriers to adsorbed reactants to enhance the photocatalytic activity at high V/Ti ratios.

#### 4-6 EPR studies of bulk and surface doping materials

EPR technique was used to gain the information about the nature of vanadium species in the V-doped TiO<sub>2</sub> and to understand their photocatalytic mechanism. All the data were acquired with UV irradiation or in the dark at 77K. Figure 4-22 illustrates the EPR spectra of the pure TiO<sub>2</sub> before and after UV irradiation at 77K. There was no observable peak appear in the dark. However, after irradiation with UV light, one of additional signals at  $g_1 = 2.011$ ,  $g_2 = 2.007$ , and  $g_3 = 2.002$  was detected, denoting trapped holes at surface O<sup>-</sup> sites. The other one at  $g = 2.06$  was detected, denoting superoxide radical anion (O<sub>2</sub><sup>-</sup>).<sup>81, 82</sup> However, the Ti<sup>3+</sup> and •OH did not appear in Figure 4-22 after UV irradiation. Because Ti<sup>3+</sup> ions were easily oxidization to Ti<sup>4+</sup> and the electron transferred to O<sub>2</sub> which was adsorption on the surface of TiO<sub>2</sub>, oxygen was chemically adsorbed by O<sub>2</sub><sup>2-</sup> ion at room to low temperature process. Besides, O<sub>2</sub><sup>2-</sup> simultaneously had hole-reduction agent and electron consumed

agent function, and  $O_2^-$  was the product by hole/electron consumed reaction. That is why  $O_2^-$  signal can be detected in EPR system after UV irradiation with low vanadium concentration.<sup>83</sup> In addition, after UV irradiation, a little parts of photo electrons transferred to surface and reacted with oxygen to perform superoxide radical anion ( $O_2^{\cdot-}$ ) while holes were trapped by oxygen vacancy. Therefore, the superoxide radical anions and trapped holes were detected in EPR spectra, as shown in Figure 4-22.

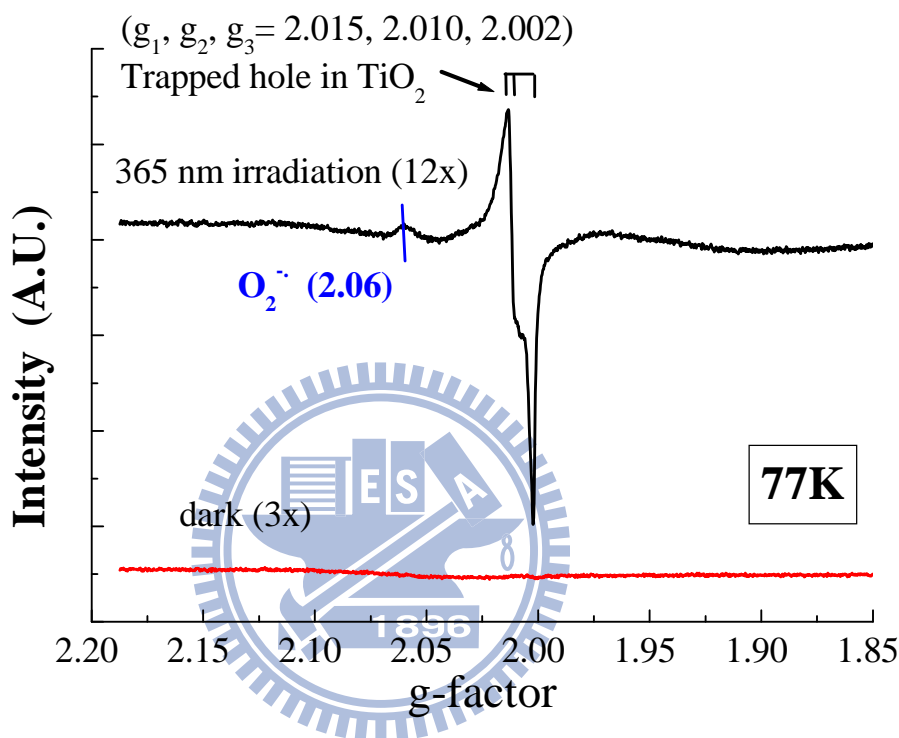


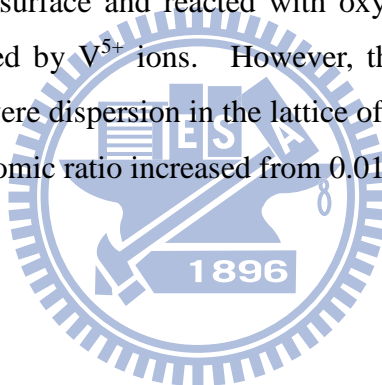
Figure 4-22 The difference in EPR spectra of pure  $TiO_2$  before and after irradiation of UV at 77K.

Figure 4-23 displays the EPR spectra of the bulk doped  $TiO_2$  at various vanadium concentrations in the dark at 77K. The observable peaks denoted vanadium ions were found in the dark at 77K. The hyperfine structure of  $V^{4+}$  ions of bulk doped materials were resulted from the interaction between the unpaired  $3d^1$  electron and the vanadium nucleus spin ( $I = 7/2$ ). Thus, Figure 4-24 shows eight lines, leading to the following EPR parameters:  $g_{\perp} = 1.985$ .<sup>84</sup> The results indicate that a portion of  $V^{5+}$  ions, which can not be detected by EPR, were reduced to  $V^{4+}$ . The remaining  $V^{4+}$  diffused into the anatase lattice as substitutional  $V^{4+}$ . Figure 4-25 shows the EPR spectra of the bulk doped  $TiO_2$  at various vanadium concentrations under UV irradiation at 77K. Compared with pure  $TiO_2$ , the trapped holes increased while V/Ti ratios increased from 0 to  $1.34 \times 10^{-4}$ . The intensity of trapped holes



showed a downturn when V/Ti increased from  $5.09 \times 10^{-4}$  to  $1.27 \times 10^{-3}$ . However, when the bulk V/Ti ratio was higher than  $1.22 \times 10^{-2}$ , only  $V^{4+}$  ions were observed in the EPR spectra.

Figure 4-25 shows three types of phenomena, denoting to low, intermediate and high vanadium concentration. For low vanadium concentration, two additional peaks occurred after UV irradiation, denoting to superoxide radical anions and trapped holes. It seemed that parts of photo electrons were trapped by  $V^{5+}$  ions spread in the lattice of  $TiO_2$  while photo holes increased simultaneously. In addition, some excited electrons transferred to surface and reacted with oxygen to perform superoxide radical anion ( $O_2^{\cdot-}$ ). The residual excited electrons remained in conduction band of  $TiO_2$  or were trapped by  $Ti^{4+}$  ions, which were not detected by EPR. Therefore, compared with  $TiO_2$ , the trapped holes of surface doped  $TiO_2$  increased when some photo electrons were trapped by bulk- $V^{5+}$ . At intermediate vanadium concentration, three additional peaks, including superoxide radical anions, trapped holes and  $V^{4+}$  ions were observed in Figure 4-25 after UV irradiation. It referred the parts of excited electrons were migrated to surface and reacted with oxygen to perform superoxide radical anions ( $O_2^{\cdot-}$ ) or were trapped by  $V^{5+}$  ions. However, the other parts of photo holes were trapped by  $V^{4+}$  ions which were dispersion in the lattice of  $TiO_2$ . So, the intensity of trapped holes declined while V/Ti atomic ratio increased from 0.01 % to 0.1 %.



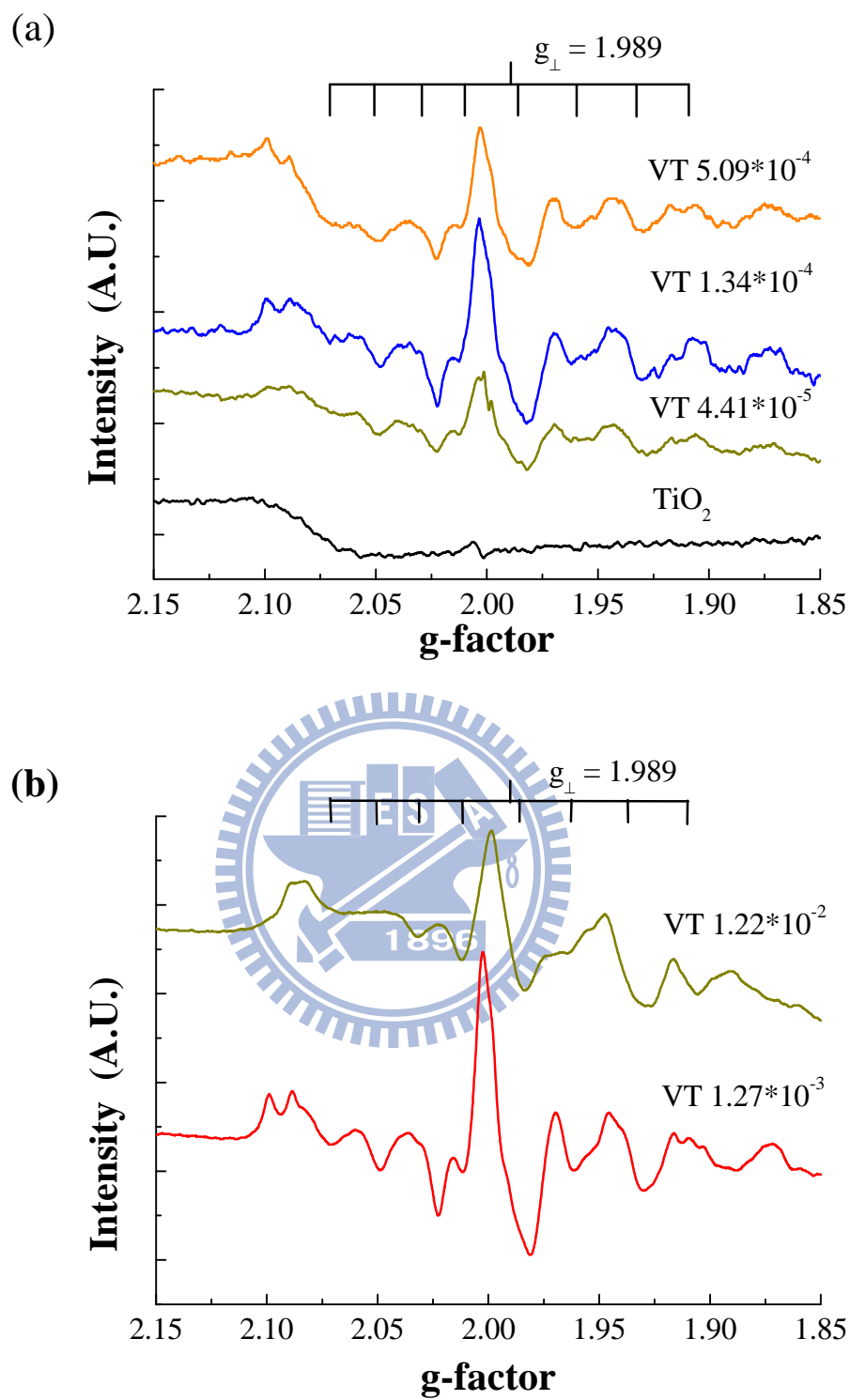


Figure 4-23 EPR spectra of pure and bulk doped TiO<sub>2</sub> at different vanadium contents at 77K in the dark. (a) The bulk V/Ti ratios ranged 0- $5.09 \times 10^{-4}$  and (b) The bulk V/Ti ratios in the range  $1.27 \times 10^{-3}$ - $1.22 \times 10^{-2}$ .

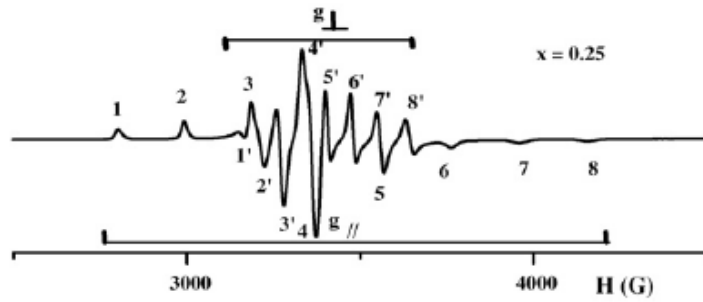


Figure 4-24 The EPR spectra of vanadium ions doped in  $\text{TiO}_2$ .<sup>84</sup>

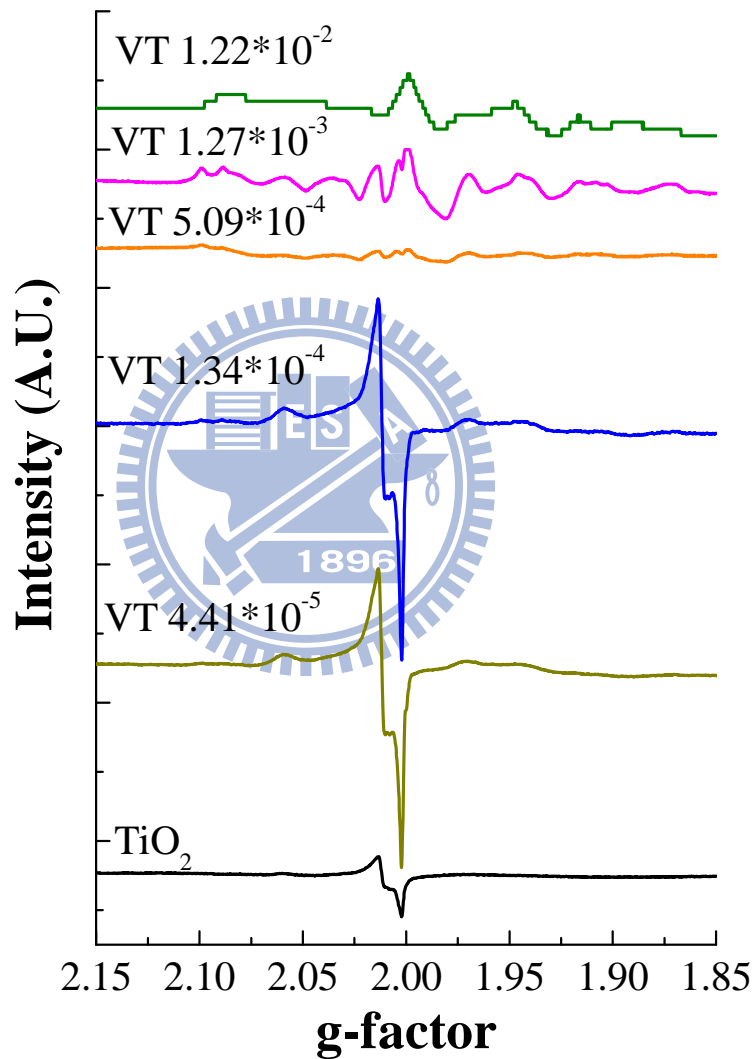


Figure 4-25 EPR spectra of bulk doped materials at various vanadium concentrations under UV irradiation at 77K.

With high vanadium concentration, only eight peaks denoted  $\text{V}^{4+}$  ( $g_{\perp} = 1.989$ ) were found before and after UV irradiation. It indicated the photo-electrons and photo-holes were both trapped by  $\text{V}^{4+}$ , besides the trapped electrons recombined with trapped holes easily.

Moreover, even  $V_2O_5$  crystalline structure formed on the surface of VT  $1.22 \times 10^{-2}$ , its photocatalytic activity was 2.5 times lower than that of pure  $TiO_2$  since only few excited electrons/holes transferred to surface and reacted with accepters/donors. Therefore, bulk- $V^{4+}$  ions dispersion in the lattice of  $TiO_2$  had negative effect on charge diffusions.

To summary the photocatalytic mechanism bulk doped materials; the phenomena separated three parts are shown in Figure 4-26 to Figure 4-28, such as low vanadium concentration, intermediate vanadium concentration and high vanadium concentration. In the three figures, the red square meant the species can be detected by EPR and the other ones meant can not be detected by EPR.

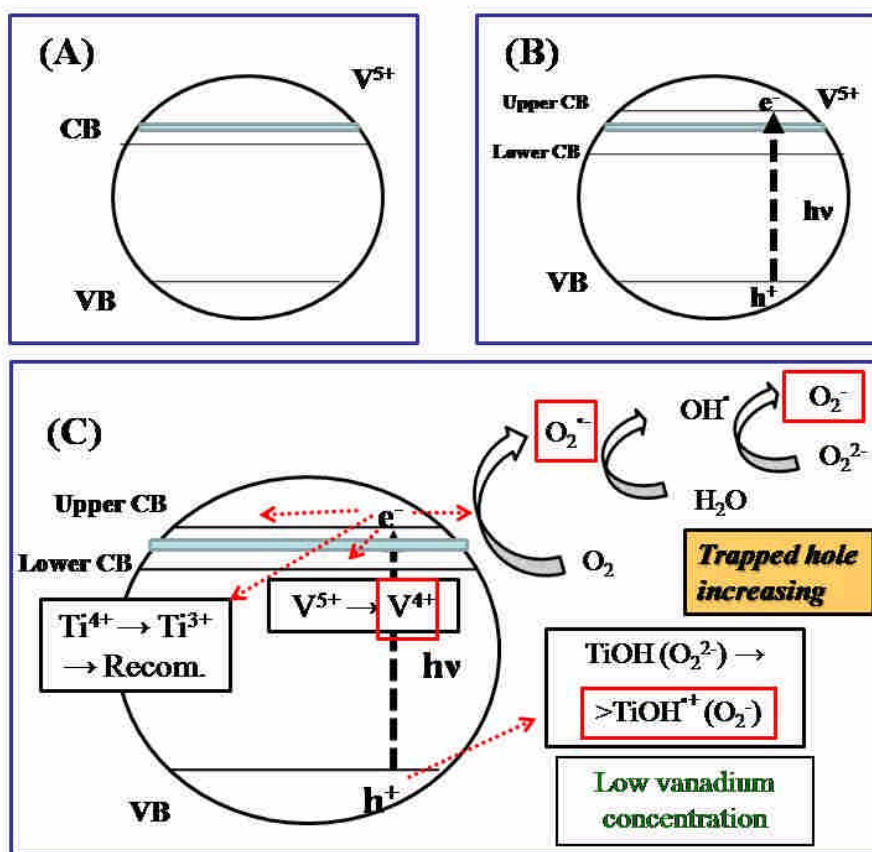


Figure 4-26 The concept of bulk doping materials at low vanadium concentration.

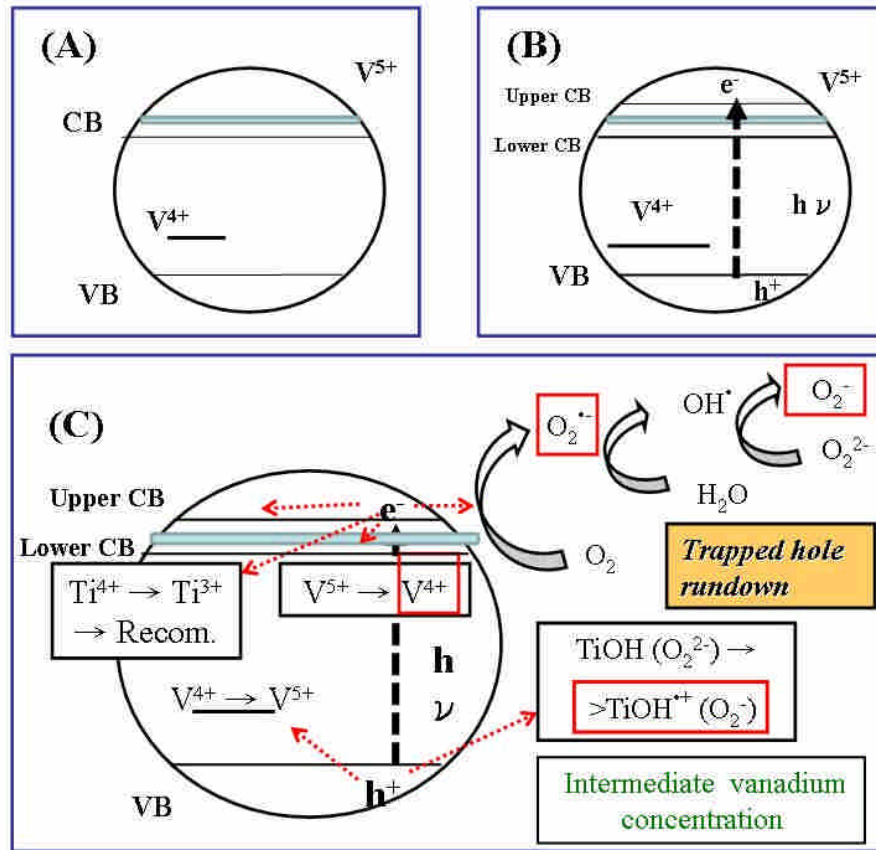


Figure 4-27 The concept of bulk doping materials at intermediate vanadium concentration.



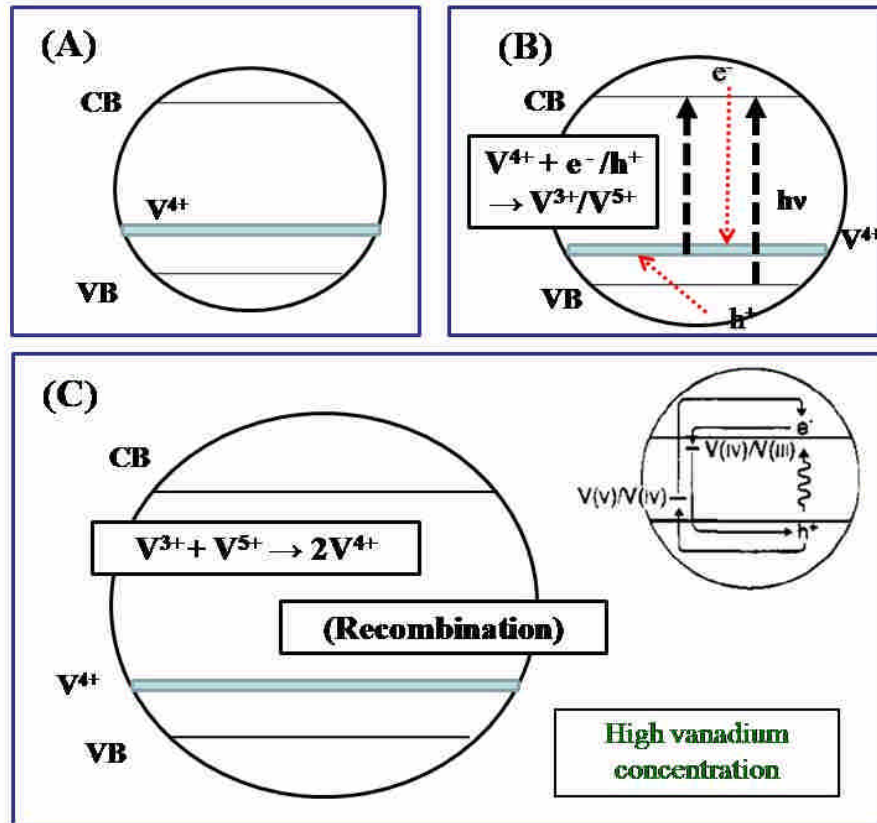


Figure 4-28 The concept of bulk doping materials at high vanadium concentration.<sup>14</sup>

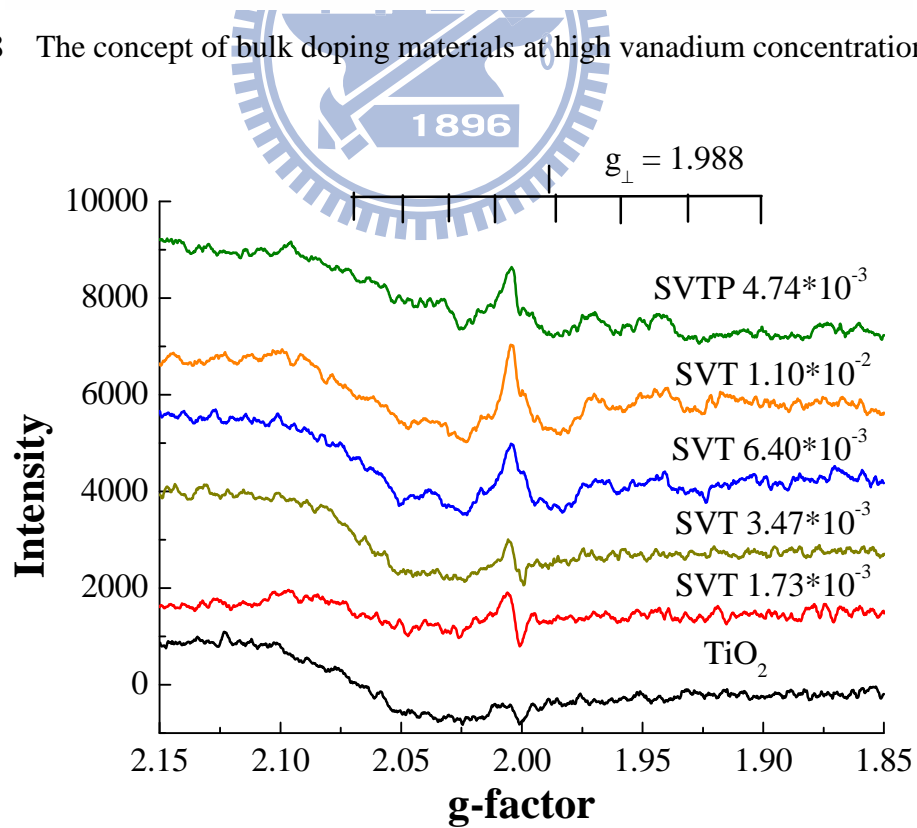
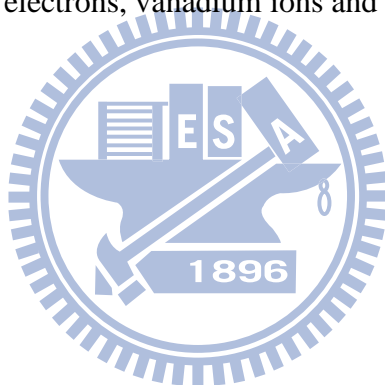


Figure 4-29 EPR spectra of surface doping materials at various vanadium concentration in the dark at 77K.

Figure 4-29 shows EPR spectra of surface doped TiO<sub>2</sub> at various vanadium concentration in the dark at 77K. The V<sup>4+</sup> signals except SVT 1.73×10<sup>-3</sup> and SVT 3.47×10<sup>-3</sup> were detected, because the concentration of the V<sup>4+</sup> ions were too low to be detected by EPR. Figure 4-30 displays EPR spectra of surface doped TiO<sub>2</sub> at various vanadium concentrations under UV irradiation at 77K. The addition of three peaks, including superoxide radical anions, trapped holes and V<sup>4+</sup> ions were observed after UV irradiation. The appearance of V<sup>4+</sup> indicated trapping photo-generated electrons by surface V<sup>5+</sup> ions. Because the surface-V<sup>5+</sup> has higher ionic charge and smaller ionic radius than Ti<sup>4+</sup>, the electrons migrated to surface is more readily.<sup>19</sup> In addition, the photocatalytic mechanism of surface doped TiO<sub>2</sub> is shown in Figure 4-31. The photo electrons were trapped by surface-V<sup>5+</sup> while trapped holes/electrons were easily migrated to surface and reacted with donors/acceptors. Thus, the photocatalytic activity of surface doped TiO<sub>2</sub> increased with the increasing vanadium-ion contents. Besides, Table 4-9 lists the g-factor of EPR for easy reference. The EPR data are separated four parts, i.e. as trapped holes, trapped electrons, vanadium ions and radicals.



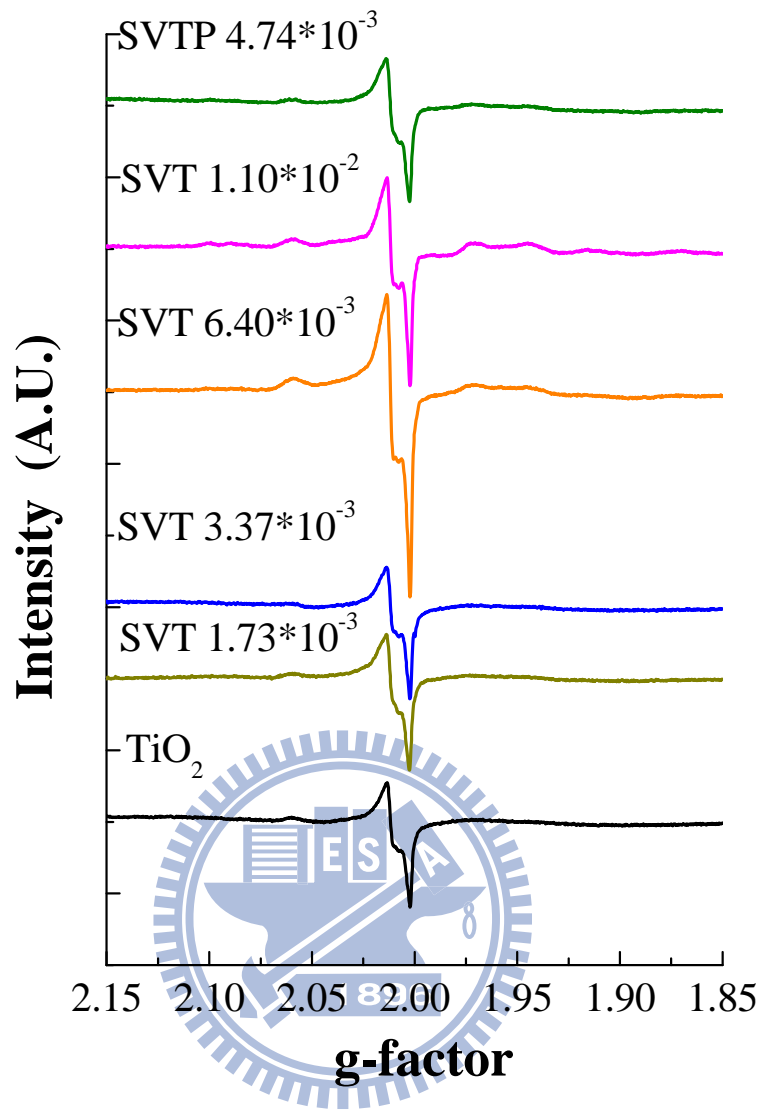


Figure 4-30 EPR spectra of surface doped materials at various vanadium concentrations under UV light at 77K.



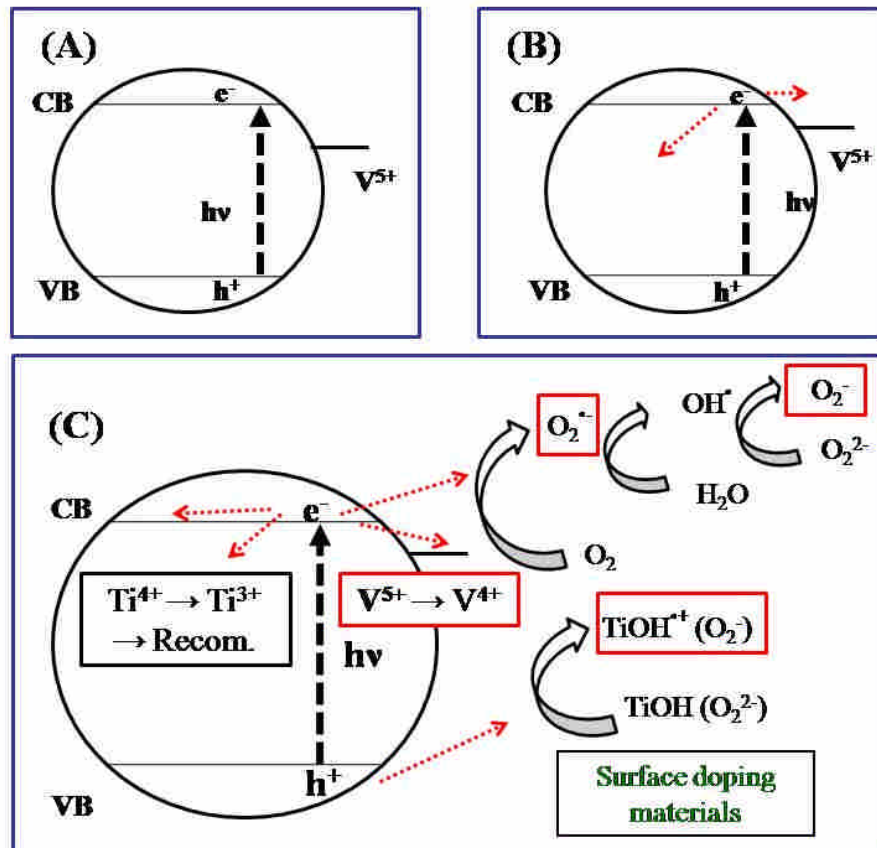


Figure 4-31 The concept of surface doped materials.

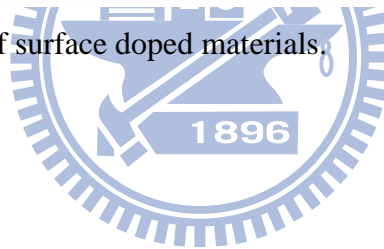


Table 4-9 g value for various paramagnetic species.

g factor	assignment	Ref.
$g_1 = 1.961 ; g_2 = 1.992 ; g_3 = 1.992$	Inner $Ti^{3+}$ (interstitial, colloidal $TiO_2$ )	13, 85
$g_1 = 1.960 ; g_2 = 1.990 ; g_3 = 1.990$	Electron trapping sites (anatase)	86
$g_{\perp} = 1.990 ; g_{\parallel} = 1.957$	Lattice electron trapping sites (anatase)	37
$g_{\perp} = 1.975 ; g_{\parallel} = 1.940$	Lattice electron trapping sites (rutile)	37
$g_1 = 2.002 ; g_2 = 2.011 ; g_3 = 2.018$	$Ti^{4+}O^{\cdot-}Ti^{4+}OH^-$ (hydrated anatase)	13, 85
$g_1 = 2.004 ; g_2 = 2.018 ; g_3 = 2.030$	$Ti^{4+}O^{2-}Ti^{4+}O^{\cdot-}$ (surface, colloidal $TiO_2$ )	13, 85
$g_1 = 2.002 ; g_2 = 2.012 ; g_3 = 2.016$	Trapped hole in $TiO_2$	86, 87
$g_1 = 2.007 ; g_2 = 2.014 ; g_3 = 2.024$	Trapped hole in $TiO_2$	14
$g_3 = 2.06$	$O_2^{\cdot-}$ (on $TiO_2$ , adsorbed oxygen)	13, 85
$g_1 = 2.001 ; g_2 = 2.009 ; g_3 = 2.021$	$O_2^{\cdot-}$ (on anatase)	14
$g_1 = 2.003 ; g_2 = 2.009 ; g_3 = 2.025$	$O_2^{\cdot-}$ (on anatase)	86
$g_{\perp} = 1.913 ; g_{\parallel} = 1.980$	$V^{4+}$ (amorphous $V_2O_5$ )	58
$g_{\perp} = 1.932 ; g_{\parallel} = 1.975$	$V^{4+}$ (hydrated $V_2O_5$ )	58
$g_{\perp} = 1.923 ; g_{\parallel} = 1.986$	$V^{4+}$ (crystalline $V_2O_5$ )	58
$g_z = 1.911 ; g_x = 1.983$	$V^{4+}$ (in $V_2O_5$ )	14
$g_1 = 1.912 ; g_2 = 1.914 ; g_3 = 1.956$	$V^{4+}$ ( in $TiO_2$ ) surface	57
$g_1 = 1.913 ; g_2 = 1.915 ; g_3 = 1.956$	$V^{4+}$ ( in $TiO_2$ ) surface	58
$g_1 = 1.912 ; g_2 = 1.914 ; g_3 = 1.956$	$V^{4+}$ (in rutile ) surface	57
$g_{\perp} = 1.960 ; g_{\parallel} = 1.932$	$V^{4+}$ ( in anatase ) surface	57, 88
$g_z = 1.940 ; g_x = 1.986 ; g_y = 1.993$	$V^{4+}$ ( in rutile ) bulk	14, 58

DMPO spin trapping EPR experiments have been carried out to detect free radical intermediates generated during the irradiation process and to provide essential information on understanding the reaction mechanism. In order to understand the ability of interfacial charge transfer of the bulk and surface doped materials, the generation of  $\bullet OH$  were detected via EPR. Figure 4-32 shows the EPR spectrum of DMPO ( $3.00 \times 10^{-2}$  M) to  $O_2$ -saturated aqueous solutions, followed by in situ light irradiation of UV light. Its EPR parameters are characteristic of  $\bullet OH$ -DMPO adducts formed upon trapping of OH radicals by the DMPO

molecules. Figure 4-32 shows the signals identified the characteristic •OH-DMPO occurred since the UV light can decompose water to perform •OH.

Table 4-10 summarizes •OH generated in the bulk doped TiO<sub>2</sub> suspensions irradiated with UV light. The integrated area of •OH signals increased from  $3.24 \times 10^7$  to  $8.18 \times 10^7$  when the bulk V/Ti ratios increased from 0 to  $1.22 \times 10^{-2}$ . The •OH-DMPO adduct decayed because two •OH, which performed on the surface of materials, recombined together while its can not detected by EPR, as shown in Figure 4-33.<sup>89</sup> Moreover, the decreasing integrated area were caused by recombination of two •OH since too many •OH produced by reaction between generated electrons/holes and oxygen/water. For examples, the generated •OH on the surface declined due to the photo electrons/holes were both trapped by V<sup>4+</sup> ions, which was doped in the bulk lattice of VT  $1.22 \times 10^{-2}$ . Moreover, the integrated area of •OH was higher than pure TiO<sub>2</sub>.

Table 4-11 lists integrated area of •OH of surface doped TiO<sub>2</sub>. The integrated area of •OH signals decreased from  $6.57 \times 10^7$  to  $4.42 \times 10^7$  when the bulk V/Ti ratios increased from 0 to  $1.10 \times 10^{-2}$ . The generation of •OH increased with increasing vanadium ions, because the excited electrons were trapped by surface V<sup>5+</sup> which migrated to surface easily, especially SVT  $1.10 \times 10^{-2}$ . Thus, relative to photoactivitiy of V-doped TiO<sub>2</sub>, substantial recombination centers at V<sup>4+</sup> sites lead to detrimental effects on the low photocatalytic activity of bulk doped samples. However, surface-V<sup>5+</sup> promotes electrons diffusion to surface and further facilities charges transfer to reactants, thereby greatly improving the degradation efficiency.

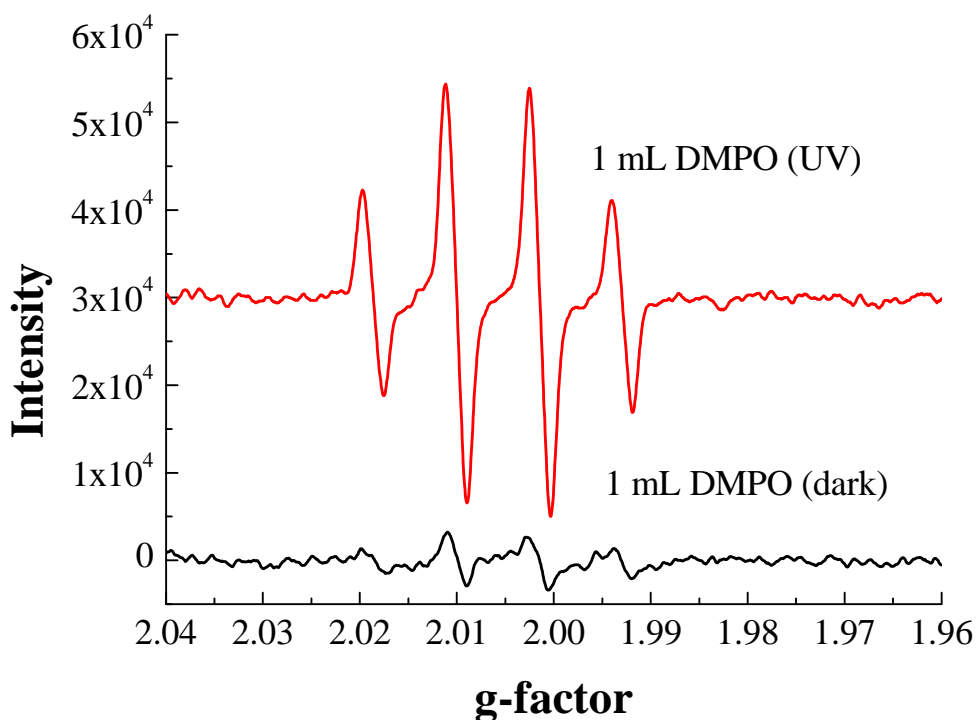
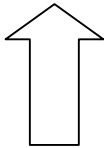


Figure 4-32 The ERP spectrum of •OH-DMPO in the dark and UV irradiation.

Table 4-10 The integrated areas of •OH-DMPO signals obtained from the bulk doped TiO<sub>2</sub> suspension under UV irradiation. The suspensions were aerated with O<sub>2</sub> for 30 min in the dark before irradiation.

Bulk doped TiO <sub>2</sub>			
Sample name	Integrated area	Calibrated values <sup>a</sup>	Photoactivity
1 mL DMPO	$8.64 \times 10^7$	- <sup>b</sup>	- <sup>b</sup>
TiO <sub>2</sub>	$3.24 \times 10^7$	$5.40 \times 10^7$	 <b>Increase</b>
VT $4.41 \times 10^{-5}$	$4.92 \times 10^7$	$3.72 \times 10^7$	
VT $1.34 \times 10^{-4}$	$5.43 \times 10^7$	$3.21 \times 10^7$	
VT $5.09 \times 10^{-4}$	$5.93 \times 10^7$	$2.71 \times 10^7$	
VT $1.27 \times 10^{-3}$	$6.34 \times 10^7$	$2.30 \times 10^7$	
VT $1.22 \times 10^{-2}$	$8.19 \times 10^7$	$5.50 \times 10^6$	

<sup>a</sup>calibrated values= integrated area of DMPO – integrated area of samples. <sup>b</sup> not available.

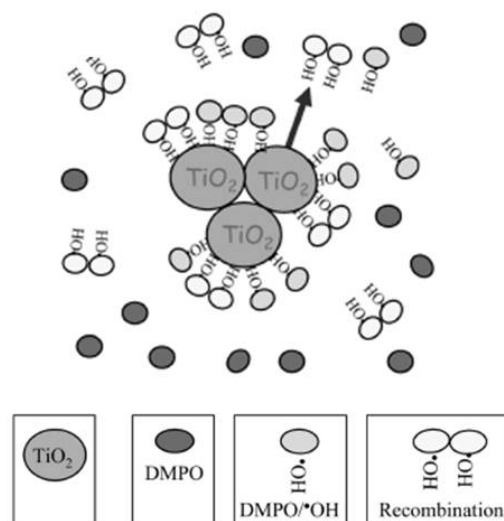


Figure 4-33 The mechanism of •OH-DMPO adducts formed upon trapping of OH radicals by the DMPO molecules.<sup>89</sup>

Table 4-11 The integrated areas of •OH-DMPO signals obtained from the surface doped TiO<sub>2</sub> suspension under UV irradiation. The suspensions were aerated with O<sub>2</sub> for 30 min in the dark before irradiation.

Surface doped TiO <sub>2</sub>			
Sample name	Integrated area	Calibrated values <sup>a</sup>	Photoactivity
TiO <sub>2</sub>	$6.57 \times 10^7$	$2.07 \times 10^7$	 <b>Increase</b>
SVT $1.73 \times 10^{-3}$	$5.94 \times 10^7$	$2.70 \times 10^7$	
SVT $3.47 \times 10^{-3}$	$6.25 \times 10^7$	$2.39 \times 10^7$	
SVT $6.40 \times 10^{-3}$	$5.77 \times 10^7$	$2.77 \times 10^7$	
SVT $1.10 \times 10^{-2}$	$4.42 \times 10^7$	$4.22 \times 10^7$	

<sup>a</sup>calibrated values= integrated area of DMPO – integrated area of samples.

## Chapter 5 Conclusions

In this study, the influence of bulk and surface doping sites on chemical compositions, photoactivity, electronic- and micro- structure of V-doped TiO<sub>2</sub> were discussed. V<sub>2</sub>O<sub>5</sub> was formed on the surface because the low Tammann temperature induced the diffusion of vanadium ions from bulk lattice toward surface lattice. In addition, some incorporated V<sup>5+</sup> ions were reduced to V<sup>4+</sup> ions when the bulk V/Ti ratios higher than 1 mol%. The lattice V<sup>5+</sup>/V<sup>4+</sup> not only decreased the anatase-rutile transformation at 300 °C but also inhibited growth of crystal size of anatase TiO<sub>2</sub> at high vanadium concentration. In bulk doped TiO<sub>2</sub>, lattice-V<sup>5+</sup> ions trapped electrons thus increased the number of trapped holes. However, the trapped holes decreased when V/Ti ratios were higher than 1 mol% because lattice-V<sup>4+</sup> ions acted as recombination centers. Prompt charge recombination led to the decrease in photoactivities of bulk doped TiO<sub>2</sub> with increasing contents of vanadium ions. In contrast to bulk doped TiO<sub>2</sub>, V<sub>2</sub>O<sub>5</sub> shell was coated on the surface of TiO<sub>2</sub> when vanadium ions were doped in the surface lattice of TiO<sub>2</sub>. The surface-V<sup>5+</sup> ions had no obvious effect on the micro- and electronic- structure of TiO<sub>2</sub>. However, they promoted electrons diffusion to surface and further facilitates charges transfer to reactants because the d-orbital energy of V<sup>5+</sup> was lower than that of conduction band of titanium. Therefore, the surface defects contributed to high photoactivity, while bulk ones had detrimental effects on photodegradation of RhB under irradiation of UV light.

## References

1. Di Paola, A.; Garcia-Lopez, E.; Ikeda, S.; Marci, G.; Ohtani, B.; Palmisano, L., Photocatalytic degradation of organic compounds in aqueous systems by transition metal doped polycrystalline TiO<sub>2</sub>. *Catalysis Today* **2002**, 75, (1-4), 87-93.
2. Yuan, Z.; Zhang, J. L.; Li, B.; Li, J. Q., Effect of metal ion dopants on photochemical properties of anatase TiO<sub>2</sub> films synthesized by a modified sol-gel method. *Thin Solid Films* **2007**, 515, (18), 7091-7095.
3. Xin, B. F.; Ren, Z. Y.; Wang, P.; Liu, J.; Jing, L. Q.; Fu, H. G., Study on the mechanisms of photoinduced carriers separation and recombination for Fe<sup>3+</sup>-TiO<sub>2</sub> photocatalysts. *Applied Surface Science* **2007**, 253, (9), 4390-4395.
4. Bouras, P.; Stathatos, E.; Lianos, P., Pure versus metal-ion-doped nanocrystalline titania for photocatalysis. *Applied Catalysis B-Environmental* **2007**, 73, (1-2), 51-59.
5. Umebayashi, T.; Yamaki, T.; Itoh, H.; Asai, K., Analysis of electronic structures of 3d transition metal-doped TiO<sub>2</sub> based on band calculations. *Journal of Physics and Chemistry of Solids* **2002**, 63, (10), 1909-1920.
6. Park, H.; Choi, W., Photocatalytic reactivities of Nafion-Coated TiO<sub>2</sub> for the degradation of charged organic compounds under UV or visible light. *Journal of Physical Chemistry B* **2005**, 109, (23), 11667-11674.
7. Mrowetz, M.; Balcerski, W.; Colussi, A. J.; Hoffman, M. R., Oxidative power of nitrogen-doped TiO<sub>2</sub> photocatalysts under visible illumination. *Journal of Physical Chemistry B* **2004**, 108, (45), 17269-17273.
8. Reddy, K. M.; Baruwati, B.; Jayalakshmi, M.; Rao, M. M.; Manorama, S. V., S-, N- and C-doped titanium dioxide nanoparticles: Synthesis, characterization and redox charge transfer study. *Journal of Solid State Chemistry* **2005**, 178, (11), 3352-3358.
9. Wang, H.; Lewis, J. P., Second-generation photocatalytic materials: anion-doped TiO<sub>2</sub>. *Journal of Physics-Condensed Matter* **2006**, 18, (2), 421-434.
10. Levy, B., Photochemistry of nanostructured materials for energy applications. *Journal of Electroceramics* **1997**, 1, (3), 239-272.
11. Zhang, J. Z., Interfacial charge carrier dynamics of colloidal semiconductor nanoparticles. *Journal of Physical Chemistry B* **2000**, 104, (31), 7239-7253.
12. Zhao, J. C.; Wu, T. X.; Wu, K. Q.; Oikawa, K.; Hidaka, H.; Serpone, N., Photoassisted degradation of dye pollutants. 3. Degradation of the cationic dye rhodamine B in aqueous anionic surfactant/TiO<sub>2</sub> dispersions under visible light irradiation: Evidence for the need of

- substrate adsorption on TiO<sub>2</sub> particles. *Environmental Science & Technology* **1998**, 32, (16), 2394-2400.
13. Kemp, T. J.; McIntyre, R. A., Transition metal-doped titanium(IV) dioxide: Characterisation and influence on photodegradation of poly(vinyl chloride). *Polymer Degradation and Stability* **2006**, 91, (1), 165-194.
  14. Martin, S. T.; Morrison, C. L.; Hoffmann, M. R., Photochemical Mechanism of Size-Quantized Vanadium-Doped TiO<sub>2</sub> Particles. *Journal of Physical Chemistry* **1994**, 98, (51), 13695-13704.
  15. Klosek, S.; Raftery, D., Visible light driven V-doped TiO<sub>2</sub> photocatalyst and its photooxidation of ethanol. *Journal of Physical Chemistry B* **2001**, 105, (14), 2815-2819.
  16. Balikdjian, J. P.; Davidson, A.; Launay, S.; Eckert, H.; Che, M., Sintering and phase transformation of V-loaded anatase materials containing bulk and surface V species. *Journal of Physical Chemistry B* **2000**, 104, (38), 8931-8939.
  17. Linsebigler, A. L.; Lu, G. Q.; Yates, J. T., Photocatalysis on TiO<sub>2</sub> Surfaces - Principles, Mechanisms, and Selected Results. *Chemical Reviews* **1995**, 95, (3), 735-758.
  18. Haber, J.; Nowak, P., Surface doping of rutile by vanadium. *Topics in Catalysis* **2002**, 20, (1-4), 75-83.
  19. Lee, D. Y.; Lee, W. J.; Song, J. S.; Koh, J. H.; Kim, Y. S., Electronic surface state of TiO<sub>2</sub> electrode doped with transition metals, studied with cluster model and DV-X alpha method. *Computational Materials Science* **2004**, 30, (3-4), 383-388.
  20. Thompson, T. L.; Yates, J. T., TiO<sub>2</sub>-based photocatalysis: Surface defects, oxygen and charge transfer. *Topics in Catalysis* **2005**, 35, (3-4), 197-210.
  21. Chang, S. M.; Hou, C. Y.; Lo, P. H.; Chang, C. T., Preparation of phosphated Zr-doped TiO<sub>2</sub> exhibiting high photocatalytic activity through calcination of ligand-capped nanocrystals. *Applied Catalysis B-Environmental* **2009**, 90, (1-2), 233-241.
  22. Fujishima, A.; Honda, K., Electrochemical photolysis of water at a semiconductor electrode. *Nature* **1972**, 238, (5358), 37-38.
  23. Sclafani, A.; Herrmann, J. M., Comparison of the photoelectronic and photocatalytic activities of various anatase and rutile forms of titania in pure liquid organic phases and in aqueous solutions. *Journal of Physical Chemistry* **1996**, 100, (32), 13655-13661.
  24. Augustynski, J., Comment on "Diffusion impedance and space charge capacitance in the nanoporous dye-sensitized electrochemical solar cell" and "Electronic transport in dye-sensitized nanoporous TiO<sub>2</sub> solar cells-comparison of electrolyte and solid-state devices". *Journal of Physical Chemistry B* **2003**, 107, (48), 13544-13545.



25. Skubal, L. R.; Meshkov, N. K.; Vogt, M. C., Detection and identification of gaseous organics using a TiO<sub>2</sub> sensor. *Journal of Photochemistry and Photobiology a-Chemistry* **2002**, 148, (1-3), 103-108.
26. Hoffmann, M. R.; Martin, S. T.; Choi, W. Y.; Bahnemann, D. W., Environmental Applications of Semiconductor Photocatalysis. *Chemical Reviews* **1995**, 95, (1), 69-96.
27. Asahi, R.; Taga, Y.; Mannstadt, W.; Freeman, A. J., Electronic and optical properties of anatase TiO<sub>2</sub>. *Physical Review B* **2000**, 61, (11), 7459-7465.
28. Matthews, R. W., PHOTOOXIDATION OF ORGANIC IMPURITIES IN WATER USING THIN-FILMS OF TITANIUM-DIOXIDE. *Journal of Physical Chemistry* **1987**, 91, (12), 3328-3333.
29. Choi, W. Y.; Termin, A.; Hoffmann, M. R., The Role of Metal-Ion Dopants in Quantum-Sized TiO<sub>2</sub> - Correlation between Photoreactivity and Charge-Carrier Recombination Dynamics. *Journal of Physical Chemistry* **1994**, 98, (51), 13669-13679.
30. Litter, M. I., Heterogeneous photocatalysis - Transition metal ions in photocatalytic systems. *Applied Catalysis B-Environmental* **1999**, 23, (2-3), 89-114.
31. Diebold, U., The surface science of titanium dioxide. *Surface Science Reports* **2003**, 48, 53-229.
32. Weckhuysen, B. M.; Keller, D. E., Chemistry, spectroscopy and the role of supported vanadium oxides in heterogeneous catalysis. *Catalysis Today* **2003**, 78, (1-4), 25-46.
33. Zhang, H. Z.; Banfield, J. F., Understanding polymorphic phase transformation behavior during growth of nanocrystalline aggregates: Insights from TiO<sub>2</sub>. *Journal of Physical Chemistry B* **2000**, 104, (15), 3481-3487.
34. Riegel, G.; Bolton, J. R., Photocatalytic Efficiency Variability in TiO<sub>2</sub> Particles. *Journal of Physical Chemistry* **1995**, 99, (12), 4215-4224.
35. Sze, S. M., *Semiconductor Devices - physics and technology*. 2002.
36. Serpone, N., Relative photonic efficiencies and quantum yields in heterogeneous photocatalysis. *Journal of Photochemistry and Photobiology a-Chemistry* **1997**, 104, (1-3), 1-12.
37. Hurum, D. C.; Gray, K. A.; Rajh, T.; Thurnauer, M. C., Recombination pathways in the Degussa P25 formulation of TiO<sub>2</sub>: Surface versus lattice mechanisms. *Journal of Physical Chemistry B* **2005**, 109, (2), 977-980.
38. Lawless, D.; Serpone, N.; Meisel, D., Role of Oh. Radicals and Trapped Holes in Photocatalysis - a Pulse-Radiolysis Study. *Journal of Physical Chemistry* **1991**, 95, (13), 5166-5170.

39. Kabra, K.; Chaudhary, R.; Sawhney, R. L., Treatment of hazardous organic and inorganic compounds through aqueous-phase photocatalysis: A review. *Industrial & Engineering Chemistry Research* **2004**, 43, (24), 7683-7696.
40. Wu, T. X.; Liu, G. M.; Zhao, J. C.; Hidaka, H.; Serpone, N., Photoassisted degradation of dye pollutants. V. Self-photosensitized oxidative transformation of Rhodamine B under visible light irradiation in aqueous TiO<sub>2</sub> dispersions. *Journal of Physical Chemistry B* **1998**, 102, (30), 5845-5851.
41. Cushing, B. L.; Kolesnichenko, V. L.; O'Connor, C. J., Recent advances in the liquid-phase syntheses of inorganic nanoparticles. *Chemical Reviews* **2004**, 104, (9), 3893-3946.
42. The Sol-Gel Process <http://optoweb.fis.uniroma2.it/opto/solgel/index.html>.
43. Hench, L. L.; West, J. K., The Sol-Gel Process. *Chemical Reviews* **1990**, 90, (1), 33-72.
44. Brinker, C. J.; Scherer, G. W., *Sol-gel science*. Academic Press: 1990.
45. Bischoff, B. L.; Anderson, M. A., Peptization Process in the Sol-Gel Preparation of Porous Anatase (TiO<sub>2</sub>). *Chemistry of Materials* **1995**, 7, (10), 1772-1778.
46. Wang, C. C.; Ying, J. Y., Sol-gel synthesis and hydrothermal processing of anatase and rutile titania nanocrystals. *Chemistry of Materials* **1999**, 11, (11), 3113-3120.
47. Sadasivan, S.; Dubey, A. K.; Li, Y. Z.; Rasmussen, D. H., Alcoholic solvent effect on silica synthesis - NMR and DLS investigation. *Journal of Sol-Gel Science and Technology* **1998**, 12, (1), 5-14.
48. Sato, H.; Norisuye, T.; Takemori, T.; Tran-Cong-Miyata, Q.; Nomura, S., Effects of solvent on microstructure and proton conductivity of organic-inorganic hybrid membranes. *Polymer* **2007**, 48, (19), 5681-5687.
49. Ichinose, I.; Senzu, H.; Kunitake, T., A surface sol-gel process of TiO<sub>2</sub> and other metal oxide films with molecular precision. *Chemistry of Materials* **1997**, 9, (6), 1296-&.
50. Choi, W. Y.; Termin, A.; Hoffmann, M. R., Effects of Metal-Ion Dopants on the Photocatalytic Reactivity of Quantum-Sized TiO<sub>2</sub> Particles. *Angewandte Chemie-International Edition in English* **1994**, 33, (10), 1091-1092.
51. Alyea, E. C.; Lakshmi, L. J.; Ju, Z., Spectroscopic and activity studies on vanadia supported on titania and phosphorus-modified titania. *Langmuir* **1997**, 13, (21), 5621-5626.
52. Bulushev, D. A.; Kiwi-Minsker, L.; Zaikovskii, V. I.; Renken, A., Formation of active sites for selective toluene oxidation during catalyst synthesis via solid-state reaction of V<sub>2</sub>O<sub>5</sub> with TiO<sub>2</sub>. *Journal of Catalysis* **2000**, 193, (1), 145-153.
53. Rodella, C. B.; Nascente, P. A. P.; Mastelaro, V. R.; Zucchi, M. R.; Franco, R. W. A.;

- Magon, C. J.; Donoso, P.; Florentino, A. O., Chemical and structural characterization of V<sub>2</sub>O<sub>5</sub>/TiO<sub>2</sub> catalysts. *Journal of Vacuum Science & Technology A* **2001**, 19, (4), 1158-1163.
54. Calatayud, M.; Minot, C., Reactivity of the oxygen sites in the V<sub>2</sub>O<sub>5</sub>/TiO<sub>2</sub> anatase catalyst. *Journal of Physical Chemistry B* **2004**, 108, (40), 15679-15685.
55. Izumi, Y.; Kiyotaki, F.; Yagi, N.; Vlaicu, A. M.; Nisawa, A.; Fukushima, S.; Yoshitake, H.; Iwasawa, Y., X-ray absorption fine structure combined with X-ray fluorescence spectrometry. Part 15. Monitoring of vanadium site transformations on Titania and in mesoporous titania by selective detection of the vanadium K alpha(1) fluorescence. *Journal of Physical Chemistry B* **2005**, 109, (31), 14884-14891.
56. Sorantin, P. I.; Schwarz, K., Chemical Bonding in Rutile-Type Compounds. *Inorganic Chemistry* **1992**, 31, (4), 567-576.
57. Gratzel, M.; Howe, R. F., Electron-Paramagnetic Resonance Studies of Doped TiO<sub>2</sub> Colloids. *Journal of Physical Chemistry* **1990**, 94, (6), 2566-2572.
58. Davidson, A.; Che, M., Temperature-Induced Diffusion of Probe Vanadium(IV) Ions into the Matrix of Titanium-Dioxide as Investigated by ESR Techniques. *Journal of Physical Chemistry* **1992**, 96, (24), 9909-9915.
59. Zhao, G. L.; Han, G. R.; Takahashi, M.; Yoko, T., Photoelectrochemical properties of sol-gel-derived Ti<sub>1-x</sub>V<sub>x</sub>O<sub>2</sub> solid solution film photoelectrodes. *Thin Solid Films* **2002**, 410, (1-2), 14-20.
60. Butler, T. M.; MacCraith, B. D.; McDonagh, C., Leaching in sol-gel-derived silica films for optical pH sensing. *Journal of Non-Crystalline Solids* **1998**, 224, (3), 249-258.
61. Berger, T.; Lana-Villarreal, T.; Monllor-Satoca, D.; Gomez, R., Charge transfer reductive doping of nanostructured TiO<sub>2</sub> thin film's as a way to improve their photoelectrocatalytic performance. *Electrochemistry Communications* **2006**, 8, (11), 1713-1718.
62. Wilson, R. G.; Stevie, F. A.; Magee, C. W., *Secondary Ion Mass Spectrometry - A Proactical Handbook for Depth Profiling and Bulk Impurity Analysis* New York, 1989.
63. Uvarov, V.; Popov, I., Metrological characterization of X-ray diffraction methods for determination of crystallite size in nano-scale materials. *Materials Characterization* **2007**, 58, (10), 883-891.
64. Lacombe, S.; Cardy, H.; Soggiu, N.; Blanc, S.; Habib-Jiwan, J. L.; Soumillion, J. P., Diffuse reflectance UV-Visible spectroscopy for the qualitative and quantitative study of chromophores adsorbed or grafted on silica. *Microporous and Mesoporous Materials* **2001**, 46, (2-3), 311-325.
65. 力丞儀器科技有限公司 <http://www.apisc.com/index.htm>.

66. Wachs, I. E.; Jehng, J. M.; Ueda, W., Determination of the chemical nature of active surface sites present on bulk mixed metal oxide catalysts. *Journal of Physical Chemistry B* **2005**, 109, (6), 2275-2284.
67. Reed-Hill, R. E. a., *Physical metallurgy principle*. third ed.; 1991.
68. Trifiro, F., The chemistry of oxidation catalysts based on mixed oxides. *Catalysis Today* **1998**, 41, (1-3), 21-35.
69. Bhattacharyya, K.; Varma, S.; Tripathi, A. K.; Bharadwaj, S. R.; Tyagi, A. K., Effect of Vanadia Doping and Its Oxidation State on the Photocatalytic Activity of TiO<sub>2</sub> for Gas-Phase Oxidation of Ethene. *Journal of Physical Chemistry C* **2008**, 112, (48), 19102-19112.
70. Udompom, A.; Ananta, S., Effect of calcination condition on phase formation and particle size of lead titanate powders synthesized by the solid-state reaction. *Materials Letters* **2004**, 58, (7-8), 1154-1159.
71. Zhao, G. L.; Kozuka, H.; Lin, H.; Yoko, T., Sol-gel preparation of Ti<sub>1-x</sub>V<sub>x</sub>O<sub>2</sub> solid solution film electrodes with conspicuous photoresponse in the visible region. *Thin Solid Films* **1999**, 339, (1-2), 123-128.
72. Zhao, C.; Zhong, S. H., Structures and photo absorption properties of sol-gel-derived coupled semiconductor V<sub>2</sub>O<sub>5</sub>-TiO<sub>2</sub>. *Chinese Journal of Inorganic Chemistry* **2006**, 22, (2), 238-242.
73. Chang, S. M.; Doong, R. A., Characterization of Zr-doped TiO<sub>2</sub> nanocrystals prepared by a nonhydrolytic sol-gel method at high temperatures. *Journal of Physical Chemistry B* **2006**, 110, (42), 20808-20814.
74. Luan, Z. H.; Kevan, L., Electron spin resonance and diffuse reflectance ultraviolet-visible spectroscopies of vanadium immobilized at surface titanium centers of titanosilicate mesoporous TiMCM-41 molecular sieves. *Journal of Physical Chemistry B* **1997**, 101, (11), 2020-2027.
75. Zheng, S.; Gao, L.; Zhang, Q. H.; Zhang, W. P.; Guo, J. K., Preparation, characterization and photocatalytic properties of singly and doubly titania-modified mesoporous silicate MCM-41 by varying titanium precursors. *Journal of Materials Chemistry* **2001**, 11, (2), 578-583.
76. Busca, G.; Centi, G.; Marchetti, L.; Trifiro, F., CHEMICAL AND SPECTROSCOPIC STUDY OF THE NATURE OF A VANADIUM-OXIDE MONOLAYER SUPPORTED ON A HIGH-SURFACE-AREA TiO<sub>2</sub> ANATASE. *Langmuir* **1986**, 2, (5), 568-577.
77. Centi, G., Nature of active layer in vanadium oxide supported on titanium oxide and control of its reactivity in the selective oxidation and ammoxidation of alkylaromatics.

*Applied Catalysis a-General* **1996**, 147, (2), 267-298.

78. Serpone, N.; Lawless, D.; Disdier, J.; Herrmann, J. M., Spectroscopic, Photoconductivity, and Photocatalytic Studies of TiO<sub>2</sub> Colloids - Naked and with the Lattice Doped with Cr<sup>3+</sup>, Fe<sup>3+</sup>, and V<sup>5+</sup> Cations. *Langmuir* **1994**, 10, (3), 643-652.

79. Osorio-Guillen, J.; Lany, S.; Zunger, A., Atomic control of conductivity versus ferromagnetism in wide-gap oxides via selective doping: V, Nb, Ta in anatase TiO<sub>2</sub>. *Physical Review Letters* **2008**, 100, (3), -.

80. Wang, C. T.; Huang, H. H., Photo-chargeable titanium/vanadium oxide composites. *Journal of Non-Crystalline Solids* **2008**, 354, (28), 3336-3342.

81. Coronado, J. M.; Maira, A. J.; Conesa, J. C.; Yeung, K. L.; Augugliaro, V.; Soria, J., EPR study of the surface characteristics of nanostructured TiO<sub>2</sub> under UV irradiation. *Langmuir* **2001**, 17, (17), 5368-5374.

82. Coronado, J. M.; Maira, A. J.; Martinez-Arias, A.; Conesa, J. C.; Soria, J., EPR study of the radicals formed upon UV irradiation of ceria-based photocatalysts. *Journal of Photochemistry and Photobiology a-Chemistry* **2002**, 150, (1-3), 213-221.

83. 高濂, 鄭., 張青虹, 奈米光觸媒 *Nano-photocatalyst*. 五南圖書出版股份有限公司: 台灣, 2004.

84. Kaoua, S.; Krimi, S.; El Jazouli, A.; Hlil, E. K.; de Waal, D., Preparation and characterization of phosphate glasses containing titanium and vanadium. *Journal of Alloys and Compounds* **2007**, 429, (1-2), 276-279.

85. Nakaoka, Y.; Nosaka, Y., ESR Investigation into the effects of heat treatment and crystal structure on radicals produced over irradiated TiO<sub>2</sub> powder. *Journal of Photochemistry and Photobiology a-Chemistry* **1997**, 110, (3), 299-305.

86. Howe, R. F.; Gratzel, M., EPR Study of Hydrated Anatase under UV Irradiation. *Journal of physical chemistry* **1987**, 91, (14), 3906-3909.

87. Micic, O. I.; Zhang, Y. N.; Cromack, K. R.; Trifunac, A. D.; Thurnauer, M. C., Trapped Holes on TiO<sub>2</sub> Colloids Studied by Electron-Paramagnetic-Resonance. *Journal of physical chemistry* **1993**, 97, (28), 7277-7283.

88. Depero, L. E.; Bonzi, P.; Musci, M.; Casale, C., Microstructural Study of Vanadium-Titanium Oxide Powders Obtained by Laser-Induced Synthesis. *Journal of Solid State Chemistry* **1994**, 111, (2), 247-252.

89. Sroiraya, S.; Triampo, W.; Morales, N. P.; Triampo, D., Kinetics and mechanism of hydroxyl radical formation studied via electron spin resonance for photocatalytic

nanocrystalline titania: Effect of particle size distribution, concentration, and agglomeration. *Journal of Ceramic Processing Research* **2008**, 9, (2), 146-154.

90. 鄭信民, 李., X 光繞射應用介紹. *工業材料雜誌* **2002**, 181, 100-108.

91. 張 銀 祐 X 光 繞 射 與 薄 膜 殘 留 應 力 分 析  
<http://el.mdu.edu.tw/datacos//09623111018A/%E6%9D%90%E6%96%99%E5%88%86%E6%9E%90%20CH4%20XRD-X%E5%85%89%E7%B9%9E%E5%B0%84.pdf>.

92. Ray, W. J.; Post, C. B., The Oxyvanadium Constellation in Transition-State-Analog Complexes of Phosphoglucomutase and Ribonuclease - Structural Deductions from Electron-Transfer Spectra. *Biochemistry* **1990**, 29, (11), 2779-2789.

93. Gao, X. T.; Bare, S. R.; Weckhuysen, B. M.; Wachs, I. E., In situ spectroscopic investigation of molecular structures of highly dispersed vanadium oxide on silica under various conditions. *Journal of Physical Chemistry B* **1998**, 102, (52), 10842-10852.

94. Gao, X. T.; Wachs, I. E., Investigation of surface structures of supported vanadium oxide catalysts by UV-vis-NIR diffuse reflectance spectroscopy. *Journal of Physical Chemistry B* **2000**, 104, (6), 1261-1268.

95. The phase control in EPR. <http://www.kyospin.com/KSPhaseControl.htm>.

96. Akira Fujishima; Tata N. Rao; Tryk, D. A., Titanium dioxide photocatalysis. *Journal of Photochemistry and Photobiology C-Photochemistry Reviews* **2000**, 1, 1-21.

97. Herrmann, J. M., Heterogeneous photocatalysis: fundamentals and applications to the removal of various types of aqueous pollutants. *Catalysis Today* **1999**, 53, (1), 115-129.

98. Kumar, K. V.; Porkodi, K.; Rocha, F., Langmuir-Hinshelwood kinetics - A theoretical study. *Catalysis Communications* **2008**, 9, (1), 82-84.

## Appendix A Experimental parameters

Appendix A-1 Operational parameter of XPS.

Mode	Binding energy	Pass energy	Anode	Step size	Time/steps
Survey	1200-0 eV	23.5 eV	Al	1.0 eV	50 ms
Multiplex	Depending on element	23.5 eV	Al	0.1 eV	50 ms

Appendix A-2 Detail operational of XPS in multiplex.

Element	Pass Energy	Step size	Scan times	BE range	ASF
O 1s	23.5 eV	0.1 eV	20	529.3-531.2	0.711
Ti 2p	23.5 eV	0.1 eV	20	458.2	2.001
V 2p	23.5 eV	0.1 eV	80	517.6	2.116

Appendix A-3 Relative sensitivity factor of SIMS.

Sample name	Impurity density, $\rho_i$ (atoms/cm <sup>2</sup> )	Matrix secondary ions intensity, $I_i$	Impurity secondary ions intensity, $I_m$	Relative sensitivity factor (RSF)
V (Impurity)				
Ti (Matrix)				
VT $7 \times 10^{-1}$	1.74E+18	93785	107849	$1.51 \times 10^{18}$
VT $1 \times 10^{-4}$	2.49E+14	276246	93	$7.40 \times 10^{17}$

Appendix A-4 Raw data of SIMS.

Sample name	Vanadium (m/z)	Impurity (V) secondary ions intensity, $I_m$	Titanium (m/z)	Matrix (Ti) secondary ions intensity, $I_i$	Impurity density, $\rho_i$ (atoms/cm <sup>2</sup> )
VT 4.4E-5	50.68	41	47.97	399106	$1.55 \times 10^{14}$
VT 1.3E-4	50.83	305	47.97	320761	$1.44 \times 10^{15}$
VT 5.1E-4	50.86	368	47.93	587123	$9.48 \times 10^{14}$
VT 1.3E-3	50.99	1979	47.94	759273	$3.94 \times 10^{15}$
VT 1.2E-2	50.90	16152	47.93	683923	$3.57 \times 10^{16}$
SVT 1.7E-3	50.96	9009	47.97	414003	$3.29 \times 10^{16}$
SVT 3.5E-3	51.04	1616	47.87	8317	$2.94 \times 10^{17}$
SVT 6.4E-3	50.73	3582	47.87	12480	$4.34 \times 10^{17}$
SVT 1.1E-2	50.89	8022	47.81	19117	$6.35 \times 10^{17}$

Appendix A-5 Operational parameter of XRPD.

Scan range	Sampling width (degree)	Scan speed (degree/min)	Measurement type	Voltage (KV)	Current (mA)
10-80 degree	0.02	4.0	Ordinary  (without background)	30.0	20.0

Appendix A-6 Operational parameter of UV-vis.

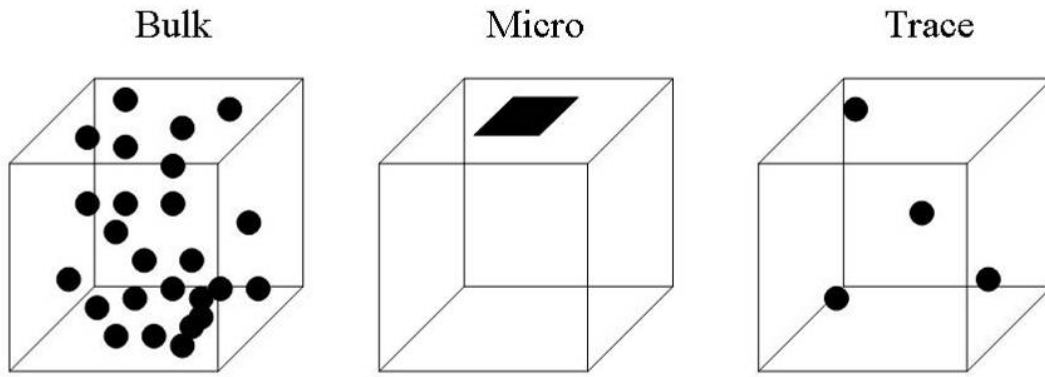
Measurement	Data Mode	Starting wavelength	Ending wavelength	Sampling interval	Slit width	Reference
Wavelength	% R	900 nm	200 nm	1 nm	1 nm	Al <sub>2</sub> O <sub>3</sub>



## Appendix B Instrument principle

### Appendix B-1 Time-of-Flight Secondary Ion Mass Spectrometer

SIMS is an analytical technique that can be used to characterize the surface and near surface ( $\sim 30 \mu\text{m}$ ) region of solid. The technique uses a beam of energetic (0.5-20 keV) primary ions to sputter the sample surface, producing ionized secondary particles that are detected using a mass spectrometer. Besides, the detection limit for element is ppb  $\sim$  ppm, where is more sensitive than AES (0.1 %) or ESCA (0.01 %). And for chemical analysis, SIMS can detect bulk, micro and trace of sample which is shown in Appendix B-1.<sup>62, 90</sup>



Appendix B-1 Chemical analysis for three different types of sample.<sup>90</sup>

SIMS measurements were performed with a TOF-SIMS IV (ION-TOF) spectrometer which use a  $\text{Ga}^+$  or  $\text{Au}^+$  to be analytic source and use an  $\text{O}_2^+$  or  $\text{Cs}^+$  to be sputter source. The thickness of sample is around 1 cm and area of sample is around  $1 \text{ cm}^2$ . The detection area is  $100 \times 100 \mu\text{m}^2$ . The sputter time is 120 seconds. The surface atomic ratio was calculated from the intensity of secondary ions which are normalized to relative sensitivity factor. A relative sensitivity factor (RSF) is a conversion factor from secondary ion intensity to atom density. The RSF is defined by sub-equation:<sup>62</sup>

$$\rho_i = \frac{I_i}{I_m} RSF \quad (\text{B-1})$$

Where  $\rho_i$  is the impurity atom density in  $\text{atoms/cm}^3$ ,  $I_i$  is the impurity isotope secondary ion intensity in counts/s,  $I_m$  is the matrix isotope secondary ion intensity in counts/s, and  $RSF$

has unit of atoms/cm<sup>3</sup>.

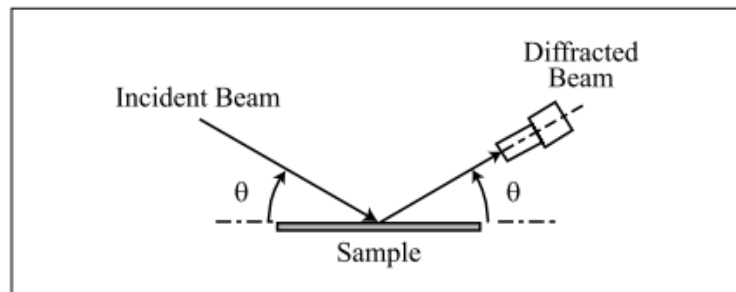
The surface atomic ratio can be calculated by sub-equation

$$\frac{n_1}{n_2} = \frac{I_1 / RSF_1}{I_2 / RSF_2} \quad (\text{B-2})$$

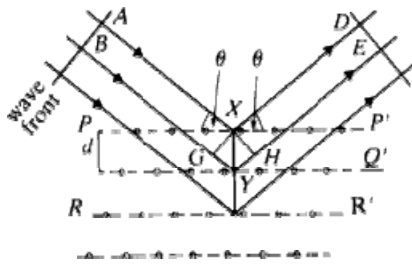
Where  $n$  denotes the atomic numbers,  $I$  is the intensity of secondary ions on SIMS spectra,  $RSF$  stands for the atomic relative sensitive factor of element.

## Appendix B-2 X-ray powder diffractometry (XRPD)

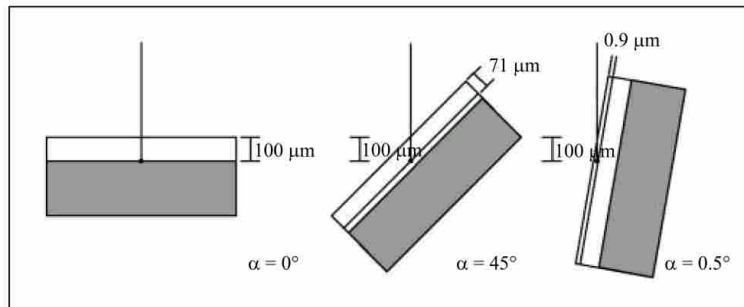
The bulk crystal structure of bulk materials were detected by Bragg's law. The device of XRPD is shown in Appendix B-2. And the principle of XRD is Bragg's law, which calculated the d-spacing of the crystal structure, as shown in Appendix B-3. But the thickness of X-ray detective limit is positive with  $\sin \alpha / \mu$  ( $\alpha$  is incidence angle and  $\mu$  is adsorption constant of materials). Therefore, the thickness of XRPD detection is around 10~100  $\mu\text{m}$  ( $1/\mu$ ). But the thickness of thin film is quite lower than limit of XRPD, even several hundred  $\text{\AA}$ . Moreover, while the thin film is detected by XRPD, the signal of sample would be cover by matrix. So, grazing incident diffraction, GID, method could vary the thickness of detection by change the incidence angle. Appendix B-4 shows the relationship between incidence angle and detective thickness. And Appendix B-5 shows the concept of GI-XRD.



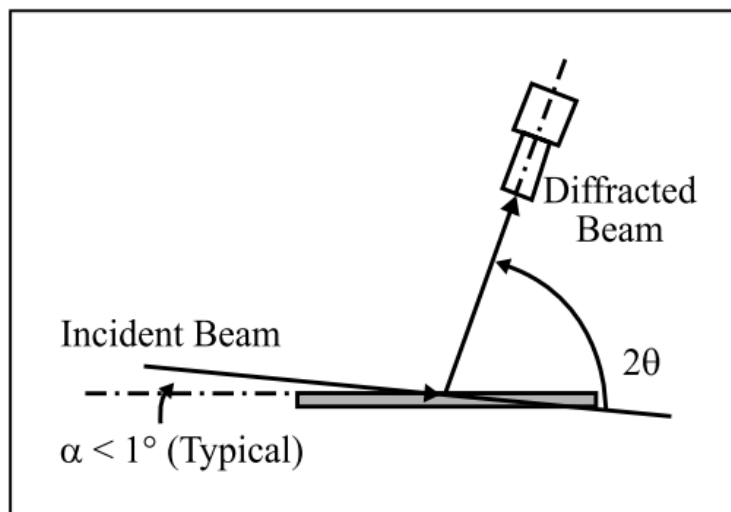
Appendix B-2 The concept of x-ray powder diffractometry device.<sup>90</sup>



Appendix B-3 The concept of geometric figure for Bragg's law.<sup>91</sup>



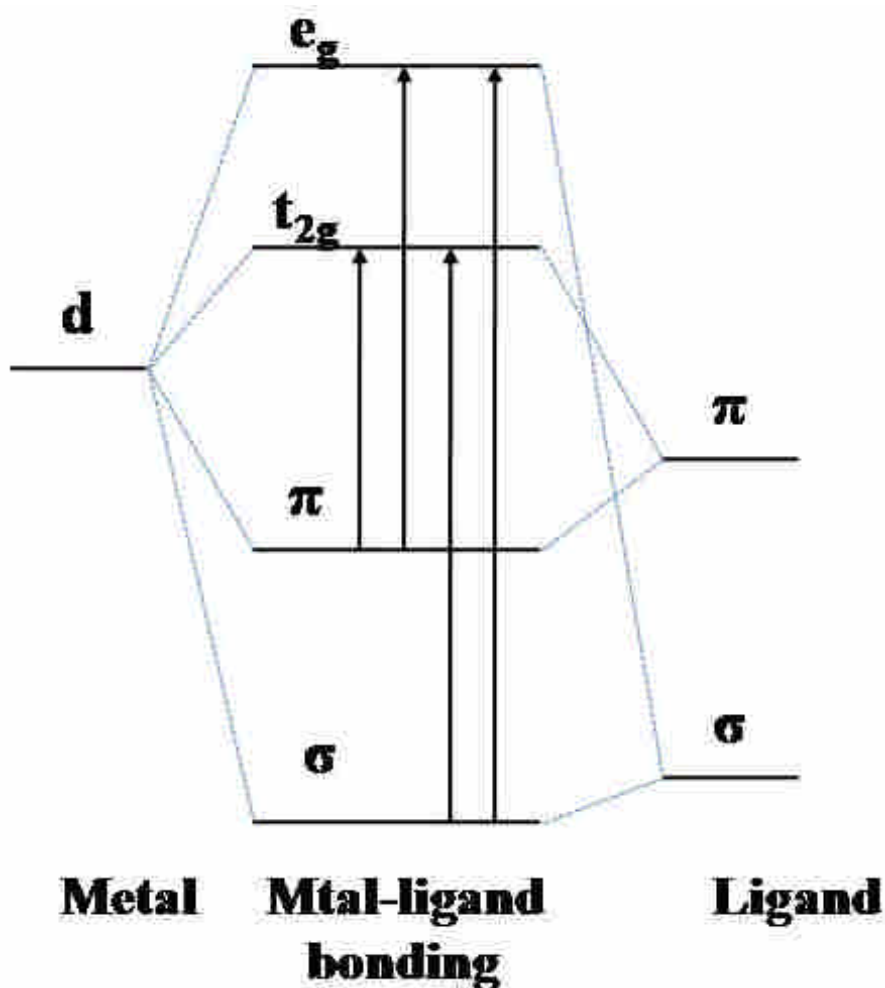
Appendix B-4 The relationship between incidence angle and detective thickness for GI-XRD.<sup>90</sup>



Appendix B-5 The concept of grazing incident x-ray powder diffractometry device.<sup>90</sup>

### Appendix B-3 UV-vis diffuse reflectance spectroscopy (DRS)

UV-vis diffuse reflectance spectroscopy (DRS) was applied to study the bonding information for inorganic compounds. And the local structures of the vanadium ions in  $\text{TiO}_2$  are often associated with the band positions of the ligand<sup>1</sup>-to-metal charge transfer (LMCT) transition from an  $\text{O}^{2-}$  ion  $t_{1u}$  orbital to a  $\text{M}^{n+}$  metal  $e_g$  orbital.<sup>76, 92-94</sup> In order to elucidate the optical properties for photocatalysts, UV-visible spectroscopy was used to examine the optical reflectance of the bulk and surface doping materials at different vanadium ions concentration. Thus, Appendix B-6 is shown the ligand-to-metal charge transfer (LMCT) transition for  $\text{TiO}_2$ .

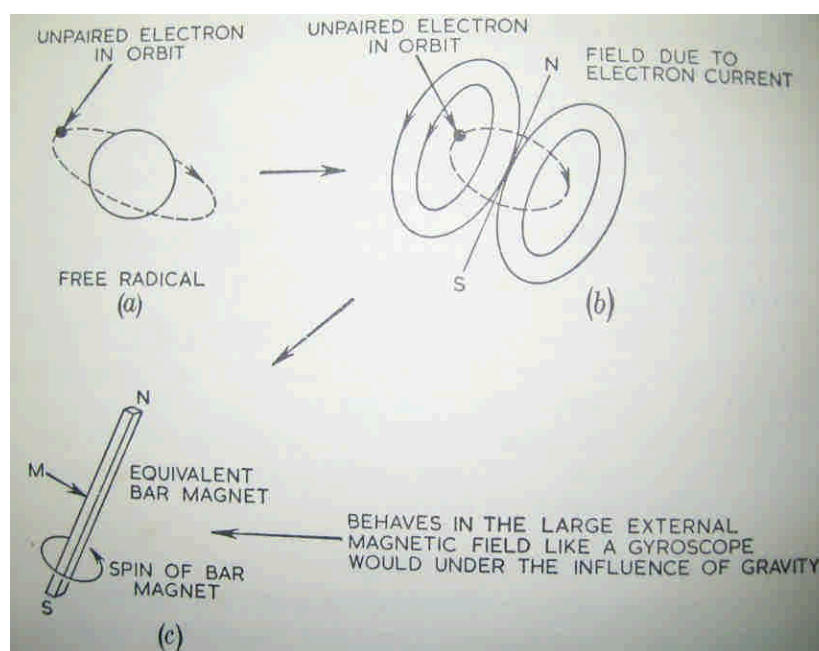


Appendix B-6 A simplified molecular orbital diagram illustrating the potential ligand to metal charge transfer transitions.<sup>5, 67</sup>

<sup>1</sup> In chemistry, a ligand is either an atom, ion, or molecule that bonds to a central metal to produce a coordination complex. The bonding between the metal and ligand generally involving formal donation of one or more of the ligand's electrons. The metal-ligand bonding ranges from covalent to more ionic. Furthermore, the metal-ligand bond order can range from one to three. <http://en.wikipedia.org/wiki/Ligand>

## Appendix B-4 Electron paramagnetic resonance (EPR)

An unpaired electron which is rotating around the rest of the molecule is equivalent to a current flowing in a complete turn of wire without resistance, and thus it produces a magnetic field which passes through its centre as shown in Appendix B-7. In the other word, the electron is circling around the molecule it acts rather like a gyroscope, with the same reluctance to change the direction of its axis of spin. If a quantity of these free radicals is placed in strong unidirectional and constant value magnetic field,  $H$ , some of the bar magnets will take up a position relative to the d.c. field as shown in Appendix B-8.<sup>35</sup>

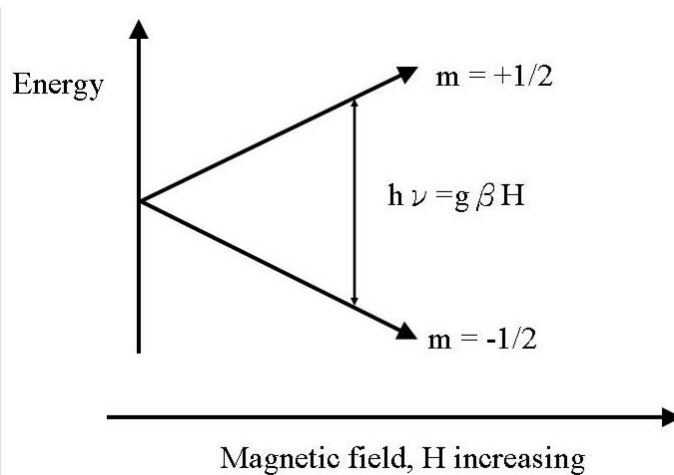


Appendix B-7 How a free radical acts a bar magnet with mass.<sup>35</sup>

Such EPR spectra (Appendix B-8) are obtained by measuring the attenuation versus frequency (or wavelength) of a beam of electromagnetic radiation as it passes through a sample of matter. Transition can be induced between there levels by applying an oscillating magnetic field of frequency at right angles to the d.c. field. The relation between field and frequency for resonance of the free electron is

$$\nu = (g\beta / h)H \quad (\text{B-3})$$

where  $g$  is  $g$  factor,  $\beta$  is Bohr magneton,  $H$  is magnetic field and  $h$  is Planck constant.

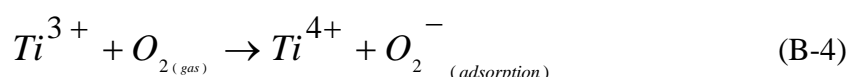


Appendix B-8 Energy-level scheme for the sample (e.g. free electron) as a function of applied magnetic field.<sup>83</sup>

However, the transition elements are present for which shells inside the valence shell are not filled, so that unpaired electrons are always present. For example, the first transition group is the iron group in which the electrons start filling the 3d shell after the 4s valence electrons have filled. For free electron  $g$  factor has the value 2.0023. In most free radicals  $g$  lies very close to this value, where in the range 2.002 to 2.004.<sup>35</sup>

EPR spectra of V-doped anatase are as expected for  $V^{4+}$  ( $S=1/2$ ,  $I=7/2$ ) being composed of essentially two or three groups of octets due to the coupling of a single electron with the vanadium nucleus. However, the  $Ti^{3+}$  and  $\bullet OH$  would not appear after UV irradiation, because the  $Ti^{3+}$  ions would easily oxidize to  $Ti^{4+}$  and the electron would transfer to  $O_2$  which is adsorbed on the surface of  $TiO_2$  (equation B-4). Moreover, oxygen was chemically adsorbed by  $O_2^{2-}$  ion in room to low temperature process. Besides,  $O_2^{2-}$  simultaneously have hole-reduction agent and electron consumed agent function, and  $O_2^-$  be the product by hole/electron consumed reaction. That is why  $O_2^-$  signal can be detected in EPR system after UV irradiation with low vanadium concentration.<sup>83</sup>

The reaction between  $Ti^{3+}$  and oxygen:



The reaction between excited electron or hole and oxygen gas or ion :

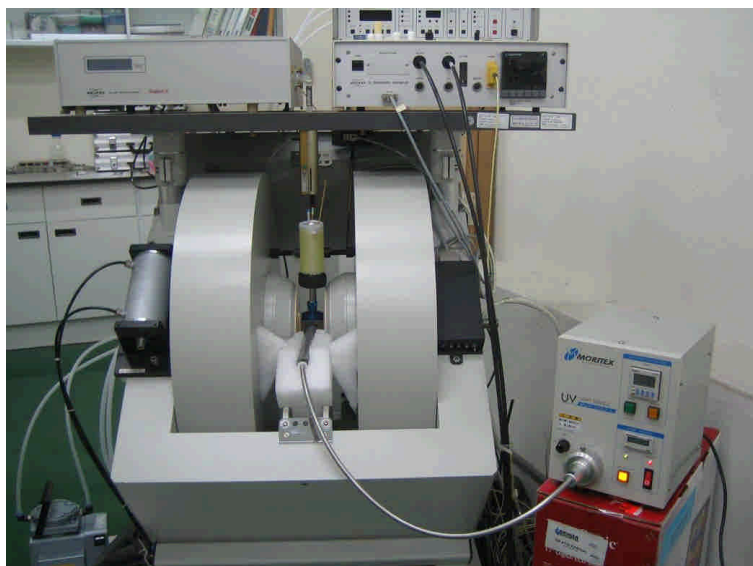


The reaction between excited electron or hole and water :

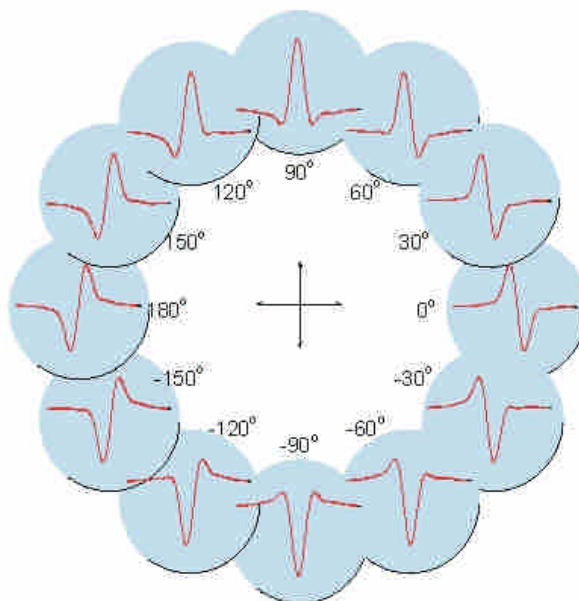


The EPR spectra recorded at 77 K of all samples. Each sample contains 0.01 g powder which is filled in quartz tube in the dark or under UV light. Furthermore, the wavelength of UV light system (Moritex, MUV-250U-L) is 365 nm mainly and 150W. And the photograph of EPR instrument is presented in Appendix B-9. The temperature is control by He (3.8K to 300K) or N<sub>2</sub> (100 to 500k). The microwave frequency is 9.490 GHz, and its power is 8.012 mW. In addition, the range of magnetic field center is 3400 G where the sweep width and sweep time is 600 G and 167 second separately. And the resolution is 2048 point. Beside, the phase is 0.0 deg, which is shown in Appendix B-10. The electromagnet size is 10 inches and the length between is 72 mm.

However, in order to understand the diffusion of interface generated-electron/hole, the concentration of hydroxyl radicals which were generated on the surface of materials were detected by ESR. The signal of radicals spin-trapped with 5,5-dimethyl-1-pyrroline N-oxide (DMPO, Aldrich) were detected by ESR, as shown in Appendix B-11. The 1 mL of 0.03 M DMPO solution was injected in 10 mL DI water that dissolve 10 mg samples. EPR samples were analyzed at 77 K with UV irradiation after 30 min O<sub>2</sub> aeration.

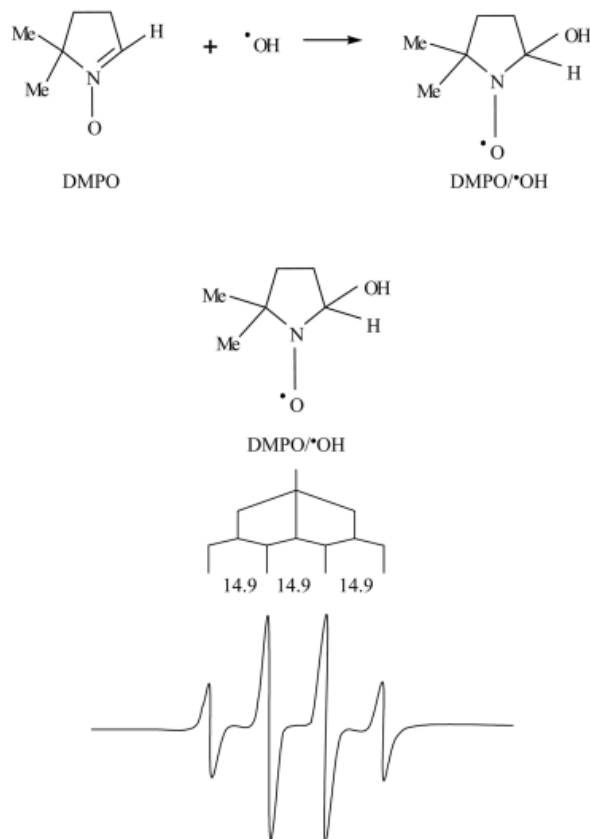


Appendix B-9 The photograph of EPR instrument.



Appendix B-10 The EPR phase control with different angle.<sup>95</sup>





Appendix B- 11 The spectrum of spin trap of  $\cdot\text{OH}$  radical with DMPO. And hyperfine splitting of DMPO/ $\cdot\text{OH}$  ESR signal is 14.9 Gauss. This is characteristic of a DMPO adduct (1 : 2 : 2 : 1 quartet with hyperfine coupling of  $a_N = a_H = 14.9$  Gauss) produced by spin trapping of a hydroxyl radical produced in a hydroxyl radical-generating system.<sup>89</sup>

## Appendix C BET Data

Appendix C-1 The specific surface area of bulk doping materials.

Bulk doped materials					
Sample	VT	VT	VT	VT	VT
	$4.41 \times 10^{-5}$	$1.34 \times 10^{-4}$	$5.09 \times 10^{-4}$	$1.27 \times 10^{-3}$	$1.22 \times 10^{-2}$
$S_{\text{BET}}$ ( $\text{m}^2/\text{g}$ )	102	103	105	104	110

Appendix C-2 The specific surface area of all of surface doping materials.

Surface doped materials					
Sample	$\text{TiO}_2$	SVT	SVT	SVT	SVT
		$1.73 \times 10^{-3}$	$3.47 \times 10^{-3}$	$6.40 \times 10^{-3}$	$1.10 \times 10^{-2}$
$S_{\text{BET}}$ , ( $\text{m}^2/\text{g}$ )	$99 \pm 2$	107	105	105	99

Appendix C-3 The specific surface area of all of surface doping material with pure vanadium ions.

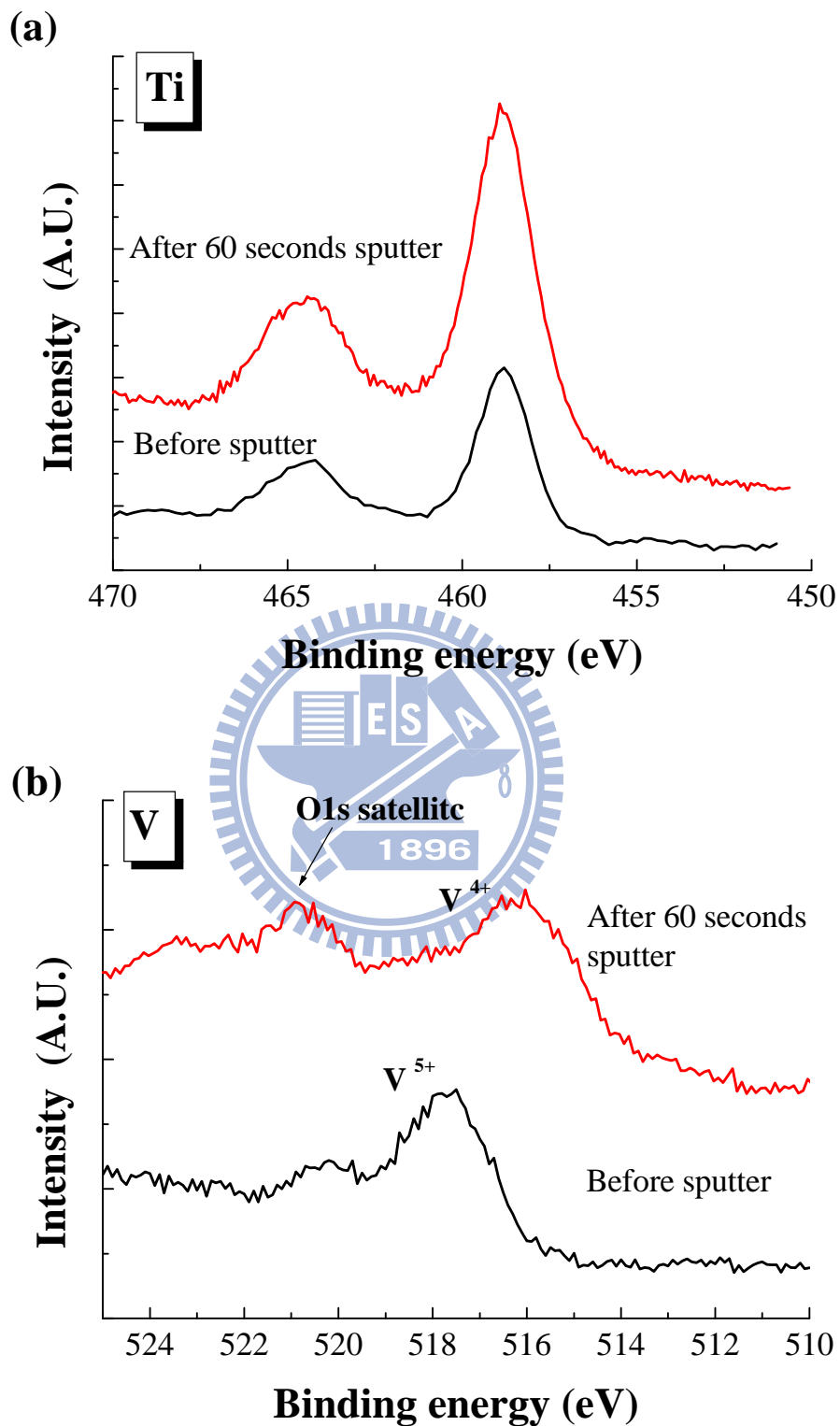
Surface doping materials		
Sample	$\text{TiO}_2$	SVTP $4.74 \times 10^{-3}$
$S_{\text{BET}}$ , ( $\text{m}^2/\text{g}$ )	$99 \pm 2$	103

## Appendix D. ESCA analysis

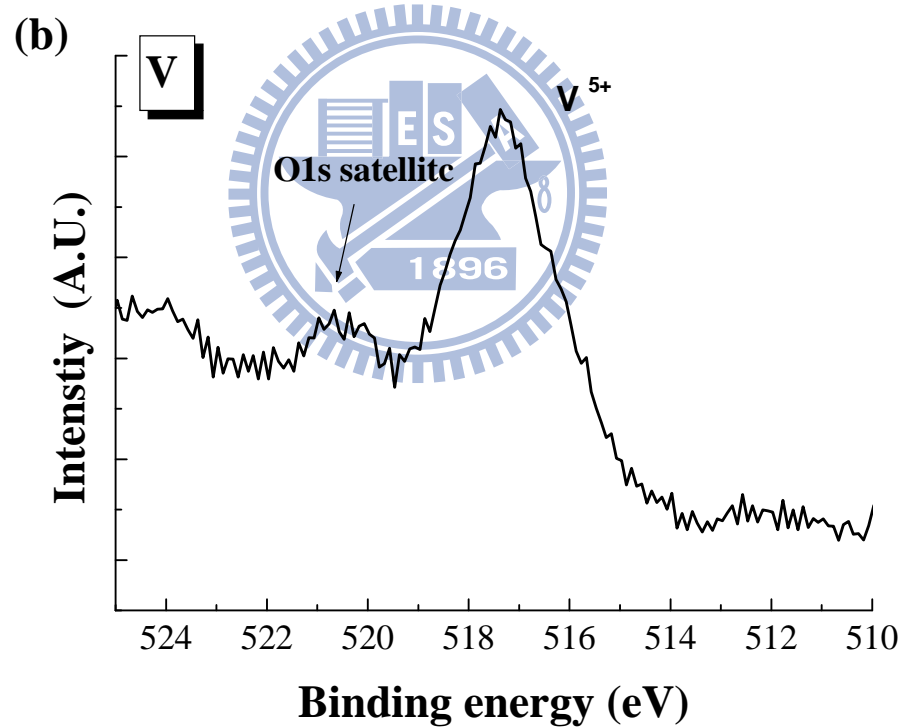
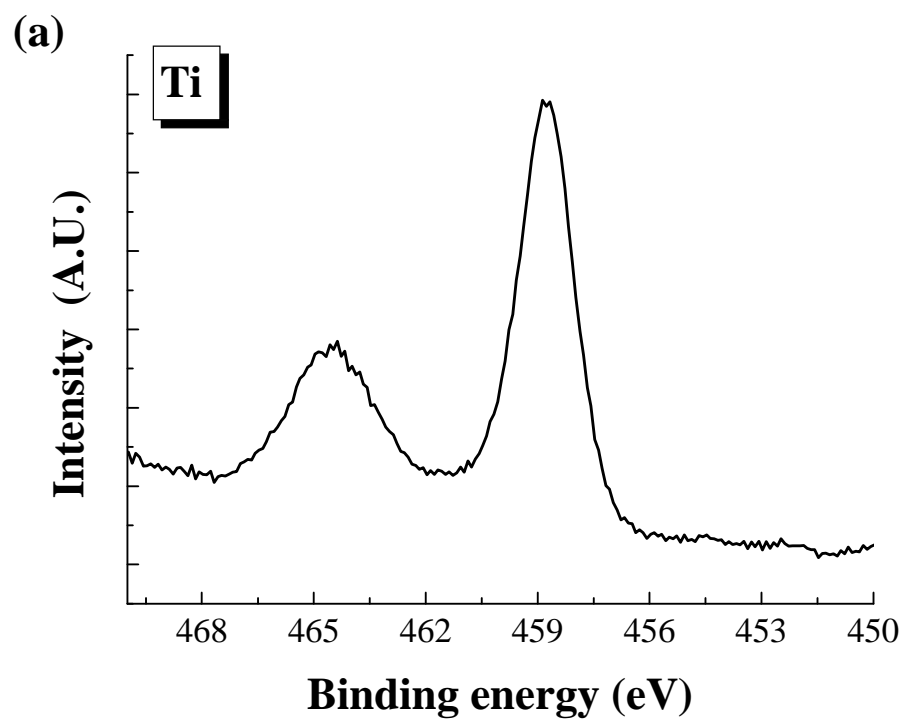
Appendix D-1 ESCA data for bulk and surface complex doping materials.

	V 2p <sub>3/2</sub> (eV)			Ti 2p <sub>3/2</sub> (eV)	Surface V/Ti (atomic ratio)			
	V <sup>III</sup>	V <sup>IV</sup>	V <sup>V</sup>		V <sup>III</sup> /Ti	V <sup>IV</sup> /Ti	V <sup>V</sup> /Ti	V/Ti
VT 2×10 <sup>-1</sup>	- <sup>a</sup>	-	517.4	458.8	-	-	0.61	0.61
(Sputter time : 60 seconds)	515.2	516.2	518	458.9	0.09	0.31	0.10	0.50
SVT 3×10 <sup>-1</sup>	-	-	517.3	458.7	-	--	0.33	0.33



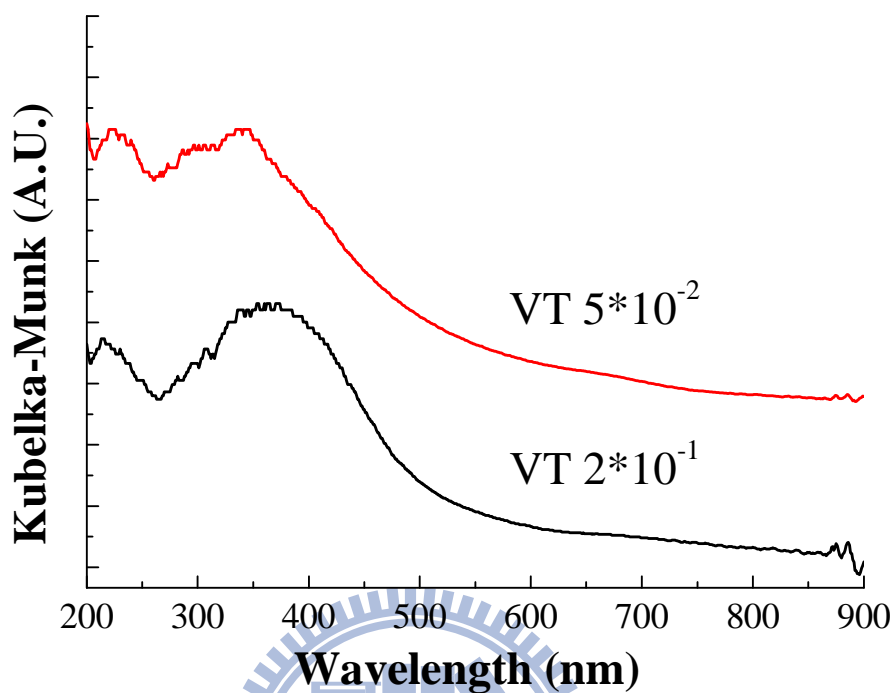


Appendix D-2 The XPS spectra of  $\text{VT}_2 \times 10^{-1}$  illustrated before and after Ar ion gun sputter. (A) The evolution Ti (2p) XPS spectra and (B) The evolution V (3d) XPS spectra.



Appendix D-3 The evolution Ti (2p) and V (3d) XPS spectra of SVT3 $\times 10^{-1}$ .

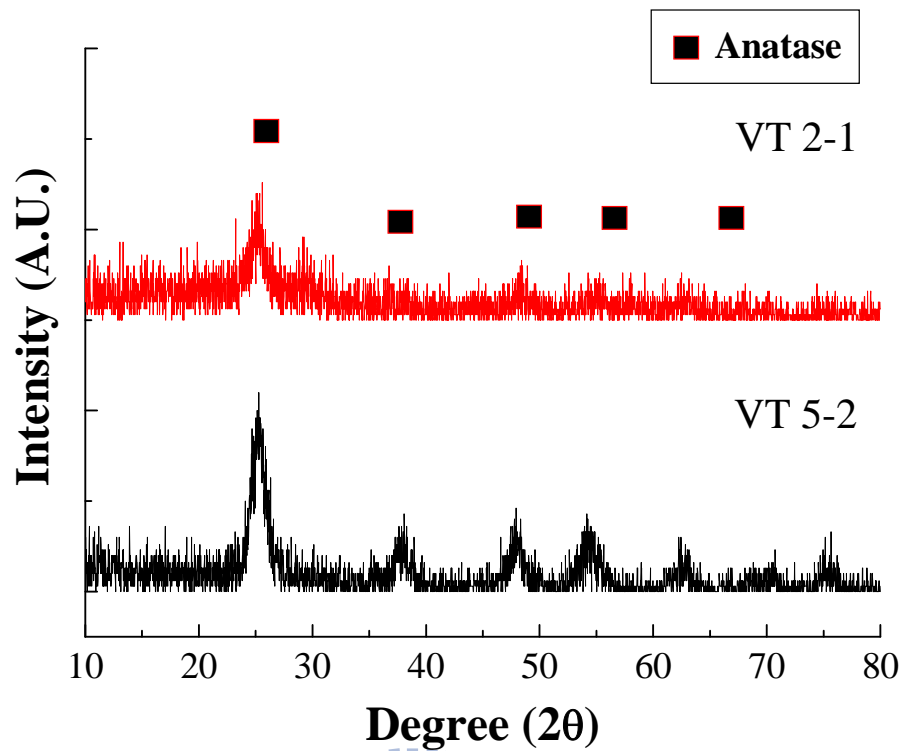
## Appendix E Bulk doped materials with high vanadium ions



Appendix E-1 The UV-Vis spectra of VT5×10<sup>-2</sup> and VT 2×10<sup>-1</sup>.

Appendix E-2 The UV-Vis data of VT5×10<sup>-2</sup> and VT 2×10<sup>-1</sup>.

Bulk doped materials	
Materials	Band gap (eV)
TiO <sub>2</sub>	3.1
VT 5×10 <sup>-2</sup>	2.4
VT 2×10 <sup>-1</sup>	2.4



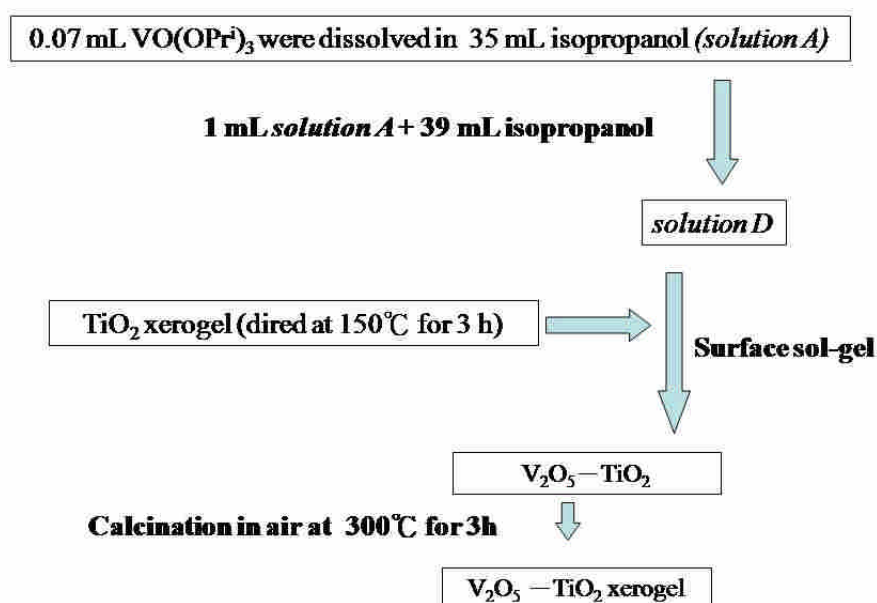
Appendix E-3 The XRD spectra of  $VT5 \times 10^{-2}$  and  $VT 2 \times 10^{-1}$ .

Appendix E-4 The XRD data of  $VT5 \times 10^{-2}$  and  $VT 2 \times 10^{-1}$ .

Bulk doping materials			
Materials	Crystal size (nm)	d-spacing (nm)	Weight ratio of Rutile (%)
TiO <sub>2</sub>	6.1 ± 0.6	350	31.1
VT 5 × 10 <sup>-2</sup>	5.5	352	—
VT 2 × 10 <sup>-1</sup>	5.2	353	—

## Appendix F Vanadium-doped on the surface of TiO<sub>2</sub>

Vanadium-doped materials are prepared by surface sol-gel process, as shown in Appendix F-1. The different from surface doped materials is lack of TTIP in *solution D*. To add 1.0 g TiO<sub>2</sub> which is calcinated at 150 °C for 3h into sample tube and then inject 25 mL mixture precursor solution into tube. After 10 min immersion, the production was separated from solution by gravity. The solid was dried at 100 °C and then calcined at 300 °C for 3 h. The xerogel obtained was named SVTP.



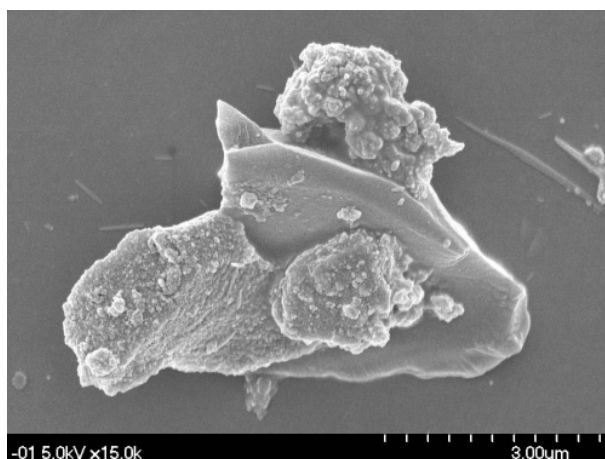
Appendix F-1 The synthetic process of surface doping materials.

Appendix F-2 The bulk V-to-Ti atomic ratios of surface doped TiO<sub>2</sub> with pure vanadium.

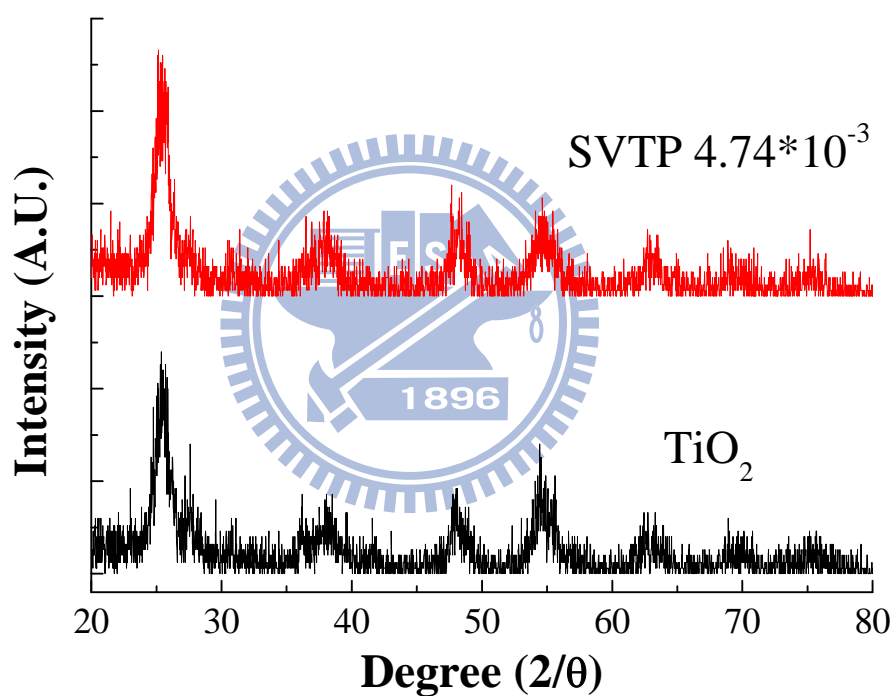
Materials	Bulk V/Ti ratios <sup>a</sup>	Sample name
SVTP	$4.74 \times 10^{-3}$	SVTP $4.74 \times 10^{-3}$

<sup>a</sup> determined by ICP-MS





Appendix F-3 SEM image of surface doped materials (pure).



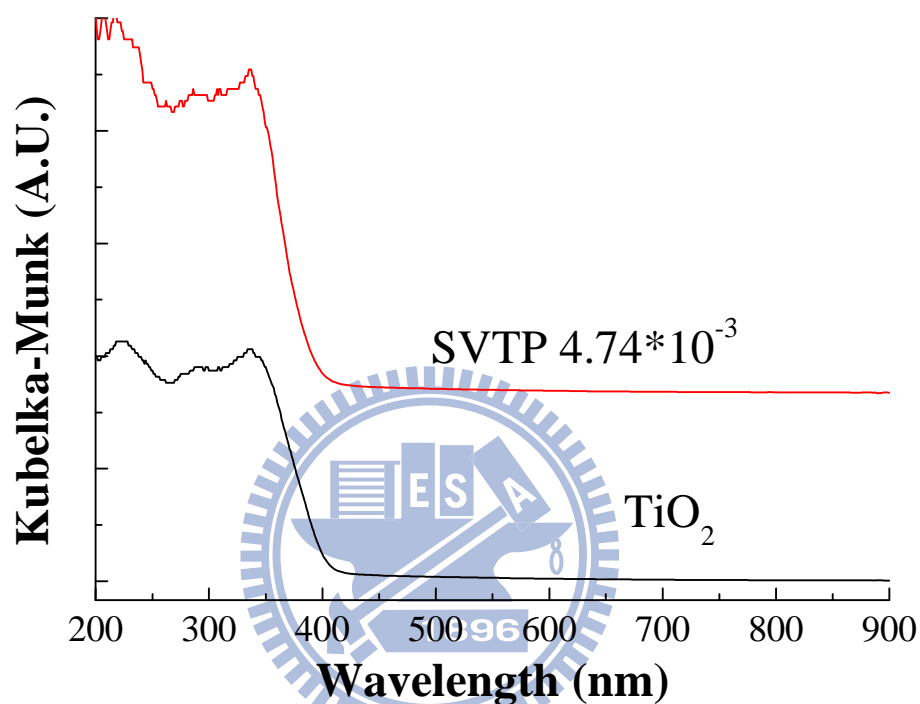
Appendix F-4 The XRD spectra of  $\text{TiO}_2$  and  $\text{SVTP } 4.74 \times 10^{-3}$ .

Appendix F-5 The XRD data of  $\text{SVTP } 4.74 \times 10^{-3}$  and  $\text{TiO}_2$ .

Surface doping materials (Pure)			
Materials	Crystal size (nm)	d-spacing (pm)	Weight ratio of Rutile (%)
$\text{TiO}_2$	$8.3 \pm 0.1$	$350 \pm 2$	28.7
SVTP $4.74 \times 10^{-3}$	9.5	350	-

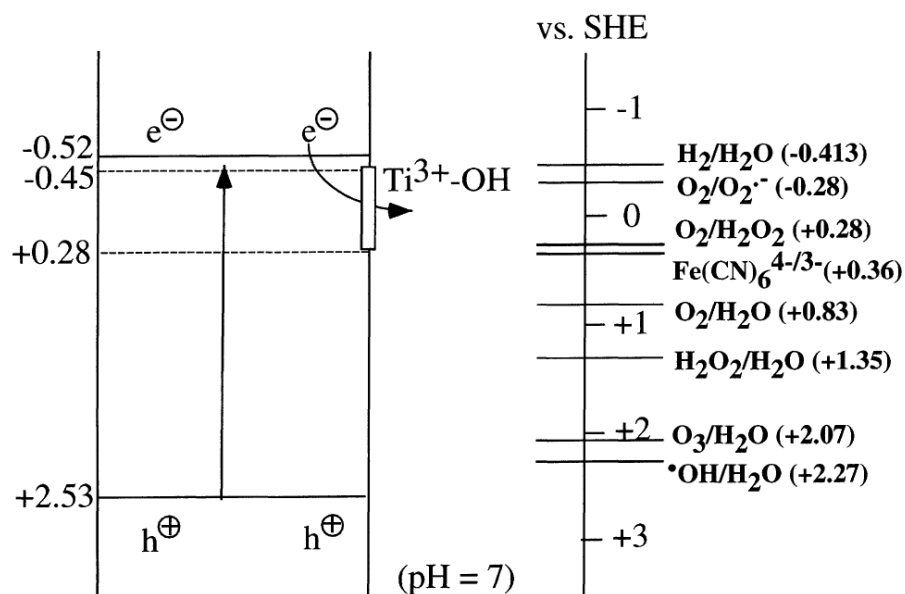
Appendix F-6 The specific surface area of all of surface doping material with pure vanadium ions.

Surface doping materials		
Sample	TiO <sub>2</sub>	SVTP 4.74×10 <sup>-3</sup>
S <sub>BET</sub> (m <sup>2</sup> /g)	99 ± 2	103

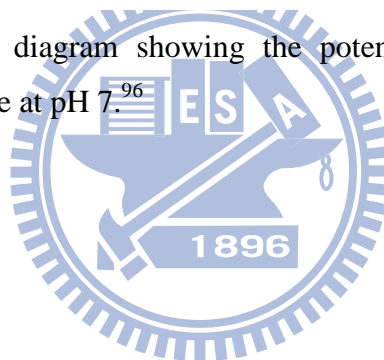


Appendix F-7 The UV-DRS spectra of TiO<sub>2</sub> and SVTP 4.74×10<sup>-3</sup>.

## Appendix G Redox potential



Appendix G-1 Schematic diagram showing the potentials for various redox processes occurring on the  $\text{TiO}_2$  surface at pH 7.<sup>96</sup>



## Appendix H Langmuir-Hinshelwood kinetics

Langmuir-Hinshelwood (LH) kinetics which is the most commonly used kinetic expression to explain the kinetics of the heterogeneous catalytic processes. The Langmuir-Hinshelwood equation is given by:

$$r = -\frac{dC}{dt} = \frac{k_r KC}{1 + KC} \quad (\text{H-1})$$

where  $r$  respects the rate of reaction that changes with time,  $C$  is concentration at any time  $t$  during degradation,  $K$  respects equilibrium constant for adsorption of the substrate onto catalyst, and  $k_r$  respects limiting rate of reaction at maximum coverage under the given experimental condition.

The constants  $k_r$ , and  $K$  can be calculated from the corresponding integrated expression. This equation can be integrated between the limits:  $C=C_0$  at  $t=0$  and  $C=C$  at  $t=t$ . The integrated expression is given by :

$$\ln\left(\frac{C}{C_0}\right) + K(C_0 - C) = k_r Kt \quad (\text{H-2})$$

Most of researchers approximated equation H-1 to first order kinetics for the condition  $C < 1$  mM, as  $KC$  is much less than unity.<sup>97, 98</sup> If the term  $KC \ll 1$  then equation H-1 is reduce to :

$$r = k_r KC \quad (\text{H-3})$$

In the case of equation H-3, the constants  $k_r$ , and  $K$  can be calculated from the corresponding integrated expression. This equation can be integrated between the limits:  $C=C_0$  at  $t=0$  and  $C=C$  at  $t=t$ . The integrated expression is given by :

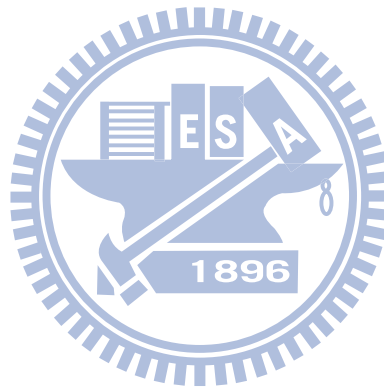
$$-\ln\left(\frac{C}{C_0}\right) = k_1 t \quad (\text{H-4})$$

where  $k_I = k_r K$ , which respects first order rate constants.

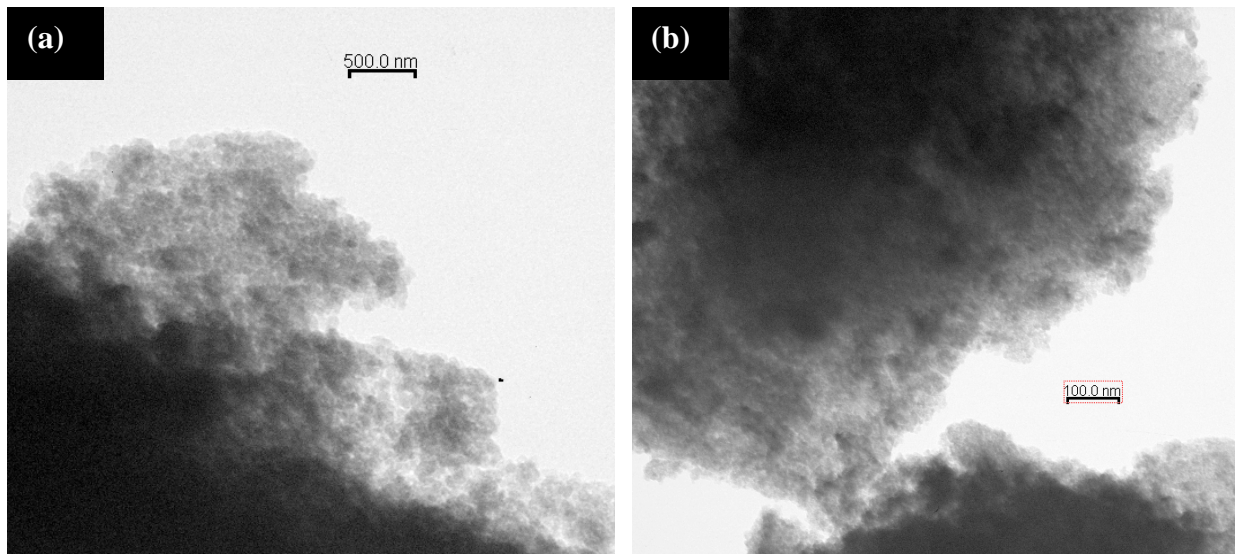
In addition, for  $C > 5$  mM, the LH kinetics reduced to zero order when  $KC \gg 1$ , in which case the reaction rate will be maximal. Thus the Langmuir-type kinetic rate expression reduces to a zero-order rate expression and the overall rate would not depend on external mass transfer, i.e., be kinetically limited. The concentration versus time will follow a linear relationship. Then the zero-order rate expression should be expressed as:<sup>97,98</sup>

$$r = -\frac{dC}{dt} = k_0 \quad (\text{H-5})$$

where  $k_0$  respects zero-order rate constant.



## Appendix I TEM of surface doped materials



Appendix I-1 The TEM images of SVT  $1.10 \times 10^{-2}$ . (a) 12000x (b) 60000x.

